Dissipative and $\mathcal{PT}$-Symmetry Breaking Phase Transitions in Open Spin Systems

PhD Thesis

Simon Kothe

Open Quantum Systems Group
Department of Physics
University of Strathclyde, Glasgow

July 16, 2024

This thesis is the result of the author's original research. It has been composed by the author and has not been previously submitted for examination which has led to the award of a degree.

Abstract

This thesis is concerned both with investigating the effects an environment has on quantum systems as well as with methods for the study of open quantum systems. In experiments and applications it is impossible to separate a quantum system from its environment. This often causes decoherence and loss of information, however, environments can also be used to drive systems into novel states which cannot otherwise be realized in Hamiltonian systems.

In the first part of the thesis the effects of environments are studied by constructing a model which possess both an equilibrium-connected phase transition as well as a $\mathcal{PT}$-symmetry breaking phase transition. The latter depends on the fine balance of gain and loss, and can thus only exists in the context of open quantum systems. Equilibrium-connected phase transitions are ones which recover the equilibrium transition of a model in the limit of vanishing dissipation. We consider a $\mathcal{PT}$-symmetric *Lipkin-Msekov-Glick* (LMG) dimer. Each part of the model is individually well understood and we can gain insight by understanding how they are affected by each other. The presence of the environment causes corrections to the critical threshold of the second-order phase transition of the LMG model. We further find that presence of the second-order phase transition delays the $\mathcal{PT}$-phase transition as the system is first driven through various intermediate phases.

Quantum systems in general, and open quantum systems in particular suffer exponential scaling of the state space in system size. This makes approximative methods a necessity for the study of strongly-correlated systems. In the second part of the thesis we propose a novel *Neural Quantum State* (NQS) ansatz for the steady state density matrix. NQS are ansatz functions for variational Monte Carlo whose structure

is informed by the architecture of neural networks. A simple NQS is the *Restricted Boltzmann Machine* (RBM). NQS and in particular RBMs have been shown to possess a volume-law entanglement capacity which significantly expands the range of states NQS can represent over comparable ansatze such as tensor networks. This makes them prime candidates for the representation of highly-correlated states of spatially extended systems. The proposed ansatz uses the Choi-Isomorphism to represent a local density matrix as a state vector. This allows a simple extension of the basic RBM architecture to represent the state without requiring a complex purification. The ansatz is compared to other approach on two different dissipative transverse field Ising models. We find that the proposed ansatz can more efficiently represent strongly correlated states than competing approaches.

Publications

Liouville-space neural network representation of density matrices

Phys. Rev. A 109, 062215 (2024)

Neural network quantum states such as ansatz wave functions have shown a great deal of promise for finding the ground state of spin models. Recently, work has focused on extending this idea to mixed states for simulating the dynamics of open systems. Most approaches so far have used a purification ansatz where a copy of the system Hilbert space is added, which when traced out gives the correct density matrix. Here we instead present an extension of the restricted Boltzmann machine which directly represents the density matrix in Liouville space. This allows the compact representation of states which appear in mean-field theory. We benchmark our approach on two different versions of the dissipative transverse-field Ising model, which show our ansatz is able to compete with other state-of-the-art approaches.

Contents

List of Figures

List of Acronyms

CNN	Convolutional Neural Networks
DMRG	Density Matrix Renormalization Group
ED	Exact Diagonalization
EP	Exceptional Point
HP	Holstein-Primakoff
LDM	Liouville Density Machine
LMG	Lipkin-Keshkov-Glick Model
MCMC	Markov Chain Monte Carlo
MF	Mean Field
MPS	Matrix Product States
MPO	Matrix Product Operator
NDM	Neural Density Machines
NESS	Non-Equilibrium Steady State
NHH	Non-Hermitian Hamiltonian
NQS	Neural Quantum State
OQS	Open Quantum Systems
PEPS	Projected Entangled Pair State
POVM	Positive Operator Valued Measure
QT	Quantum Trajectories

RBM	Restricted Boltzmann Machines
RNN	Recurrent Neural Networks
SR	Stochastic Reconfiguration
SGD	Stochastic Gradient Descent
SVD	Singular Value Decomposition
TEBD	Time-Evolving Block Decimation
TFI	Transverse-Field Ising model
TN	Tensor Networks
VMC	Variational Monte Carlo

Preface/Acknowledgements

I acknowledge the help of my wife who provided much support throughout its duration.

I further acknowledge the help of my friends, in particular John, Jannis, Freddy, Malte and Dominic who have provided excellent comments.

And last but not least my supervisor Peter, who gave me the opportunity to do a PhD in the first place and who provided invaluable support and guidance throughout the entire time.

Chapter 0. Preface/Acknowledgements

Chapter 1

Overview

For over a century quantum physics has been exceedingly important from the viewpoint of fundamental physics and very well supported in experiments.

Due to the recent advent of quantum computers and related technologies it has gained an increased importance in applied physics as well. An issue with both experiments and applications, however, is the presence of an environment which affects the system under consideration, i.e. all realistic quantum systems are open.

The effects an environment may have on systems have long been considered a bane rather than a wellspring of interesting physics, as they tend to destroy coherences. Furthermore, the state of an open quantum system is generally described by a density matrix, which scales even worse in system size than the pure states of equilibrium systems. Environments are however not just sources of noise and unwanted interference. They can drive the system into novel states which are inaccessible to the usual Hamiltonian physics [1,3,4]. These novel states and phenomena are what we will focus on in this thesis. In particular we will study how the environment affects the system. We will do so by studying the competition of $\mathcal{PT}$-symmetry breaking, a purely non-equilibrium effect with ones that have direct analogues in closed systems, a second-order phase transition. Furthermore, we will introduce a novel ansatz function for the efficient representation of a non-equilibrium steady state density matrix in the context of variational Monte Carlo [5].

1.1 Dissipative Phase Transitions

One of the most fascinating aspects of all branches of physics are phase transitions. They occur as the parameters of a system are varied and the relative strength of competing terms changes. Such transitions occur all around us, from boiling water in the kettle, over the snow in winter, to classic magnets which transition from a disordered to an ordered phase where all spins align. Such classical transitions generally occur as the temperature or density is varied. Classical phase transitions have been thoroughly discussed by Landau and Lifshitz who categorised based on whether they are discontinuous (first-order) or continuous (second-order) [6]. Continuous and discontinuous refer the behaviour of the order-parameter at the phase boundary. At a first-order phase transition the order parameter will change discontinuously, whereas at a higher-order phase transition the order parameter changes continuously.

In quantum physics something similar occurs at low temperatures where thermal fluctuations are small. Here it is no longer the competition between energy and entropy which drives the phase transition but the competition between non-commuting terms of the Hamiltonian. Such transitions have been extensively studied in the transverse field Ising model as well as the Quantum Rotor model [7]. Another important model is the LMG model. It is a non-linear collective spin model, which can be derived from a transverse field Ising model with all-to-all interactions. It possesses both a first- and a second-order phase transition [8, 9] depending on the relative sign of the terms.

Recently, dissipative phase transitions, i.e. phase transitions in open quantum systems, have garnered some attention. While in equilibrium systems the system states must necessarily be eigenstates of the Hamiltonian, in open quantum systems the bath can drive the system into exotic states which are unreachable in equilibrium systems. These transitions occur not just due to a competition between non-commuting terms of the Hamiltonian but also due to a competition between the Hamiltonian and the dissipation [3, 4, 10]. Often such transitions are closely related to zero temperature quantum phase transitions in the Hamiltonian. There are, however models where this is not the case.

1.2 $\mathcal{PT}$-Symmetry Breaking Phase Transitions

An altogether different type of transition is the $\mathcal{PT}$-symmetry breaking phase transition. Systems possessing a Parity-Time symmetry are symmetric under the combined exchange of a pair of degrees of freedom and the exchange of gain and loss. As this transition requires finely balanced gain and loss, this type of transition cannot exist in closed systems. Originally, $\mathcal{PT}$-symmetry breaking was thought of in terms of non-Hermitian Hamiltonian systems, where complex fields would take the role of coherent dissipation or driving [11]. For a while this was the exclusive domain of mathematical physicists, as implementing a non-Hermitian quantum system posed an experimental challenge. This was solved in 1998 by the authors of [12] who proposed a family of non-Hermitian Hamiltonians which could be realized in an experimental setting. Since then the research into $\mathcal{PT}$-symmetry breaking has produced some interesting experiments [13, 14] in the context of Hamiltonian systems.

More relevant to this thesis is the work of Huber et al. [1, 15], which extended the concepts of $\mathcal{PT}$-symmetry to microscopic Lindbladian systems, i.e. systems which experience incoherent jumps in addition to the coherent Hamiltonian dynamics. They identified a symmetry which the microscopic Lindblad master equation needed to possess a $\mathcal{PT}$-symmetry breaking phase transition. The system they consider consists of two collective spins of size S which interact with a collective spin-flip Hamiltonian. Each spin couples to the environment, however, one is driven, while the other is dissipative.

The $\mathcal{PT}$-symmetry breaking phase transition is driven by a competition between the coherent and incoherent parts of the master equation. In the limit of small but finite bath-coupling strength the drive and dissipation cancel precisely and the Hamiltonian perfectly mixes the system. In the limit of large dissipation, on the other hand, the system separates into to two parts, where one is dominated by gain and the other by loss.

In this thesis $\mathcal{PT}$-symmetry plays an important role in the model which we will investigate in Part I. As it is an effect exclusive to open systems it will help as a contrast

to the equilibrium-connected second-order phase transition of the LMG model.

1.3 Neural Quantum States

An issue that plagues numerical simulations of quantum systems is the "curse of dimensionality", i.e. the exponential scaling of the state space with system size. This severely limits the size of systems that can be exactly simulated with numerical methods. As phase transitions are only possible in the thermodynamic limit, this is a big problem.

To mitigate this problem physicists have come up with a wide variety of approximative methods. These can help us simulate and better understand many-body systems but are often limited by the entanglement of states. One that is of particular interest to this thesis is *Variational Monte Carlo* (VMC) [16]. As all other numerical methods, VMC uses, that most of the state space will never be seen by most relevant Hamiltonians. One can thus define an ansatz function whose parameters only grow polynomially in systems size and whose structure is hopefully as close as possible to that of the true state.

Similar to the wavefunction, the ansatz defines a probability distribution over the basis states, which can be sampled using Monte Carlo methods. With these one can then estimate the gradient of the energy with respect to the parameters and systematically approach the ground- or steady-state.

A class of ansatz functions which as been proven to be very capable of representing strongly-correlated states was recently proposed by Carleo and Troyer [17]. The parameter structure of these ansatze is informed by neural networks and hence called *Neural Quantum States* (NQS). They make use of neural networks' uncanny ability to efficiently represent extremely complex data. In physicists' terms, Neural Quantum States have a volume-law entanglement capacity [18].

In this thesis we propose a Neural Quantum State for the density matrix. It works by applying the Choi-Isomorphism in a similar vein to Zwolak et al. [19] to transform the density matrix into a density vector. By extending the the original ansatz of [17] to a third order polynomial in a similar manner to [20] we are able to discriminate four

local states. This allows us to efficiently find the steady state of open quantum models consisting of spins on a lattice. The ansatz forgoes the need for a global purification via auxiliary degrees of freedom as done in [21] and retains the simplicity and expressibility of the original NQS ansatz.

1.4 This Thesis

In this thesis we will examine a variety of models. In the first part we focus on the dissipative LMG-dimer model with an additional $\mathcal{PT}$-symmetry. As we will show, the LMG model can be derived from a transverse field Ising model with all-to-all interaction. In the second part we will describe how to use NQS for the study of open quantum systems with a particular emphasis on the transverse field Ising model with different kinds of dissipations.

This thesis is structured as follows. In Part I we propose and investigate a $\mathcal{PT}$-symmetric LMG dimer model, which in this form has not been investigated before. This model possess both an equilibrium connected second-order phase transition as well as a $\mathcal{PT}$-symmetry breaking phase transition. This will help us understand how each transition is influenced by the presence of the other. In Ch. 2 we introduce and discuss open quantum systems. We introduce the Lindblad master equation and discuss the necessary approximations to derive it. We further discuss the ideas of $\mathcal{PT}$-symmetry in both Hamiltonian and Lindbladian contexts. Finally, the LMG model and its phase transitions are discussed. In Ch. 3 we discuss the methods we will use to investigate the LMG dimer. Chief among them are mean-field and Holstein-Primakoff approximations. We discuss linear stability analysis and how it can be used to get a first idea of the phase diagram. We also give a brief introduction to Quantum Trajectories, which are used to achieve results for large but finite spin sizes. Ch. 4 finally concludes this part with a discussion of our results. We begin with a brief introduction to the behaviour of the individual models. We then discuss the *linear stability phase diagram* as well as what we assume to be the full phase diagram. We find that the environment causes second-order corrections to the phase boundaries. Furthermore, the presence of the second-order phase transitions causes the system to undergo a various other phase

transitions before it is driven over the $\mathcal{PT}$-symmetry breaking phase transition. Finally, we end the chapter with a comparison of mean-field with spin-Wigner functions.

Part II is concerned with the development of a novel ansatz for non-equilibrium steady state density matrices. Ch. 5 gives an overview over various methods for the numerical simulation of quantum systems, with a focus on Tensor Networks and VMC. In Ch. 6 we introduce and discuss the novel ansatz in more detail. We begin with a review of *Restricted Boltzmann Machines*, the original neural quantum states. We discuss how one can find the groundstate using stochastic gradient descent. We then introduce our architecture and discuss our motivation as well as how we can use it to find the steady-state. We end with a brief introduction to the *Markov Chain Monte Carlo* algorithm. Finally, in Ch. 7 we benchmark our ansatz. Our ansatz is compared with matrix product states as well as neural density machines. We use two different versions of the dissipative transverse field Ising model as test beds for our comparisons. We end the chapter with a discussion of our results and possible avenues of future developments.

Part I

$\mathcal{PT}$-symmetric LMG Dimer

Chapter 2

Introduction

Since the inception of quantum mechanics in the 1920s there has been a strong focus in research on equilibrium systems. These are systems which are closed to the outside in that no energy, no coherence and no information is ever lost over time. They are described by a Hermitian operator with real eigenvalues.

An issue with this approach is that realistic quantum systems are never closed and always interact with a larger environment, see Fig. 2.1 for a sketch. As we will discuss in more detail later in this chapter, this changes the physics of the system significantly. One of the most important changes is the existence of a steady state in *Open Quantum Systems* (OQS) which is reached as the endpoint of time evolution. In a similar fashion to ground states, the properties of these steady states can change dramatically as system parameters are varied and the system undergoes a "dissipative phase transition".

As we have mentioned in the introduction to this thesis, we are interested in gaining a deeper understanding of the effects a bath has on the states of the system. The angle of investigation we choose to pursue in our work is to contrast purely non-equilibrium effects with equilibrium-connected effects, i.e. effects which remain if the system-bath coupling is switched off. The systems we choose, i.e. the LMG model [22] as well the $\mathcal{PT}$-model [1] are individually well established and understood. This allows us to compare our results with well established ones.

In this chapter we lay the groundwork for our investigation. We discuss the type of OQS we are interested in, i.e. those with a Markovian bath. We further give a

brief overview of purely non-equilibrium phenomena. This is followed by a qualitative introduction to dissipative phase transitions and collective spin models, namely the Dicke model and the LMG model. Ch. 3 then builds upon this by discussing the numerical and analytical methods we use in more detail. Finally, Ch. 4 of this part then discusses the results of our investigation.

2.1 Open Quantum Systems

The dynamics of an OQS cannot be described exactly. The bath alone is usually assumed to be infinitely large. And to suppress finite size effects in the system itself for any amount of time, we need very large systems as well. This makes it immediately clear, that if we want to have any chance of efficiently describing the dynamics of the OQS by itself, we need to at least trace out the bath degrees of freedom from the equation. The starting point of the derivation of such an equation is the von Neumann equation for the Hamiltonian $\mathcal{H}$ and density matrix ρ of the "universe":

$$\frac{d}{dt}\rho = -i[\mathcal{H}, \rho]; \tag{2.1}$$

where the total Hamiltonian is given by a sum of the system Hamiltonian $\mathcal{H}_\mathrm{S}$, the bath Hamiltonian $\mathcal{H}_\mathrm{B}$ and the interaction Hamiltonian $\mathcal{H}_\mathrm{I}$:

$$\mathcal{H} = \mathcal{H}_\mathrm{S} + \mathcal{H}_\mathrm{B} + \mathcal{H}_\mathrm{I}. \tag{2.2}$$

A consequence of tracing out the bath from the equation is that the state of the open system will generally be a mixed state and described by a density matrix. Density matrices describe both classical uncertainties, such as a probability distribution over an ensemble of states, as well as quantum properties, such as entanglement. The matrices fulfil three properties: Hermiticity (they are observable), unit trace, and positivity (they define a probability distribution). A general density matrix ρ is defined as a

weighted sum over all possible basis states, such that the weights sum to 1

$$\rho = \sum_i p_i \left|\phi_i\right\rangle \left\langle\phi_i\right|, \tag{2.3}$$

where p_i are the classical probabilities of each basis state and $\{\phi_i\}$ are the basis states which diagonalize the density matrix. Density matrices allow one to distinguish mixed states and pure states. Pure states can be described by a state vector and are the usual eigenstates of Hamiltonian systems. They are pure in the sense that there is no classical probability distribution over a larger set of states and all uncertainty is purely quantum. Mixed states are a mixture of several pure states as in Eq. 2.3. Pure states have the additional property of being idempotent, i.e. $\rho^2 = \rho$, which has the consequence of $\mathrm{Tr}[\rho^2] = 1$. Mixed states on the other hand necessarily have $\mathrm{Tr}[\rho^2] < 1$.

The quantity $\mathrm{Tr}[\rho^2]$ gives us a measure of how close a state is to being a pure state and is therefore referred to as *purity*. Now we are equipped to understand why the state of an open quantum system is necessarily mixed and must be described by a density matrix. Generally, the total state of the system and the bath combined will be entangled and pure. A simple example of such a state is the Bell-state, where we assume one spin to be the system and the other the bath:

$$\left|\Psi\right\rangle = \frac{1}{\sqrt{2}} \left|0,1\right\rangle + \left|1,0\right\rangle. \tag{2.4}$$

Its density matrix is then given by

$$\rho = \frac{1}{2} \left(\left|0,1\right\rangle + \left|1,0\right\rangle\right) \left(\left\langle 0,1\right| + \left\langle 1,0\right|\right) \tag{2.5}$$

$$= \frac{1}{2} \left(\left|0,1\right\rangle \left\langle 0,1\right| + \left|1,0\right\rangle \left\langle 0,1\right| + \left|0,1\right\rangle \left\langle 1,0\right| + \left|1,0\right\rangle \left\langle 1,0\right|\right). \tag{2.6}$$

Since we only have one pure state which contributes to the density matrix, the purity is 1. We can now trace out one of the subsystems and investigate if the state we are

left with is pure or mixed:

$$\rho_A = \mathrm{Tr}_B[\rho] = \frac{1}{2}\mathrm{Tr}_B\left[|\Psi\rangle\langle\Psi|\right] \tag{2.7}$$

$$= \frac{1}{2}\mathrm{Tr}_B\left[(|0,1\rangle + |1,0\rangle)(\langle 0,1| + \langle 1,0|)\right] \tag{2.8}$$

$$= \frac{1}{2}\left(|0\rangle\langle 0| + |1\rangle\langle 1|\right). \tag{2.9}$$

This yields for the purity P of the reduced state of subsystem A:

$$\rho_A^2 = \frac{1}{4}\left(|0\rangle\langle 0| + |1\rangle\langle 1|\right) \tag{2.10}$$

$$P = Tr\left[\rho_A^2\right] = \frac{1}{2} < 1. \tag{2.11}$$

While this is an extremely simplified example compared to an infinite bath coupled to a large and complex system, the idea nonetheless holds generally. Any state of entangled subsystems will lead to a mixed state under a partial trace and one requires a density matrix to describe the state of the remaining subsystem.

The equations which govern the dynamics of these density matrices are called *Master Equations*. Master equations are a concept from the mathematical field of stochastic mathematics and describe how probability distributions evolve over time, see Ch. 1 of Ref. [23]. They introduce various approximations that can be utilized to derive different master equations, as well as details when each of them fails. Another excellent but more succinct introduction to the field is found in Ref. [24]. The most general master equation which is fully trace preserving and completely positive is the Lindblad master equation

$$\frac{d}{dt}\rho = \mathcal{L}\rho_s = -i[\mathcal{H}, \rho_s] + \sum_k \gamma_k \left(A_k \rho_s A_k^\dagger - \frac{1}{2}\{A_k^\dagger A_k, \rho_s\}\right), \tag{2.12}$$

where $\mathcal{L}$ is the "Liouvillian" super-operator, that governs the dynamics of the density matrix ρ. Here, $\mathcal{H}$ and ρ_s are the Hamiltonian and the partial density matrix of the system. A_k are the jump operators, which govern the influence of the bath on the system and γ_k is the strength of this coupling. The sum runs over the different dissipation channels k. This equation is guaranteed to possess a so-called steady state,

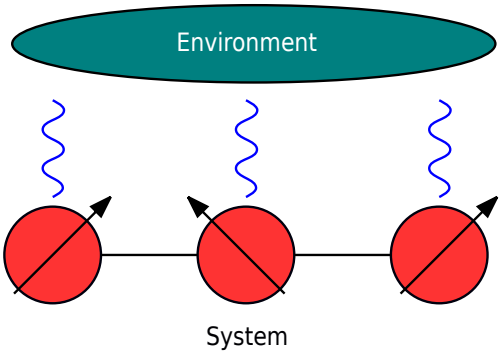

Figure 2.1: This is a simple schematic of an open quantum system. The system here consists of three spins (red) each experiencing some interactions (blue) with a large environment (turquoise). To be able to describe the dynamics of the system, one has to trace out the the environmental degrees of freedom. This leads to a mixed state whose dynamics are described by a master equation.

i.e. a state such that in the long time limit the state satisfies

$$\lim_{t\to\infty} \mathcal{L}\rho(t) = 0. \tag{2.13}$$

While there are other master equations, such as the Redfield equation, we will not be concerned with systems that cannot be described by a Lindblad master equation in this thesis.

The equation can be derived by tracing out the bath degrees of freedoms from the state and the governing equation of motion. This is generally not a trivial task, and requires one to make a number of approximations. Consequently the Lindblad master equation describes the dynamics of quantum systems which are *weakly coupled* to a *memoryless environment* as well as subject to a *rotating wave approximation*. These three approximations are based on the observation that one can, in a wide array of problems, separate three time or frequency scales: The frequency scale of the system given by the typical energy eigenvalues of the Hamiltonian ω_s, the frequency scale of the bath-system interactions given by the dissipation strength γ, and the inverse time scale at which correlations inside the bath decay ω_b. These approximations are generally well satisfied in cavity quantum electrodynamic systems with pumped and leaky cavities.

The first approximation is also called the *Born approximation*, see e.g. Refs. [23,25].

It essentially means that relevant frequencies of the bath and the system are much faster than that of their coupling, i.e. on the typical time scale on which bath and system interact with each other, both have evolved appreciably by themselves $\gamma \ll \omega_s, \omega_b$. The second approximation is known as the Markov approximation. It means that any correlations inside the bath induced by system-bath interaction decay much faster than the characteristic time of the system-bath interaction, $\tau_b \ll 1/\gamma$. Essentially, each time the system and bath interact, any knowledge of previous interactions has long been lost. This means in particular, that the system cannot couple to a previous system state via feedback from the bath. Such memory effects play an important role in the very active field of non-Markovian open quantum systems [26]. The final approximation is the rotating wave approximation. It is particularly well known in quantum optics [27]. In essence it states that once we transform the problem into the interaction picture, some terms will be constant in time while others will rotate with a large frequency over the relaxation time and average to zero.

Now that we have a basic idea of how the dynamics of an OQS are described, we will discuss a few phenomena exclusive to them. We will begin with a brief introduction of dissipative systems described by non-Hermitian Hamiltonians and then move on to fully open quantum systems described by a Lindblad master equation.

2.2 Non-Equilibrium Phenomena

For some time the effects of environments have been regarded as a nuisance. As an example, see the lengths gone to, to shield quantum computers from outside noise. And not without reason, as environments introduce noise, destroy coherences and leak information and energy irretrievably into the environment. On top of these physical consequences, environments make the problem much harder computationally and analytically. However, for all the problems they may cause, environments introduce a score of phenomena that do not exist in closed systems. Where in equilibrium systems states are limited to those that can be written as $e^{-\beta\mathcal{H}}$, drive and dissipation allow us to reach states outside of this class, see lasers for example. Here we will introduce a handful of these phenomena, chief among them $\mathcal{PT}$-symmetry breaking, exceptional

points as well as quantum contact processes.

One important example of exclusively non-equilibrium physics is Parity-Time symmetry and its breaking, which will be a major part of our discussions in later chapters. For a while, $\mathcal{PT}$-symmetry was the exclusive domain of mathematicians as there was no idea how to implement such systems in an experimental setting [11,28]. In 1998, the authors of Ref. [12] described a large family of non-hermitian Hamiltonians that possess a real spectrum due to their $\mathcal{PT}$-symmetry. Non-hermitian Hamiltonians include gain and loss terms, which generally leads to a complex spectrum. The consequence is that the trace of the density matrix is no longer conserved. Such systems represent the no-jump evolution of master equations. In the case of finely balanced gain and loss, as well as weak dissipation strength, the non-hermitian Hamiltonian retains a real spectrum [11,12]. In the beginning, $\mathcal{PT}$-symmetry was thought of purely in semi-classical terms and described by non-hermitian Hamiltonians (NHH). An example of a $\mathcal{PT}$-symmetric NHH can be found in [11]

$$\mathcal{H}_{\mathrm{NH}} = \omega\mathbb{1} + \kappa\sigma^x - i\gamma\sigma^z, \tag{2.14}$$

where σ^z and σ^x are Pauli-matrices. This Hamiltonian describes a 2-level system with an energy scale ω, balanced gain and loss γ, and a level-coupling κ. This Hamiltonian can be readily diagonalized, which leads to the eigenvalues

$$\omega_\pm = \omega \pm \sqrt{\kappa^2 - \gamma^2}, \tag{2.15}$$

and eigenvectors

$$v_\pm^T = \left(-\frac{i\gamma \pm \sqrt{\kappa^2 - \gamma^2}}{\kappa}, 1 \right) \tag{2.16}$$

For $\kappa > \gamma$ these eigenvalues are clearly real and the eigenvectors are distinct. At $\kappa = \gamma$, however, we can see that not only $\omega_+ = \omega_-$, but more importantly also

$$v_+^T = \left(-\frac{i\gamma}{\kappa}, 1 \right) = v_-^T. \tag{2.17}$$

At this *exceptional point* (EP) a number of eigenvectors coalesce, which renders the

Hamiltonian non-diagonalizable. The number of coalescing eigenvectors determines the order of an EP, e.g. at a second-order EP one sees two eigenvectors become equal. This is a hallmark feature of $\mathcal{PT}$-symmetry breaking. For $\kappa < \gamma$ the eigenvalues develop an imaginary part, while for both states the real part is equal. A consequence is that, while the groundstate before the exceptional point is unique, it will be degenerate at the EP and beyond.

In the few decades since, the theoretical and experimental research into the effects of $\mathcal{PT}$-symmetry has drastically picked up pace and resulted in many effects in optics such as unidirectional light propagation [13,29] as well as in mechanics [14], acoustics [30,31], electronics [32,33] and, most relevant to this thesis, spin systems [34–38]. The authors of Ref. [34] proposed a way of transforming a non-hermitian Hamiltonian into a hermitian Hamiltonian, which allowed them to implement and investigate $\mathcal{PT}$-symmetric Hamiltonian in an experimental setup using a Nitrogen-Vacancy center in diamond. In Ref. [38] the authors investigated a $\mathcal{PT}$-symmetric Ising chain and found a rich phase diagram containing second- and 3^{rd}-order exceptional points.

Up until recently, research into exceptional points has been restricted to the semi-classical case, in the sense that quantum noise and quantum jumps due to the environment have been neglected. The authors of [39] have developed a framework to incorporate quantum jumps by using the Lindblad master equation as their starting point. This leads to what they call *Lindblad Exceptional Points* (LEPs), as opposed to *Hamiltonian Exceptional Points* (HEPs). They could show that the presence of LEPs can have a significant effect on the dynamical behaviour of the Lindblad master equation. Where the dynamics at non-exceptional points is generally given by a sum of exponential decays of the non-steady state eigenmatrices of the Liouvillian of Eq. 2.12, this exponential decay is multiplied by a polynomial [39]. In particular in [39–41] the authors suggest that such modified dynamics could point towards the presence of a second-order dissipative phase transition. In [28] the authors investigate the effect of LEPs in the context of the Scully-Lamb laser theory. More recently, Pocklington et al. used $\mathcal{PT}$-symmetry to stabilize finite-density phases in photonic and bosonic models, proposing a $\mathcal{PT}$-laser, see Ref. [42].

For all the work that has been done in Hamiltonian systems, a formal and robust definition of $\mathcal{PT}$-symmetry in dissipative systems has been the topic of some discussion. The main contributions were made by Prosen et al. in [43, 44] as well as more recently by Huber et al. in [1, 15]. The latter studies focused on a driven-dissipative spin-flip model which we will collective refer to as the $\mathcal{PT}$-model:

$$\mathcal{L}[\rho] = -i\left[\mathcal{H}_{\mathrm{PT}}, \rho\right] + \frac{\gamma}{S}\left(\mathcal{D}[S_a^-] + \mathcal{D}[S_b^+][\rho]\right) \tag{2.18}$$

$$\mathcal{H}_{\mathrm{PT}} = \frac{\lambda}{2S}\left(S_a^+ S_b^- + S_b^- S_a^+\right) \tag{2.19}$$

$$\mathcal{D}[S_a^-][\rho] = S_a^- \rho S_a^+ - \frac{1}{2}\{S_a^+ S_a^-, \rho\} \tag{2.20}$$

$$\mathcal{D}[S_b^+][\rho] = S_b^+ \rho S_b^- - \frac{1}{2}\{S_b^- S_b^+, \rho\}. \tag{2.21}$$

In recent works evidence was presented in support of the definition by Huber in the form of similarities of the dynamical behaviour of dissipative systems to those of Hamiltonian systems [2,45]. In Ref. [2] the authors show in particular that at the point of the PT phase transition as introduced in [1, 15], the eigenvalue structure of the Liouvillian changes. More specifically, they show that in the thermodynamic limit, before the transition some eigenvalues are purely imaginary, while after the transition, the eigenvalues are purely real, i.e. the dynamical behaviour changes from oscillatory to purely damped. This is in accordance with $\mathcal{PT}$-symmetry breaking found in NHH systems.

The appearance of purely imaginary eigenvalues in the thermodynamic limit of the $\mathcal{PT}$-symmetric phase has the consequence that the long-time limit and the thermodynamic limit do not commute [45]. More specifically, if the thermodynamic limit is taken before the long-time limit, the system will have oscillatory dynamics. If the limits are taken in different order, however, the system will be damped into some stationary steady state before the thermodynamic limit. In their paper from 2023 as well as its supplemental material Nakanishi et al. also show that the system investigated in [15] in the thermodynamic limit of the $\mathcal{PT}$-symmetric phase constitutes a Boundary Time Crystal [45, 46].

Another class of processes which cannot exist in closed systems are quantum contact processes with absorbing states [47]. Classically, contact processes can be used to

model for example the spread of disease. In the quantum case, neighbouring sites are flipped coherently depending on the local spin-state ("infection"), while a Lindbladian dissipation is used to incoherently flip spins ("healing"). Classically, these systems possess an active state ("endemic") as well as a dark state ("fully healed") with a phase transition of the direct percolation universality class. In the quantum case, evidence has been put forward that the phase transition does not belong to the directed percolation class Refs. [48, 49].

This is just a small and thoroughly incomplete list of phenomena which are exclusive to dissipative and open quantum systems. It should, however limited, still give a good idea of the general nature of things to expect in open quantum systems. In particular $\mathcal{PT}$-symmetry and its breaking will play an important role in later chapters of the thesis. For all its unique features and phenomena, OQS share many properties with equilibrium quantum systems and even classical, thermal systems. One such feature are *Phase Transitions*.

2.3 Dissipative Phase Transitions

One of the most interesting phenomena in all of physics are phase transitions. They occur due to a competition of system parameters. At the point of a phase transition the system undergoes a radical shift in properties. In classical physics phase transitions are driven by the competition of the energy and entropy terms in the free energy as a function of temperature or density. They have been well and thoroughly described by the Landau theory of phase transitions [6]. Generally, there are two types of phase transitions: first order and continuous phase transitions. First order phase transitions are characterised by a discontinuity in the first derivative of the free energy [6, 50]. They can further possess phase-coexistence. An example is the boiling of water. As all classical phase transitions, it happens at finite temperature with temperature acting as the control parameter. At the critical temperature, part of the water transitions to vapour, while the rest remains at the critical temperature. The total transition of the water to vapour takes a some time.

Continuous, or second-order phase transitions, on the other hand are generally

accompanied by divergences in various properties in the vicinity of the critical point and spontaneous symmetry breaking. The divergences are governed by so-called critical exponents. Thorough experimental and analytical studies of these exponents for many systems showed that they are dependent only on the dimensionality, the symmetry and the range of the interactions. Continuous phase transitions also exhibit spontaneous symmetry breaking. This occurs when the state suddenly loses a symmetry that the governing equation possesses. An example is the phase transition of the classical Ising Model (CIM).

$$\mathcal{H}_{CIM} = -J \sum_{\langle i,j \rangle} s_i s_j. \tag{2.22}$$

Here $s_i = \{\pm 1\}$, J is the interaction strength and $\langle i, j \rangle$ denotes a sum over nearest neighbours. This model has a $\mathcal{Z}_2$ symmetry in the sense that $s_i \to -s_i$ leaves the model invariant. In 2D, this model possesses a phase transition from a disordered to an ordered state. The ordered state will either be $s_i = 1$ or $s_i = -1$ $\forall i$. The $\mathcal{Z}_2$-symmetry of the original model translates one of these states into the other and does not leave them invariant. A plot of the magnetization can be found in Fig. 2.2. It was produced using a simple Metropolis-Hastings Monte Carlo simulation. This method is similar to the one discussed in Sec. 6.4. Given a spin-configuration one flips a random spin and compares the energy of the new configuration with that of the old one. If the new energy is favourable, one retains the new configuration, otherwise one stays with the old configuration. Repeating this step a for $N_s = 10000$ steps converges the system towards the ground-state configuration. One can see that above the critical temperature, the absolute value of the magnetization is zero, while below it, the magnetization is suddenly finite. Around the critical temperature we can observe that the fluctuations in the data increase dramatically. This is a consequence of the competition of two different groundstates. A vanishing magnetization suggests that the state as well as Hamiltonian commutes with the $\mathcal{Z}_2$ symmetry.

In quantum mechanics there exists a similar phenomenon at low temperature. The main difference to classical physics is that it is not the thermal fluctuations due to the energy-entropy competition which drive the phase transition but the quantum

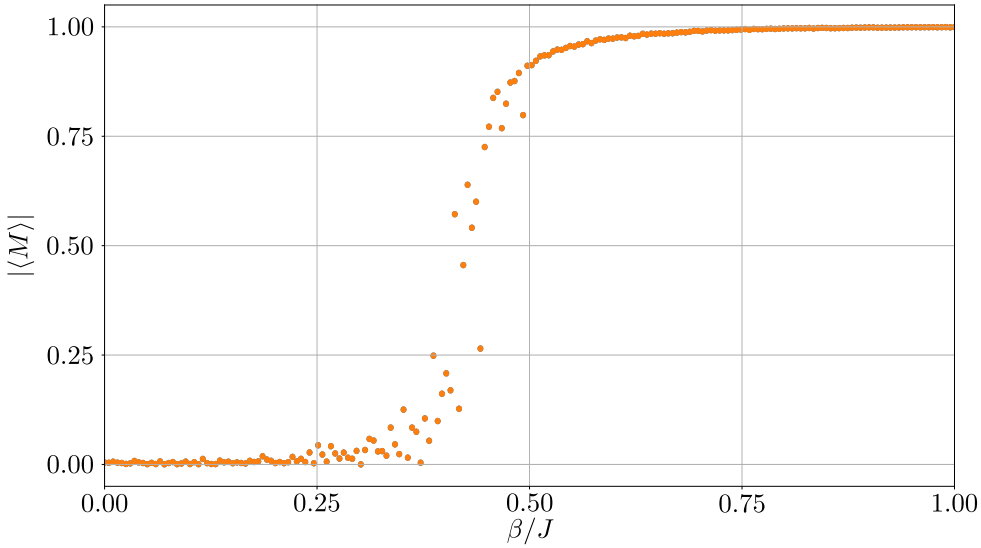

Figure 2.2: This figure shows the absolute value of the magnetization for various inverse temperatures β for the 2D classical Ising model from Eq. 2.22. Fluctuations in the data become largest around $\beta \approx 0.44$ where the system undergoes a continuous phase transition.

fluctuations due to competitions of terms of the Hamiltonian which do not commute. Archetypical models that possess a quantum phase transition are the Transverse Field Ising Model (TFI) and the Quantum Rotor Model, both of which are extensively used and discussed in Ref. [7]. The TFI in particular consists of a nearest-neighbour interaction term as well as a field transverse to the interaction direction

$$\mathcal{H}_{\text{TFI}} = -J \sum_{i=1}^{N-1} \sigma_i^x \sigma_{i+1}^x + h \sum_i \sigma_i^z. \tag{2.23}$$

Here, N is the number of sites, J is the interaction strength and h is the field strength. Note that this model possess the $\mathcal{Z}_2$-symmetry as the classical case: It remains invariant under $\sigma^x \to -\sigma^x$, $\sigma^y \to -\sigma^y$ and $\sigma^z \to \sigma^z$, i.e. a rotation around the z-axis. Competition of these terms leads to a transition between an ordered phase for large interaction and a disordered phase for large field. To be clearer, the interaction term is minimized by parallelly aligned spins in x-direction. There are two such states which are related via a $\mathcal{Z}_2$-symmetry. Hence, this phase spontaneously breaks the $\mathcal{Z}_2$-

symmetry of the model. The field term, on the other hand, is minimized by a state which points along the positive z-direction. This state is invariant under the above symmetry transformation.

The more relevant model in the context of this thesis is the *Lipkin-Meshkov-Glick* model (LMG), see Ref. [22]. Its Hamiltonian is

$$\mathcal{H}_{\mathrm{LMG}} = -\frac{J}{S}\left(S^x\right)^2 - gS^z, \tag{2.24}$$

where S^x and S^z are collective spin operator and S is the total spin size. It describes a single-site spin-S model within a transverse field and a self-interaction. As we will discuss later in more detail, the LMG can be derived from an N-site spin-1/2-model with all-to-all interaction, see Eq. 2.28 and the following paragraphs. It has a first and second-order phase transition, depending on the sign of the self-interaction, which are driven by a competition between the self-interaction term and the magnetic field, see Refs. [8, 9].

In recent years quantum phase transitions in driven-dissipative systems have emerged as a rich and unexplored field of study. Competition between Hamiltonian terms and the bath interaction can drive the system across phase transitions which are connected to their equilibrium counterparts as well as into novel phases that have no equilibrium counterpart. Examples of the former include an open TFI discussed in Ref. [10] as well as the first and second-order transitions of the LMG model discussed at length throughout the first part of this thesis. The best example of novel phases are the aforementioned $\mathcal{PT}$-symmetry breaking transitions explored in Refs. [1, 15]. Another example is the work of Lee et al. [51], in which they were able to stabilize spin-density waves and staggered XY-states which do not exist in the equilibrium model. However, even without explicitly non-equilibrium phenomena, driven dissipative systems offer a host of research opportunities. Much work has been done in the early 2010s by groups around Baumgartner, Buca and Albert on the symmetries of the Lindblad master equation, see Refs. [52–54]. An important result of their work is that there is a difference beteween *(i)* symmetries that commute with the Hamiltonian and all individual jump operators or *(ii)* with the entire Liouvillian itself. The latter is called

a *symmetry* in Ref. [54], a *weak symmetry* in Ref. [53] and a dynamical symmetry in Ref. [52]. An important consequence, in stark contrast to equilibrium systems, is that a mere symmetry of the Liouvillian does not imply a conservation of the symmetry generator, while a *strong symmetry*, *(i)*, implies both a symmetry of the Liouvillian as well as a conservation of the symmetry generator.

There are, however, not just differences between the transitions of open and equilibrium systems. While, there is no Noether Theorem for conserved quantities in open systems and no exceptional points in equilibrium systems, the general idea and framework are quite similar, see Ref. [55]. Whereas in equilibrium systems the relevant quantity is the energy eigenvalue of the Hamiltonian, in dissipative systems it is the complex eigenvalues of the Liouvillian. An equilibrium phase transition between two groundstates occurs as the energy gap between those states closes. Similarly, a dissipative phase transition occurs, as the real part of the Liouvillian gap closes.

More recently, Minganti et al. worked out various properties of the spectrum of the Liouvillian in Ref. [40] by decomposing a generic density matrix into eigenmatrices of the Liouvillian

$$\rho = \frac{\rho_0}{\mathrm{Tr}[\rho_0]} + \sum_{i=1} c_i \rho_i, \tag{2.25}$$

where

$$\mathcal{L}\rho_i = \lambda_i \rho_i \tag{2.26}$$

$$\mathcal{L}\rho_0 = 0. \tag{2.27}$$

They then used that decomposition to investigate how the steady state is approached and which eigenmatrices contribute in first and second-order phase transitions. In particular for second-order phase transitions, they find that two eigenmatrices coalesce at the critical point, rendering the Liouvillian non-diagonalizable.

While most groups mentioned in this thesis, ourselves included, focus on the steady state and its properties, one should not neglect the dynamics that lead to it. In 2016 the authors of Ref. [56] investigated the transient phase in the presence of metastable states and the dynamics in the manifold spanned by these metastable states. These

are just a few of the myriad of studies that have been published on spectral properties of Liouvillians and the general structure of steady states, their symmetries [57], as well as their dynamics and metastability [58–62].

Numerical studies and experiments are vitally important to any scientific research. Experiments are ultimately what decides whether a model is accurate, needs to be amended or even discarded. To be able to compare experimental results with a model, one requires predictions which are derived from that model. There are generally two major ways to achieve this: Analytic investigations or numerical studies. Analytical investigations are the traditional "pen-and-paper" studies. One often tries to derive equations of motion for the model's degrees of freedom or closed expressions for some observables, such as the magnetization or the purity. One can then compare these quantities or trajectories with those from the experiment. The analytic methods which are most relevant to this thesis are mean-field approximations as well as Hosltein-Primakoff transformations, both of which will be further introduced and applied in Ch. 3. Quite often, however, models aren't accessible by analytic studies. In these cases one attempts to numerically simulate the model wholesale via some appropriately chosen method. This results in numerical trajectories in case of semi-classical equations of motion, or expectation values in case of full quantum simulations.

Numerical simulations are no silver bullet which render analytics completely superfluous, however. In fact, they come with an entire host of their own issues. The main problem is the infamous *curse of dimensionality*, i.e. the exponential scaling of the state and system-operator with system size. This strictly limits exact numerical simulations of quantum systems to small system sizes. One can mitigate this problem by approximating the state in various way, see Fig. 2.3. The trade-off of these approximations is some kind of approximation error, which is usually only minimisable by approaching the exact state. Robust numerical methods are thus those which find the optimum between accuracy and memory usage.

One of the most successful numerical methods of the last few decades are matrix product states (MPS) [63]. MPS use the singular value decomposition to break the state of the total system into a product of smaller matrices and find lower rank approx-

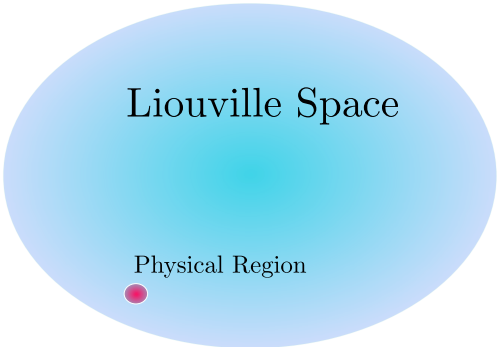

Figure 2.3: Sketch of the Liouville Space. The total number of possible configurations is generally much larger than the number configurations that actually contribute with non-vanishing weight to any physical state. This is the primary reason why most numerical methods work at all: Monte Carlo methods only need to generate a small number of samples form a very restricted set, which allows for fast convergence, while compression algorithms only need to optimize a relatively small number of parameters.

imations for each individual. Each matrix then describes the state of a single site and the correlations with its neighbours. MPS were found to be the theoretical foundation for an even older, very successful numerical method called the *Density Matrix Renormalization Group* introduced in [64]. Ref. [65] introduces the *Time Evolving Block Decimation* (TEBD) algorithm to evolve MPS in time. Due to the way MPS break up the system-state they work best for one dimensional systems, however extensions for two dimensional systems have been introduced [66, 67]. For a more in-depth discussion of MPS and related methods see Ch. 5.

Another method which has proven robust are Quantum Trajectories (QT). While MPS work both in equilibrium and open systems, QT target specifically open quantum systems [27]. QT do away with the need for a full density matrix by stochastically simulating an ensemble of single quantum trajectories. A quantum trajectory in this case refers to the time evolution of a single, pure quantum state. This state is evolved either under a non-hermitian effective Hamiltonian or experiences a sudden jump due to the interaction with the environment. If sufficiently many such trajectories are averaged, one approaches the full dynamics of the density matrix. Due to their stochastic nature, QT were originally introduced as Monte Carlo methods for master equations [68, 69]. For a more detailed explanation of the algorithm, see Ch. 3.

A method introduced in [17] as recently as 2017 are Neural Quantum States (NQS). NQS take inspiration from the parameter structure of neural networks to define an ansatz wave-function. This function is then used in a variational Monte Carlo framework to generate samples and estimate the energy as well as its gradient. This can be used to iteratively update the parameters. Once converged to the energy minimum, the ansatz wavefunction is an approximate representation of the ground-state probability distribution. This can be used to calculate expectation values and even do time evolution. In equilibrium settings, NQS have proven exceptionally powerful and have spawned an entire field of research. In an open system setting, efficient NQS ansatze are still being developed and tested. Part II of this thesis will be primarily concerned with the development and benchmarking of the *Liouville Density Machine* (LDM) ansatz, introduced in [5].

A different method to investigate driven-dissipative two-dimensional systems was employed by the group around Ciuti, see Refs. [70–72]. They developed the Corner-Space Renormalization method for two-dimensional, dissipative systems. In Ref. [70] the group used the dissipative Bose-Hubbard model to illustrate the convergence of their method. In a later study the group applied the method to a dissipative, anisotropic Heisenberg lattice [71]. They investigated the properties of its dissipative phase transition and found that von Neumann entropy increases sharply at the critical point, which is usually characteristic for thermal phase transitions, while the quantum Fisher information, an entanglement witness, also increases across the transition. The dissipative phase transition of the Heisenberg model thus shows behaviour characteristic for both thermal and quantum phase transitions. A further study applying the method was published by the group in 2019 [72]. Here they used a quadratically driven dissipative Bose-Hubbard model to implement a lattice of coupled optical resonators. A main finding is that for small loss rates, the quantum critical point falls into the same universality class of the TFI.

One of the earlier numerical studies of dissipative phase transitions was conducted in Ref. [55]. In their work, the group investigated a central spin system. They do so by deriving semi-classical equations of motion via a Holstein-Primakoff description of

the model. This allowed for an efficient simulation and exploration of the entire phase diagram. It is also noteworthy for detailing the exact differences between thermal, quantum and dissipative phase transitions, how each system is described, what the relevant quantities are and how to recognize a phase transition.

Joshi et al. investigated the dissipative phase transition in a 1-dimensional, $\mathcal{Z}_2$-symmetric, dissipative Transverse Field Ising model using MPS and approximate time integration via TEBD, see Ref. [10]. Each spin of the chain experiences a dissipation given by the σ^--operator. Given such a dissipation a $\sigma^x\sigma^x$-interaction is necessary to preserve the $\mathcal{Z}_2$-symmetry of the equilibrium model, whereas a $\sigma^z\sigma^z$-interaction breaks that symmetry. This is a central point of the second part of this thesis, where we use both models to benchmark our *Liouville Density Machines* ansatz and find that the $\mathcal{Z}_2$-symmetric is much more difficult to efficiently represent.

Experimental studies into dissipative phase transitions have focused mainly on various types of waveguides and cavities, see for example Refs. [3, 4]. In such experiments spin states are modelled by the photon number in each cavity. Inherent cavity loss accounts for the dissipation. Coherent inter-cavity hopping models spin-flip interaction. These platforms allowed for the theoretical proposition and actual realization of a wide array of models. The authors of Ref. [73] for example proposed the realization of driven-dissipative Kerr resonators, subject to one- and two-photon processes. In that study the authors investigated a Kerr non-linearity inside of a photonic cavity subject to coherent one- and two-photon driving as well as one- and two-photon losses. They discovered that this system possesses a dissipative phase transition similar to the one of the Jaynes-Cummings model. A different proposition was made by the authors of [74]. They proposed that an ensemble of superconducting qubits coupled to an array of photonic waveguides could act as a platform for a model of supercorrelated radiance. In the last few years many platforms and methods have been proposed and implemented,such as the 1D circuit QED lattices, fluorescence spectra in driven coupled cavity arrays, the quantum Rabi model to optical hysteresis of semiconductor microcavities to name but a few [74–79]. All of this goes to show the incredible richness of dissipative phase transitions and open quantum systems in general.

As we have mentioned above we are interested in understanding the effects that baths have on the phase of the system. Our way of approaching this question is by contrasting dissipative phase transitions which have an equilibrium counterpart with purely non-equilibrium phase transitions. So far we have discussed $\mathcal{PT}$-symmetry breaking as well as regular dissipative phase transitions. In the next few paragraphs we will discuss the class of models which we will use to engineer both types of phase transitions.

2.4 Collective Spin Models

A particularly interesting class of models are collective spin models. Collective spin models can be regarded as a large collection of spin-1/2 which experience a homogeneous all-to-all interaction. This allows one to write a N-spin-1/2 system as a 1-spin-N/2 system, which is generally much simpler to solve.

As an example consider a two site transverse field Ising model:

$$\mathcal{H} = J\sigma_1^x\sigma_2^x + g\left(\sigma_1^z + \sigma_2^z\right). \tag{2.28}$$

One can always add constant terms to any Hamiltonian, as that merely shifts the eigenvalues but neither changes the level spacings nor the eigenstates. A possible constant term we can add to this Hamiltonian is $\left((\sigma_1^x)^2 + (\sigma_2^x)^2\right)/2 = \mathbb{1}$:

$$\mathcal{H}' = J\sigma_1^x\sigma_2^x + g\left(\sigma_1^z + \sigma_2^z\right) + \frac{J}{2}\left((\sigma_1^x)^2 + (\sigma_2^x)^2\right) \tag{2.29}$$

This completes the square and allows us to rewrite the Hamiltonian in terms of *collective* spin operators $S_j = \sum_i \sigma_i^j$ with $j \in \{x, y, z\}$. The term collective refers to

the fact that the operators act on all spins simultaneously:

$$\mathcal{H}' = J\sigma_1^x\sigma_2^x + g\left(\sigma_1^z + \sigma_2^z\right) + \frac{J}{2}\left((\sigma_1^x)^2 + (\sigma_2^x)^2\right) \tag{2.30}$$

$$= \frac{J}{2}\left(2\sigma_1^x\sigma_2^x + (\sigma_1^x)^2 + (\sigma_2^x)^2\right) + gS_z \tag{2.31}$$

$$= \frac{J}{2}\left(\sigma_1^x + \sigma_2^x\right)^2 + gS_z \tag{2.32}$$

$$= \frac{J}{2}S_x^2 + gS_z. \tag{2.33}$$

We can now readily see that $\left[S_x^2, S^2\right] = \left[S_z, S^2\right] = 0$, where $S^2 = S_x^2 + S_y^2 + S_z^2$ is the total spin operator. Thus, the Hamiltonian conserves total spin. Furthermore, the Hamiltonian is fully symmetric under any permutation of sites. In the two-site case $\mathcal{P}_{12}\left(\sigma_1^x\right) = \sigma_2^x$, however, it generalises to any number of sites. Total spin conservation and permutation symmetry suggests we choose a basis in which both operators are diagonal. One such basis is:

	S^2	S_z	$\mathcal{P}_{12}$
$\|\uparrow\uparrow\rangle$	1	1	1
$\|\uparrow\downarrow\rangle + \|\downarrow\uparrow\rangle$	1	0	1
$\|\downarrow\downarrow\rangle$	1	-1	1
$\|\uparrow\downarrow\rangle - \|\downarrow\uparrow\rangle$	0	0	-1

There are two distinct sectors of the spin, one which lies on the shell of the collective bloch sphere and has total spin $S = 1$, and one which lies at its center and has spin $S = 0$. Symmetry under permutation suggests that the only states the collective spin Hamiltonian can act upon lie on the shell. Thus, we can regard an all-to-all coupled two-site spin-1/2 Hamiltonian as a collective, single-site spin-1 Hamiltonian. This can readily be generalized to any number of sites N.

Two of the most common collective spin models are the Dicke model [80] as well as the Lipkin-Meshkov-Glick Model (LMG) [22]. The Dicke model describes N 2-level atoms interacting with a single bosonic mode and has garnered attention for its prediction of a transition to a superradiant phase [81]. Over the years, various possible

experimental setups have been proposed and realized. See in particular [82] for a cavity QED implementation, where the two lowest lying states of interacting 4-state-atoms are coupled via two Raman channels. The authors of [83, 84] coupled a BEC to an optical cavity and observed self-organization within the BEC as they varied the pump strength. For a more in-depth introduction to the Dicke model in both closed and open system settings, see [85].

The LMG model was first introduced by Lipkin, Meshkov and Glick in 1965 in the context of nuclear physics [22] but has since been shown to map to a vast number of Hamiltonians in many different fields, from bosonic Josephson junctions [86, 87] to nitrogen-vacancy centres in magnetic fields [88]. The mapping between a 2-site Bose-Hubbard model and the LMG model is based on Schwinger bosons, which opens up the possibility to realise the with ultracold atoms in optical lattices [89]. The LMG model, which we have see to arise from a TFI with all-to-all interactions, is described by the following Hamiltonian:

$$\mathcal{H}_{\mathrm{LMG}} = -\frac{J}{S}S_x^2 - gS_z. \tag{2.34}$$

Here S_x and S_z are collective spin operators of total spin S. J gives the strength of the self-interaction term and g the strength of a transverse field. The LMG model has the same $\mathcal{Z}_2$-symmetry as the TFI of Eq. 2.23, i.e. it is invariant under $S_x \to -S_x$, $S_y \to -S_y$ and $S_z \to S_z$.

The model itself can be solved exactly by semi-classical approximations in the thermodynamic limit, see [90]. In this limit, the model possesses a surprisingly rich phase diagram with both a first-order and a second-order phase transition, depending on whether its non-linearity is ferromagnetic or antiferromagnetic, see Fig. 2.4. The figure shows the magnetization of the state along the Z-axis across a scan of g/J for $J = -1$ (a) and $J = 1$ (b). One can see a clear qualitative difference in the behaviour of the magnetisation. For an overall ferromagnetic non-linearity (b), i.e. $J = 1$ the model undergoes two second-order phase transitions at $g/J = \pm 2$. This is marked by a closing of the gap across the entire region $|g/J| < 2$. Across this region, the magnetization changes smoothly from $Z = +1$ at $g/J = -2$ to $Z = -1$ at $g/J = 1$. This is in stark contrast to the anti-ferromagnetic case of plot (a). Here the gap closes at only a single

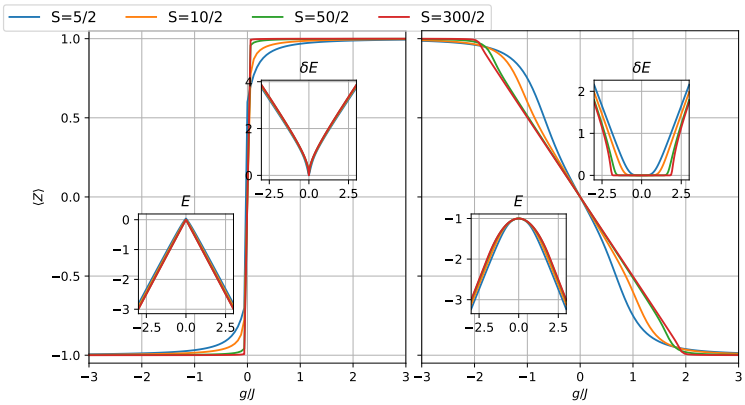

Figure 2.4: This figure shows the first-(a) and second-order (b) phase transition of the LMG model for $J = \pm 1$ respectively for various sizes of the spin.

point, namely $g/J = 0$, and the magnetization jumps discontinuously from $Z = -1$ at $g/J = 0^-$ to $Z = +1$ at $g/J = 0^+$. The scans were repeated for different spin sizes to show how the transitions become sharper towards the semi-classical limit. The entanglement properties of these transitions have been investigated by the Vidal et al. in the dual study [8] (first-order) and [9] (second-order).

While the model is trivially solved by various semi-classical methods, away from the thermodynamic limit finite size effects leave the system highly non-trivial. Extensive research has been done among others by Dusuel et al. [91, 92] on the finite size scaling exponents of various observables and the entanglement entropy [93, 94].

Ribeiro et al have investigated the spectrum of the LMG model in both the thermodynamic limit as well as at finite sizes [95]. A broad discussion of various ground-state collective spin models has been presented by Vidal et al in 2007 [94]. More recently, Huang et al investigated ways to stabilize a state close to the mean-field ground state through a small perturbation [96], which goes to show that even 60 years after its original publication, the ground-state model still offers rich opportunities for discovery.

In 2008 Morrisson and Parkins proposed a dissipative version of the LMG model [97]. They were able to show numerically that the open model inherits the first- and second-order phase transition of the ground-state LMG model. They found however, that the first- and second-order phase transition both appear when just a single parameter is

varied, as opposed to the ground-state model where the order of the phase transition varies as the relative sign of the interaction and field strength flips. In the same year Morrison and Parkins also presented a possible experimental implementation of the dissipative LMG model in [98] which is closely related to the setup presented in [82] for the Dicke model.

A more recent study by Ferreira et al. investigates the dissipative phase transitions of a collective spin model coupled to a metallic surface [99] as well as a magnetic tip. The spin model is well described by the LMG Hamiltonian, while the coupling to the environment could be modelled by a Markovian dissipation term. They found rich phase diagrams depending on whether the magnetic tip is polarized parallel or perpendicular to the applied magnetic field of the LMG model.

2.5 Summary

In this chapter we discussed the literature necessary to understand our results in Ch. 4. The thesis in general and Part I in particular focus on the properties of the steady states of open quantum systems. As described in the introduction, we are keen on understanding how phenomena exclusive to open quantum systems and phenomena from equilibrium physics compete with each other. The model we identified to serve us best is a $\mathcal{PT}$-symmetric LMG dimer with a coherent spin-flip interaction. There are a few reasons for this. For one, as we have seen, individual LMG models are analytically solvable using semi-classic approximations, and possess a rich phase diagram in both closed and open scenarios. These approximations have been found to become exact in the thermodynamic limit. As we have seen, it is further a well established and understood model across a vast number of fields, with various proposed and realized experimental implementations. All of this makes the LMG model a prime candidate as the "equilibrium-analogue" part of our investigation.

The driven-dissipative spin-flip model of [1, 15], on the other hand, is a well understood model possessing $\mathcal{PT}$-symmetry breaking. It has been investigated analytically using Holstein-Primakof approximation, mean-field approximations and brute-force numerical integration. As with the LMG model, experimental realizations have been

proposed. Furthermore, the model has made appearances in the description of time-crystals as well as of lasers, where gain and loss are necessary for the lasing process to exist. In fact the semi-classical model of Eq. 2.14 can be thought of as a 2-mode laser setup. Given how well understood each individual model is, we believe they are perfect candidates to investigate their competition and learn more about the effects of environments on the system.

With the groundwork of this part of the thesis done, we will discuss the methods we employ to investigate this $\mathcal{PT}$-symmetric LMG dimer in Ch. 3. These are primarily the mean-field approximation and linear stability analysis. An important and novel result introduced in the next chapter will be the sufficient condition on the Hamiltonian's symmetries for $\mathcal{PT}$-symmetry breaking to occur. Once the methods we used to investigate the LMG dimer are introduce, we will discuss our results in Ch. 4. That chapter will contain most of the novel findings of this part of the thesis.

Chapter 3

LMG Dimer Theory

In the previous chapter we discussed our motivation for investigating open systems and the $\mathcal{PT}$-symmetric LMG dimer in particular. In this chapter we introduce the methods and approximations we for our investigation. In particular we will discuss the Holstein-Primakoff approximation in Sec. 3.2, which we use to derive analytic expression for various observables. In Sec. 3.3, we will use a mean-field approximation to derive equations of motions for the spin degrees of freedom of the system. In Sec. 3.4 also work out the conditions under a systems symmetries for it to be able to undergo a $\mathcal{PT}$-symmetry breaking phase transition. Finally we discuss quantum trajectories in Sec. 3.5. These will be used along Holstein-Primakoff and mean-field to derive and understand our results.

3.1 The $\mathcal{PT}$-model and the LMG-model

In this part of the thesis we are interested in the $\mathcal{PT}$-symmetric LMG-dimer model. This model possesses both a $\mathcal{PT}$-symmetry breaking phase transition as well as a second-order phase transition, depending on which system parameter is varied. In this section we will briefly discuss the two individual models which we use to construct the LMG-dimer.

3.1.1 $\mathcal{PT}$-model

The first model we consider is the spin-flip- or $\mathcal{PT}$-model given by the following equation:

$$\dot{\rho} = -i[\mathcal{H}_{\mathrm{PT}}, \rho] + \frac{\gamma}{S}\left(\mathcal{D}[S_A^+] + \mathcal{D}[S_B^-]\right) \tag{3.1}$$

$$H_{\mathrm{PT}} = \lambda(S_A^- S_B^+ + S_A^+ S_B^-) \tag{3.2}$$

$$\mathcal{D}[S_A^+] = S_A^+ \rho S_A^- - \frac{1}{2}\{S_A^- S_A^+, \rho\} \tag{3.3}$$

$$\mathcal{D}[S_B^-] = S_B^- \rho S_B^+ - \frac{1}{2}\{S_B^+ S_B^-, \rho\} \tag{3.4}$$

It consists of two collective spins of size S, one of which experiences gain, while the other experiences loss. They are coupled via a collective spin-flip interaction. The model is notable for its $\mathcal{PT}$-symmetry breaking phase transition between the "normal" state, i.e. the dark state of the dissipators and the maximally mixed state. This phase transition is driven by a competition between the coherent and incoherent terms of the Lindblad master equation. For vanishing λ the dissipation dominates, driving the system into the normal state. In the limit of large λ or small dissipation strength γ the Hamiltonian mixes the states of the sites completely, driving the system into the maximally mixed state.

3.1.2 LMG-model

The second model we consider is the dissipative LMG-model. It consists of a single collective spin of size S, which is subject to a field in Z-direction as well as a self-interaction in X-direction. The model possesses a second-order phase transition between the normal state of the dissipation and a symmetry broken phase. It is driven by a competition between the non-commuting terms of the Hamiltonian. For small self-interaction strength J the field term dominates. Since the dark state of the dissipation is an eigenstate of the field term, the system is driven into this state. For large J the quadratic term dominates, which drives the system into the symmetry-broken phase. Other than the $\mathcal{PT}$-symmetry breaking phase transition, this transition is connected

to its equilibrium counter part. As we will see in Ch. 4, we recover the critical J_c of the equilibrium phase transition in the limit of dissipation strength $\gamma \to 0$. As a reminder, the dissipative LMG-model is given by the following Lindblad master equation:

$$\dot{\rho} = -i[\mathcal{H}_{\mathrm{LMG}}, \rho] + \frac{\gamma}{S}\mathcal{D}[S_-] \tag{3.5}$$

$$\mathcal{H}_{\mathrm{LMG}} = -\frac{J}{S}S_x^2 - gS_z \tag{3.6}$$

$$\mathcal{D}[S_-] = S_-\rho S_+ - \frac{1}{2}\{S_+S_-\rho\}. \tag{3.7}$$

The capital-letter S_x-operators are collective spin-operators of size S: $S_x = \sum_i \sigma_i^x$, where the sum runs over all spins of the system. As we have seen in Ch. 2, a system of N all-to-all interacting spin-1/2 can be rewritten as a single spin-S model, where $S = N/2$.

3.2 Hosltein-Primakoff Approximation

In this section we will discuss one of the two semiclassical approximations we will make to simplify the problem, the *Holstein-Primakoff* (HP) approximation. HP maps spin systems to bosonic systems. In the limit of large S one can linearize the transformation which simplifies the resulting bosonic model. One picks some spin state as the vacuum state and linearises around it. HP breaks down if too many states contribute or the system moves too far away from the vacuum state. In the case of the $\mathcal{PT}$-model it allows us to derive analytic expressions for the σ^z-expectation values as well as the purity P.

A spin-state is usually written as $|S, m\rangle$, where S is the total spin and m the magnetization

$$S^2 |S, m\rangle = S(S+1) |S, m\rangle$$
$$S^z |S, m\rangle = m |S, m\rangle .$$

We note that for some total spin S, the magnetization can take any value

$$m = S - n;\ n = 0 \cdots 2S. \tag{3.8}$$

This then looks like a bosonic mode with fixed maximum excitation number n, i.e. for $n = 0$ we have some vacuum-state. We can turn this around and write

$$n = S - m. \tag{3.9}$$

With this we have $|s, m\rangle \to |s, n\rangle$ as well as:

$$|1/2, 1/2\rangle \to |1/2, 0\rangle \tag{3.10}$$

$$|1/2, -1/2\rangle \to |1/2, 1\rangle\,, \tag{3.11}$$

i.e. the *up-state* is the non-excited vacuum state and n counts how far we are away from the vacuum. In the case of spin-1/2 we have only two possible states, up (vacuum) and down (excited). We then have

$$S^z\,|S, m\rangle = m\,|S, m\rangle = (S - n)\,|s, m\rangle = (S - n)\,|S, n\rangle \tag{3.12}$$

$$\Rightarrow S^z\,|n\rangle = (S - n)\,|n\rangle \tag{3.13}$$

$$\Rightarrow S^z = (S - a^\dagger a), \tag{3.14}$$

where in the last line we made use of the bosonic *number operator*. This is also where "expanding around a certain point on the Bloch sphere" comes in. Our choice of the vacuum state tells us what n is counting. Enforcing the correct commutation relations leads to expressions for S^+ and S^- as well

$$S^z = (S - a^\dagger a) \tag{3.15}$$

$$S^+ = \sqrt{2S}\sqrt{1 - \frac{a^\dagger a}{2S}}\,a \tag{3.16}$$

$$S^- = \sqrt{2S}\sqrt{1 - \frac{a^\dagger a}{2S}}\,a^\dagger. \tag{3.17}$$

These equations can be simplified by expanding up to linear order in S:

$$S^z = (S - a^\dagger a) \tag{3.18}$$

$$S^+ = \sqrt{2S}a \tag{3.19}$$

$$S^- = \sqrt{2S}a^\dagger. \tag{3.20}$$

Note that we could as well choose any other point on the Bloch sphere as the vacuum state. Depending on the choice, however the equations might become very unwieldy.

3.2.1 Holstein-Primakoff approximation of the $\mathcal{PT}$-Model

Above, we discussed the basics of HP approximations. Now we will apply it to the $\mathcal{PT}$-model of Eq. 3.1 to derive an analytic expression for the S^z-expectation value as well as the purity.

The HP-transformation, up to lowest order in s and linearised around the $|\uparrow,\downarrow\rangle$-state is defined as

$$S_A^- \approx \sqrt{2S}a^\dagger \tag{3.21}$$

$$S_A^+ \approx \sqrt{2S}a \tag{3.22}$$

$$S_B^- \approx \sqrt{2S}b \tag{3.23}$$

$$S_B^+ \approx \sqrt{2S}b^\dagger. \tag{3.24}$$

Inserting this transformation into the above equation yields

$$H = \lambda 2S(ab + a^\dagger b^\dagger) \tag{3.25}$$

$$D[a] = \gamma 2S(a\rho a^\dagger - \frac{1}{2}a^\dagger a\rho - \frac{1}{2}\rho a^\dagger a) \tag{3.26}$$

$$D[b] = \gamma 2S(b\rho b^\dagger - \frac{1}{2}b^\dagger b\rho - \frac{1}{2}\rho b^\dagger b). \tag{3.27}$$

The problem is now quadratic and bosonic, which vastly simplifies it. We can use this to calculate the equations of motion for various operators and then try to find the steady-state solution. For simplicity we define $G \equiv \lambda 2S$ and $\Gamma \equiv \gamma 2S$. We begin with

the expectation of a:

$$d_t\langle a\rangle = d_t\mathrm{Tr}[\rho a] = \mathrm{Tr}[-i[H,\rho]a] + \mathrm{Tr}[D[a]a] + \mathrm{Tr}[D[b]a] \tag{3.28}$$

The first term is:

$$\mathrm{Tr}[-i[H,\rho]a] = -iG\langle b^\dagger\rangle / \tag{3.29}$$

The dissipative terms can be simplified:

$$\mathrm{Tr}[OD[A]] = \mathrm{Tr}[OA\rho A^\dagger - \frac{1}{2}OA^\dagger A\rho - \frac{1}{2}O\rho A^\dagger A] \tag{3.30}$$

$$= \frac{1}{2}\mathrm{Tr}[([A^\dagger, O]A + A^\dagger[O,A])\rho]. \tag{3.31}$$

$$\tag{3.32}$$

With this we can reduce the derivation of the equations of motion with the dissipator to two simple commutators. The second term of Eq. 3.28 then reads:

$$\mathrm{Tr}[aD[a]] = -\frac{\Gamma}{2}\langle a\rangle. \tag{3.33}$$

The third term obviously vanishes, as we have $[a,b] = [a,b^\dagger] = 0$. Hence, the time derivative of $\langle a\rangle$ is

$$d_t\langle a\rangle = -iG\langle b^\dagger\rangle - \frac{\Gamma}{2}\langle a\rangle. \tag{3.34}$$

Since neither the dissipator nor the Hamiltonian distinguish between a and b, the equation of motion for $\langle b\rangle$ looks quite similar:

$$d_t\langle b\rangle = -iG\langle a^\dagger\rangle - \frac{\Gamma}{2}\langle b\rangle. \tag{3.35}$$

The expectations for the excitations can be derived similarly:

$$d_t\langle a^\dagger a\rangle = \mathrm{Tr}[-i[H,\rho]a^\dagger a] + Tr[a^\dagger aD[a]]. \tag{3.36}$$

Here the third term vanishes again, for the same reasons as above. The first term looks

like

$$[a^\dagger a, H] = [a^\dagger a, ab - a^\dagger b^\dagger] = [a^\dagger a, ab] + [a^\dagger a, a^\dagger b^\dagger] \tag{3.37}$$

$$= -ab + a^\dagger b^\dagger. \tag{3.38}$$

Hence,

$$-iG\mathrm{Tr}[[a^\dagger a, H]\rho] = -iG\langle -ab\rangle + \langle a^\dagger b^\dagger\rangle. \tag{3.39}$$

For the second term we get

$$\mathrm{Tr}[a^\dagger a D[a]\rho] = -\Gamma\langle a^\dagger a\rangle. \tag{3.40}$$

And thus

$$d_t\langle a^\dagger a\rangle = -iG(\langle -ab\rangle + \langle a^\dagger b^\dagger\rangle) - \Gamma\langle a^\dagger a\rangle. \tag{3.41}$$

The same arguments hold again or $d_t\langle b^\dagger b\rangle$:

$$d_t\langle b^\dagger b\rangle = -iG(\langle -ab\rangle + \langle a^\dagger b^\dagger\rangle) - \Gamma\langle b^\dagger b\rangle. \tag{3.42}$$

These equations contain $\langle ab\rangle$ and $\langle a^\dagger b^\dagger\rangle$. Their time derivative is given by:

$$d_t\langle ab\rangle = -iG(1 + \langle b^\dagger b\rangle + \langle a^\dagger a\rangle) - \Gamma\langle ab\rangle \tag{3.43}$$

$$d_t\langle a^\dagger b^\dagger\rangle = iG(1 + \langle b^\dagger b\rangle + \langle a^\dagger a\rangle) - \Gamma\langle a^\dagger b^\dagger\rangle. \tag{3.44}$$

With this we have a system of 8 linear equations that are partially coupled. The interesting equations are the ones for the density $\langle a^\dagger a\rangle$ as that appears in the $\langle S_A^z\rangle$ in spin-basis.

$$\langle S_A^z\rangle = S - \langle a^\dagger a\rangle. \tag{3.45}$$

We note then that $\langle ab\rangle^\dagger = \langle a^\dagger b^\dagger\rangle$, since $[a, b] = 0$, so it is only three coupled equations. Since we care for the steady-state where the time derivatives vanish we set the equations

to zero and try to solve:

$$d_t\langle a^\dagger a\rangle = -iG(-\langle ab\rangle + \langle ab\rangle^\dagger\rangle) - \Gamma\langle a^\dagger a\rangle = 0 \tag{3.46}$$

$$d_t\langle b^\dagger b\rangle = -iG(-\langle ab\rangle + \langle ab\rangle^\dagger) - \Gamma\langle b^\dagger b\rangle = 0 \tag{3.47}$$

$$d_t\langle ab\rangle = -iG(1 + \langle b^\dagger b\rangle + \langle a^\dagger a\rangle) - \Gamma\langle ab\rangle = 0. \tag{3.48}$$

We can rewrite these equations as:

$$-\frac{iG}{\Gamma}(-\langle ab\rangle + \langle ab\rangle^\dagger\rangle) = \langle a^\dagger a\rangle \tag{3.49}$$

$$-\frac{iG}{\Gamma}(-\langle ab\rangle + \langle ab\rangle^\dagger) = \langle b^\dagger b\rangle \tag{3.50}$$

$$-\frac{iG}{\Gamma}(1 + \langle b^\dagger b\rangle + \langle a^\dagger a\rangle) = \langle ab\rangle, \tag{3.51}$$

where it becomes immediately obvious that $\langle a^\dagger a\rangle = \langle b^\dagger b\rangle$. This simplifies the system of equation to:

$$-\frac{iG}{\Gamma}(-\langle ab\rangle + \langle ab\rangle^\dagger\rangle) = \langle a^\dagger a\rangle \tag{3.52}$$

$$-\frac{iG}{\Gamma}(1 + 2\langle a^\dagger a\rangle) = \langle ab\rangle, \tag{3.53}$$

for readability we define $ix := i\frac{G}{\Gamma}$ and insert the 2nd equation into the first:

$$\langle a^\dagger a\rangle = \frac{2x^2}{(1-4x^2)} \tag{3.54}$$

Reinserting the original definitions $x = \frac{G}{\Gamma}$ as well as $G = \lambda 2S$ and $\Gamma = \gamma 2S$ yields

$$\langle a^\dagger a\rangle = \frac{2\lambda^2}{\gamma^2(1-4\left(\frac{\lambda}{\gamma^2}\right)^2)} = \frac{2\lambda^2}{(\gamma^2-4\lambda^2)}. \tag{3.55}$$

This expression suggests a phase transition at $\gamma = 2g$. For $\gamma > 2g$ we have a well defined excitation number, while it diverges at the point of transition. For $\gamma < 2g$ we have a negative excitation number which suggests a breakdown of the Holstein-Primakoff approximation.

At this stage we should note that there are two different conventions for the dissipative part of the Liouvillian which one can encounter in the literature:

$$\mathcal{D}_1(A) = \gamma \left(A\rho A^\dagger - \frac{1}{2}\{A^\dagger A, \rho\} \right) \tag{3.56}$$

$$\mathcal{D}_2(A) = \gamma' \left(2A\rho A^\dagger - \{A^\dagger A, \rho\} \right), \tag{3.57}$$

where $\gamma' = \frac{\gamma}{2}$. These are ultimately equivalent but lead to rescaling of the dissipation strength. In this chapter we use the first convention, however the code base we employed uses the second. Thus while the our calculations suggest a phase transition at $\gamma = 2\lambda$, we will in fact see it at $\gamma = \lambda$ in our results.

3.2.2 Holstein-Primakoff Approximation of the Purity

In this section we will use the Holstein-Primakoff approximation of the the previous section to derive an analytic expression for the purity of the state. We know that Holstein-Primakoff works best the closer we are to the pure state we linearized around. We thus expect the purity to be largest in the region where Holstein-Primakoff is applicable and for it drop steeply close to the phase transition. To calculate the purity we make use of the results obtained in Ref. [100]. They derived that the purity of a Gaussian state is fully characterized by its covariance matrix $\boldsymbol{\sigma}$. A Gaussian state refers to a state which is fully characterized by its first and second statistical moments x_i and p_i ,where i is the site index and $p_i = p_i^*$ is defined to be anti-hermitian. In the case of a two-mode bosonic system we then have:

$$x_1 = \frac{1}{\sqrt{2}} \left(a + a^\dagger \right) \tag{3.58}$$

$$p_1 = \frac{1}{\sqrt{2}} \left(a - a^\dagger \right) \tag{3.59}$$

$$x_2 = \frac{1}{\sqrt{2}} \left(b + b^\dagger \right) \tag{3.60}$$

$$p_2 = \frac{1}{\sqrt{2}} \left(b - b^\dagger \right) \tag{3.61}$$

With this the covariance matrix for a two-site system is given by

$$\sigma_{ij} = \frac{1}{2}\langle X_i X_j + X_j X_i\rangle - \langle X_i\rangle\langle X_j\rangle, \tag{3.62}$$

where $\vec{X} = (x_1, p_1, x_2, p_2)^T$ is the vector of all relevant moments. The purity of the state of such a 2-mode bosonic system is then given by

$$P(\boldsymbol{\sigma}) = \frac{1}{4\sqrt{|\boldsymbol{\sigma}|}}, \tag{3.63}$$

where $|\boldsymbol{\sigma}|$ is the determinant of the covariance matrix.

We begin by giving a step-by-step derivation of the covariance matrix. As covariance matrices are necessarily symmetric, we will restrict ourselves to the upper triangle, however. The first term of the covariance matrix is given by:

$$\begin{aligned}
\sigma_{11} &= \langle x_1 x_1\rangle - \langle x_1\rangle\langle x_1\rangle && (3.64)\\
&= \frac{1}{2}\langle aa + 2a^\dagger a + a^\dagger a^\dagger + 1\rangle - \frac{1}{2}\left(\langle a + a^\dagger\rangle\right)^2 && (3.65)\\
&= \frac{1}{2}\left(\langle aa\rangle + 2\langle a^\dagger a\rangle + \langle a^\dagger a^\dagger\rangle + 1\right) - \frac{1}{2}\left(\langle a + a^\dagger\rangle\right)^2. && (3.66)
\end{aligned}$$

First we note that $(aa)^\dagger = a^\dagger a^\dagger$. We also note that we know the analytic expression for $\langle a^\dagger a\rangle$ of Eq. 3.55:

$$\langle a^\dagger a\rangle = \frac{2\lambda^2}{(\gamma^2 - 4\lambda^2)}. \tag{3.67}$$

The steady-state expression for $\langle a^\dagger a^\dagger\rangle$ can be derived in a similar fashion to what we did above, i.e. derive the equation of motion for $\langle a^\dagger a^\dagger\rangle$, set it to 0, and solve for the moment:

$$\begin{aligned}
\frac{d}{dt}\langle a^\dagger a^\dagger\rangle &= -2i\lambda\langle a^\dagger b\rangle - \gamma\langle a^\dagger a^\dagger\rangle = 0 && (3.68)\\
&\Rightarrow \langle a^\dagger a^\dagger\rangle = -\frac{2i\lambda}{\gamma}\langle a^\dagger b\rangle && (3.69)
\end{aligned}$$

Similar processes for other moments yields:

$$\langle a^\dagger b\rangle = \frac{i\lambda}{\gamma}\left(\langle bb\rangle - \langle a^\dagger a^\dagger\rangle\right) \tag{3.70}$$

$$\langle bb\rangle = -\frac{2i\lambda}{\gamma}\langle a^\dagger b\rangle. \tag{3.71}$$

Inserting the expressions for $\langle a^\dagger a^\dagger\rangle$ and $\langle bb\rangle$ into $\langle a^\dagger b\rangle$ yields:

$$\frac{2\lambda^2}{\gamma^2}\langle a^\dagger b\rangle = \langle a^\dagger b\rangle, \tag{3.72}$$

which suggests that $\langle a^\dagger b\rangle = 0$, which means $\langle a^\dagger a^\dagger\rangle = \langle aa\rangle^\dagger = 0$ as well. Next up we need to look at the last term of σ_{11}:

$$\left(\langle a + a^\dagger\rangle\right)^2 = \left(\langle a\rangle^2 + 2\langle a^\dagger\rangle + \langle a^\dagger\rangle^2\right). \tag{3.73}$$

Again, we derive all necessary analytic steady-state expressions:

$$\langle a\rangle = -\frac{2i\lambda}{\gamma}\langle b^\dagger\rangle \tag{3.74}$$

$$\langle b^\dagger\rangle = -\frac{2i\lambda}{\gamma}\langle a\rangle. \tag{3.75}$$

Inserting the latter into the first yields:

$$\langle a\rangle = -\frac{4\lambda^2}{\gamma^2}\langle a\rangle, \tag{3.76}$$

which again suggests that $\langle a\rangle = 0$. With this we can finally write the first element of the covariance matrix as:

$$\sigma_{11} = \frac{2\lambda^2}{(\gamma^2 - 4\lambda^2)} + \frac{1}{2}. \tag{3.77}$$

We now progress along the diagonal with σ_{22}:

$$\sigma_{22} = \langle p_1 p_1 \rangle - \langle p_1 \rangle \langle p_1 \rangle \tag{3.78}$$

$$= \frac{1}{2}\langle aa - 2a^\dagger a + a^\dagger a^\dagger - 1 \rangle + \frac{1}{2}\left(\langle a - a^\dagger \rangle\right)^2 \tag{3.79}$$

$$= \frac{1}{2}\left(\langle aa \rangle - 2\langle a^\dagger a \rangle + \langle a^\dagger a^\dagger \rangle - 1\right) + \frac{1}{2}\left(\langle a - a^\dagger \rangle\right)^2. \tag{3.80}$$

Many of the arguments from the previous derivation apply here. In particular, we now know that $\left(\langle a - a^\dagger \rangle\right)^2 = 0$ and that $\langle aa \rangle = \langle aa \rangle^\dagger = 0$ as well. This leaves us with:

$$\sigma_{22} = -\frac{2\lambda^2}{(\gamma^2 - 4\lambda^2)} - \frac{1}{2}. \tag{3.81}$$

By exactly the same arguments we arrive at expressions for σ_{33} and σ_{44}:

$$\sigma_{33} = \frac{2\lambda^2}{(\gamma^2 - 4\lambda^2)} + \frac{1}{2} \tag{3.82}$$

$$\sigma_{44} = -\frac{2\lambda^2}{(\gamma^2 - 4\lambda^2)} - \frac{1}{2}. \tag{3.83}$$

We now move on to the off-diagonal elements. As before, most of the work has been done during the derivation of the first element, and we will just have to put everything into its place. We begin with σ_{12}:

$$\sigma_{12} = \frac{1}{2}\langle x_1 p_1 + p_1 x_1 \rangle - \langle x_1 \rangle \langle p_1 \rangle. \tag{3.84}$$

As we have shown above $\langle a \rangle = 0$ in the steady state. This makes terms like $\langle X_i \rangle \langle X_j \rangle$ vanish and we will from now on neglect them in our derivations. The remaining term then looks like:

$$\sigma_{12} = \frac{1}{2}\langle x_1 p_1 + p_1 x_1 \rangle \tag{3.85}$$

$$= \frac{1}{4}\langle (a + a^\dagger)(a - a^\dagger) + (a - a^\dagger)(a + a^\dagger) \rangle \tag{3.86}$$

$$= \frac{1}{4}\left(2\langle aa \rangle - 2\langle a^\dagger a^\dagger \rangle\right) = 0. \tag{3.87}$$

This tells us that both σ_{12} and σ_{34} vanish. The next terms we will derive are σ_{13} and σ_{31}:

$$\sigma_{13} = \frac{1}{2}\langle x_1 x_2 + x_2 x_1 \rangle \tag{3.88}$$

$$= \langle x_1 x_2 \rangle \qquad = \frac{1}{2}\langle ab + a^\dagger b^\dagger + ab^\dagger + a^\dagger b \rangle, \tag{3.89}$$

due to $[a, b] = [a, b^\dagger] = 0$. We know from before that $\langle ab^\dagger \rangle = \langle a^\dagger b \rangle^\dagger = 0$. This leaves us with the task of finding steady-state expressions for $\langle ab \rangle$. We know from the previous section that

$$\langle ab \rangle = \frac{-i\lambda\gamma}{(\gamma^2 - 4\lambda^2)}. \tag{3.90}$$

With this we now have that

$$\sigma_{13} = \langle ab \rangle + \langle ab \rangle^\dagger \tag{3.91}$$

$$= \frac{-i\lambda\gamma}{(\gamma^2 - 4\lambda^2)} + \frac{i\lambda\gamma}{(\gamma^2 - 4\lambda^2)} = 0. \tag{3.92}$$

The next element we look at is σ_{14}, where we again omit the term $\langle x_1 \rangle \langle p_2 \rangle$:

$$\sigma_{14} = \frac{1}{2}\langle ab - a^\dagger b^\dagger - ab^\dagger + a^\dagger b \rangle. \tag{3.93}$$

$\langle ab^\dagger \rangle$ as well as $\langle a^\dagger b \rangle^\dagger$ vanish as we before and we just derived $\langle ab \rangle$. with this we can easily see that:

$$\sigma_{14} = \frac{-i\lambda\gamma}{(\gamma^2 - 4\lambda^2)}. \tag{3.94}$$

Similarly, we get for σ_{23}:

$$\sigma_{23} = \frac{-\lambda\gamma}{(\gamma^2 - 4\lambda^2)}. \tag{3.95}$$

With this we finally have all elements of $\boldsymbol{\sigma}$:

$$\boldsymbol{\sigma} = \begin{pmatrix} \frac{2\lambda^2}{(\gamma^2-4\lambda^2)} + \frac{1}{2} & 0 & 0 & \frac{-i\lambda\gamma}{(\gamma^2-4\lambda^2)} \\ 0 & -\frac{2\lambda^2}{(\gamma^2-4\lambda^2)} - \frac{1}{2} & \frac{-\lambda\gamma}{(\gamma^2-4\lambda^2)} & 0 \\ 0 & \frac{-\lambda\gamma}{(\gamma^2-4\lambda^2)} & \frac{2\lambda^2}{(\gamma^2-4\lambda^2)} + \frac{1}{2} & 0 \\ \frac{-i\lambda\gamma}{(\gamma^2-4\lambda^2)} & 0 & 0 & -\frac{2\lambda^2}{(\gamma^2-4\lambda^2)} - \frac{1}{2} \end{pmatrix}. \tag{3.96}$$

This is now the complete covariance matrix of the steady-state of the driven-dissipative $\mathcal{PT}$-model of Eq. 3.1.

The determinant of this matrix is of the form $|\boldsymbol{\sigma}| = a^4 + b^4 + 2a^2b^2$, where a are the diagonal elements and b are the off-diagonal elements. Inserting yields the determinant

$$|\boldsymbol{\sigma}| = \frac{\gamma^4}{16(\gamma^2 - \lambda^2)^2}. \tag{3.97}$$

With this the purity of Eq. 3.63 is:

$$P = 1 - \frac{4\lambda^2}{\gamma^2}. \tag{3.98}$$

This is the result found in Ref. [1]. It is a closed expression for the purity of the steady state for the parameter range in which HP is applicable. The purity is largest at the point we linearized around in the Holstein-Primkaoff approximation, i.e. the normal state $|\uparrow,\downarrow\rangle$. As λ grows and the system moves further and further away from the vacuum state the purity begins to decrease. At the point of the phase transition, $\gamma = 2\lambda$, in our convention, it becomes 0. Afterwards, when the system enters the maximally mixed state, i.e. is furthest from the chosen vacuum state, the purity becomes negative, indicating that Holstein-Primakoff breaks down.

In summary, in this section we discussed the Hosltein-Primakoff approximation and applied it to the $\mathcal{PT}$-model. This allowed us to derive analytic expressions for the critical parameters as well for the purity, bearing in mind the rescaling of the dissipation strength due to the choice of convention. We will use these expressions in the next chapter when we investigate the $\mathcal{PT}$-symmetric LMG dimer in more detail.

3.3 Mean-field Equations

Mean-field approximations are powerful analytical tools. They have been used as early as 1907 by Pierre Curie and Pierre Weiss to describe phase transitions [101]. Mean-field theory generally works by breaking up correlations within the system in one way or another. Originally, one assumed that sites don't interact directly, but that all neighbours of a site form an average, or *mean*, field, which acts on it. This usually leads to equations which need to be solved self-consistently, as each site appears in the mean-field of each other site. The mean-field approximation we employ is simpler and requires no self-consistency. We will calculate the time derivatives of the expectation values of the spin components and will assume that correlations break apart, i.e.

$$\langle AB\rangle = \langle A\rangle\langle B\rangle. \tag{3.99}$$

This will lead to a set of coupled differential equations whose fixed points will be mean-field approximations of the steady-states of the full open quantum model.

Naturally, such a crass approximation raises the question of its validity. Generally, mean-field approximations will only give a first, qualitative idea of the real behaviour of a model. However, the approximation will get better as the strength of correlations decreases. This is often the case for a large spatial dimension or strong long-range interactions. The models we care about possess an infinite-range interaction and large, i.e. slow spins, and should in principle be well explained by mean-field approximations. We will use the resulting non-linear coupled mean-field equations to find the steady-state values of the spin components as well as to generate the linear stability phase diagram, which we will discuss in detail in Ch. 4.

3.3.1 Mean-field Equations of the LMG-model

We begin with a detailed derivation of the mean-field equations of motion for the LMG model of Eq. 3.5. Since it is an effective single-site model, we only require three equations of motion. The discussion of this model will transfer directly to the $\mathcal{PT}$-model in the next section.

We calculate the time-derivative of the expectation values of $\langle S_x\rangle$,$\langle S_y\rangle$ as well as $\langle S_z\rangle$. To this end we need the following two identities. The first is the well known commutator relation:

$$[A, BC] = [A, B]\, C + B\, [A, C]\,. \tag{3.100}$$

The other is a simplification of the trace over the dissipator $\mathcal{D}[A]$:

$$\mathrm{Tr}\left[O\mathcal{D}[A]\right] = \frac{1}{2}\mathrm{Tr}\left[\left(\left[A^\dagger, O\right] A + A^\dagger\left[O, A\right]\right)\rho\right], \tag{3.101}$$

which reduces the whole derivation to the calculation of two commutators of spin-operators. We begin with S_x:

$$\frac{d}{dt}\langle S_x\rangle = \mathrm{Tr}\left[\dot{\rho} S_x\right] \tag{3.102}$$

$$= \mathrm{Tr}\left[-i\left[\mathcal{H}, \rho\right] S_x\right] + \mathrm{Tr}\left[\frac{\gamma}{S}\mathcal{D}[S_-]S_x\right]. \tag{3.103}$$

We begin with the Hamiltonian term:

$$-i\mathrm{Tr}\left[[\mathcal{H}, \rho], S_x\right] = g\langle S_y\rangle. \tag{3.104}$$

The dissipative part follows Eq.3.101 and will require the mean-field approximation Eq. 3.99 for the first time:

$$\mathrm{Tr}\left[S_x\frac{\gamma}{S}\mathcal{D}[S_-]\right] = \frac{\gamma}{2S}\left(\langle S_z S_x\rangle + \langle S_x S_z\rangle - \langle S_x\rangle\right) \tag{3.105}$$

We can now use the mean-field approximation, $\langle S_z S_x\rangle = \langle S_x\rangle\langle S_z\rangle$, and finally arrive at:

$$\mathrm{Tr}\left[S_x\frac{\gamma}{S}\mathcal{D}[S_-]\right] = -\frac{\gamma}{2S}\langle S_x\rangle + \frac{\gamma}{S}\langle S_x\rangle\langle S_z\rangle. \tag{3.106}$$

With this the time derivative of the S_x-expectation value finally looks like this:

$$\langle\dot{S_x}\rangle = g\langle S_y\rangle - \frac{\gamma}{2S}\langle S_x\rangle + \frac{\gamma}{S}\langle S_x\rangle\langle S_z\rangle. \tag{3.107}$$

Note that this equations still scales with S. However, we wish that expectations values

of spins are confined to the range $[-1, 1]$. Hence, we will normalize $\langle \dot{S}_x \rangle$ by S and define $X := \langle S_x \rangle / S$. With this we get the following equation for $\dot{X}$:

$$\dot{X} = \frac{g}{S}\langle S_y \rangle - \frac{\gamma}{2S^2}\langle S_x \rangle + \frac{\gamma}{S^2}\langle S_x \rangle \langle S_z \rangle \tag{3.108}$$

$$= gY + \gamma XZ. \tag{3.109}$$

Note that we neglected the term $\gamma X/S$ as that term vanishes as S tends to infinity. In a fashion completely analogous to this derivation we can arrive at equations for $\dot{Y}$ and $\dot{Z}$ as well. This leads us to the following set of coupled, differential equations:

$$\dot{X} = gY + \gamma ZX \tag{3.110}$$

$$\dot{Y} = -gX + 2JZX + \gamma ZY \tag{3.111}$$

$$\dot{Z} = -2JYX - \gamma(X^2 + Y^2). \tag{3.112}$$

Here we have exchanged a linear full quantum description of the dynamics of the density matrix to a non-linear set of equations for the spin-degrees of freedom. These equations can now be analysed with methods from dynamical system theory, see Sec. 3.3.3 for a description of linear stability analysis.

These equations are always solved by the point $X = 0$ $Y = 0$ $Z = -1$, which we refer to as the normal state. In terms of γ the critical interaction strength at which this state becomes unstable is given by:

$$\frac{J_c}{g} = -\frac{(\gamma^2 + 1)}{2}. \tag{3.113}$$

More concretely, for $\gamma/g = 0.5$ this state is stable for $J/g > -0.625$. For $J/g < -0.625$

the set of solutions is given by

$$X = \pm\sqrt{\frac{-g^2\Xi^2 + \gamma^2}{2J\gamma\Xi}} \tag{3.114}$$

$$Y = -X\Xi \tag{3.115}$$

$$Z = \frac{g\Xi}{\gamma} \tag{3.116}$$

where $\Xi = 2J + \sqrt{4J^2 - 1}$.

These equations determine the time-evolution of the spin-components, sometimes also referred to as the flow through the phase space, where the surface of the Bloch sphere is the phase space of a spin. "Flow" refers to the fact that the equations describe the rate of change at every point of the surface, and hence, how an imagined object will flow across the surface. In the full quantum picture, described by the Lindblad master equation Eq. 2.12, we are generally interested in its steady-state, i.e. the state which remains constant in time. In the context of this mean-field approximation this translates to finding the point p on the surface of the Bloch sphere where the rate of change vanishes, i.e.

$$\frac{d\bar{p}^*}{dt} = 0, \tag{3.117}$$

where $\bar{p}^*$ is referred to as a *fixed point*, or *solution* of the system of equations. To analyse the "linear stability" of a solution, we can use employ the Jacobian matrix of the system of equations, see Sec. 3.3.3. We will make extensive use of this technique in Ch. 4 to determine a first approximation of the phase diagram. The Jacobian is the matrix of first order derivatives:

$$\mathcal{J}(X,Y,Z) = \begin{pmatrix} Z\gamma & g & X\gamma \\ -g + 2JZ & Z\gamma & 2JX + Y\gamma \\ -2JY - 2\gamma X & -2JX - 2\gamma Y & 0 \end{pmatrix}. \tag{3.118}$$

In this section we made use of a mean-field approximation to find equations of motion for the spin-degrees of freedom of the LMG-model. We further derived the Jacobian of this set of equations, which will allow us to assess the stability of a given

solution, i.e. whether some initial condition will converge towards it with time or be driven away from it.

3.3.2 Mean-field Equations of the $\mathcal{PT}$-model

The derivation of the equations of motion for the $\mathcal{PT}$-model of Eq. 3.1 uses the same concepts developed in the last section, with the added complication that we now have two spins interacting. The derivation of the other components will then follow the exact same structure, and, due to parity-symmetry of the Hamiltonian, the second spin will be identical up to a change in indices. The equations of motions for the six degrees of freedom are

$$\dot{X}_a = \lambda Z_a Y_b + \gamma X_a Z_a \tag{3.119}$$

$$\dot{Y}_a = -\lambda Z_a X_b + \gamma Y_a Z_a \tag{3.120}$$

$$\dot{Z}_a = \lambda(X_a Y_b - Y_a X_b) - \gamma(X_a^2 + Y_a^2) \tag{3.121}$$

$$\dot{X}_b = \lambda Z_b Y_a - \gamma X_b Z_b \tag{3.122}$$

$$\dot{Y}_b = \lambda Z_b X_a - \gamma Y_b Z_b \tag{3.123}$$

$$\dot{Z}_b = \lambda(X_a Y_b - Y_a X_b) + \gamma(X_b^2 + Y_b^2). \tag{3.124}$$

Note the different signs in the dissipation of the two sites. This suggests, that a hermitian conjugation of a term in the dissipator of the Lindblad master equation leads to a flipped sign of γ on the level of the mean-field equations. The derivation of the Y and Z components of either spin are completely analogous. This set of equations again has a normal state $X_{a/b} = Y_{a/b} = 0,\ Z_{a/b} = \pm 1$. It is, however not easy to see where its stable. This is a question we consider in more detail in the next chapter. With this, we have now derived a set of equations, which describe the behaviour of the spin-degrees of freedom in the semiclassical limit. Furthermore, we have now seen how to derive the mean-field equations of motion as well as the Jacobian. In the next chapter we use this

knowledge to present the mean-field equations of the full LMG-dimer model

$$\mathcal{H} = \mathcal{H}_{\mathrm{LMG,a}} \otimes \mathbb{1} + \mathbb{1} \otimes \mathcal{H}_{\mathrm{LMG,b}} + \mathcal{H}_{\mathrm{PT}} \tag{3.125}$$

$$\mathcal{D}[S_a^-] = S_a^- \rho S_a^+ - \frac{1}{2}\{S_a^+ S_a^-, \rho\} \tag{3.126}$$

$$\mathcal{D}[S_b^+] = S_b^+ \rho S_b^- - \frac{1}{2}\{S_b^- S_b^+, \rho\}. \tag{3.127}$$

Solving these equations will allow us to get a qualitative understanding of the steady-states of the model in various different regimes. To get a first impression of the entire phase diagram we will make use of the Jacobian. If the system of equations undergoes a *bifurcation*, i.e. a phase transition in physicists terms, the number of stable solutions will change. Solving the systems of equations for a large number of initial conditions while varying the system parameters will then allow us to generate a "linear stability phase diagram".

3.3.3 Linear Stability Analysis

In this section we will give a brief introduction to linear stability analysis as we employ it in Sec. 4.4.2. Linear stability analysis uses the eigenvalues of the Jacobian Matrix, evaluated at a specific fixed point $\vec{p}^*$ to determine whether that point is attractive or repulsive. If the fixed point is repulsive, i.e. if all points around it will be driven further away from it over time, we say it is an unstable solution. An unstable fixed point still solves the the equations, in the sense that

$$\frac{d\vec{p}^*}{dt} = 0, \tag{3.128}$$

however it will either never be reached, or a tiny perturbation will lead to fast divergence from it. Attractive fixed points are said to be stable for the same reason. They attract all points around them and can never be left. To see how the Jacobian can help us evaluate the linear stability of a fixed point consider the following. Assume we are given a vector $\vec{p}$ of the co-ordinates that describe the system and some non-linear function

$F(\vec{p})$. Then the time evolution of $\vec{p}$ is given by:

$$\frac{d\vec{p}}{dt} = \vec{F}(\vec{p}). \tag{3.129}$$

We call a fixed point a point that no longer changes under time evolution. Such a *fixed point* of the system $\vec{p}^*$ must always satisfy the condition

$$\frac{d\vec{p}^*}{dt} = 0. \tag{3.130}$$

We can now investigate whether the solution is stable by adding a finite but small perturbation, $\tilde{p}(t) = \vec{p}^* + \delta_{\vec{p}}$ to it and see how the perturbation grows with time:

$$\frac{d\tilde{p}}{dt} = \frac{d(\vec{p}^* + \delta_{\vec{p}})}{dt} = \frac{d\delta_{\vec{p}}}{dt} = \vec{F}(\vec{p}^* + \delta_{\vec{p}}). \tag{3.131}$$

This tells us that we can get an expression for the time evolution of the perturbation by performing a Taylor expansion of the function $\vec{F}(\tilde{p})$ around the point $\vec{p}^*$:

$$\vec{F}(\vec{p}^* + \delta_{\vec{p}})|_{\vec{p}^*} = \vec{F}(\vec{p}^*) + \left.\frac{dF_i}{dp_j}\right|_{\vec{p}^*} \delta_{\vec{p}} + \mathcal{O}(\delta_{\vec{p}}^2). \tag{3.132}$$

The first term on the right-hand side vanishes by definition, while the second term is the Jacobian evaluated at the fixed point $\vec{p}^*$

$$\mathcal{J}(\vec{p}^*) := \left.\frac{dF_i}{dp_j}\right|_{\vec{p}^*} = \left.\begin{pmatrix} \frac{dF_1}{dp_1} & \dots & \frac{dF_1}{dp_n} \\ \vdots & \ddots & \vdots \\ \frac{dF_n}{dp_1} & \dots & \frac{dFp_n}{dp_n} \end{pmatrix}\right|_{\vec{p}^*}. \tag{3.133}$$

With this we can now see that the time-evolution of the perturbation is, in linear order, determined by the Jacobian:

$$\frac{d\delta_{\vec{p}}}{dt} = \mathcal{J}(\vec{p}^*). \tag{3.134}$$

From now on the explicit dependency of the Jacobian on the fixed point will be dropped to minimize clutter. The formal solution to this equation is

$$\delta_{\vec{p}}(t) = e^{\mathcal{J}t}\delta_{\vec{p}}(0). \tag{3.135}$$

We can always expand the vector $\delta_{\vec{p}}(0)$ in the eigenbasis of the Jacobian:

$$\delta_{\vec{p}}(0) = \sum_i c_i(0)\phi_i, \tag{3.136}$$

where c_i are the expansion coefficient and ϕ_i is the ith eigenstate of the Jacobian *evaluated at a specific point*:

$$\mathcal{J}\phi_i = j_i\phi_i. \tag{3.137}$$

With this the perturbation at time t becomes:

$$\delta_{\vec{p}}(t) = \sum_i c_i(0)e^{j_i t}\phi_i. \tag{3.138}$$

From this equation it becomes obvious that a solution to the original problem can only be *linearly stable* if the real parts of all eigenvalues of the Jacobian, evaluated at that solution, are smaller than zero. Otherwise any small perturbation will drive the systems exponentially fast away from the solution. Also note, that linear stability analysis does not recognize limit cycles or chaos as stable solutions. This can lead to various phases being invisible in the linear stability phase diagram.

3.4 $\mathcal{PT}$-Symmetry and Stability of the Maximally Mixed State

In the previous sections we talked about various transformations one can do to make the $\mathcal{PT}$-model more accessible. We found in the mean-field case a set of six equations of which we know has a normal phase in the limit of vanishing interaction. Here, we will discuss the case of large interaction strength. We will see that the system possesses a maximally mixed phase in this limit which suggests a phase transition occurs at some

finite interaction strength. We will use this argument to better understand some phases of the the phase diagrams presented in Ch. 4

To investigate this limit we perform something akin to a linear stability analysis, i.e. we assume to be in the maximally mixed state and investigate the time evolution of an infinitesimal perturbation. From this we derive the conditions under which the maximally mixed state is stable. This section follows closely the derivation from Ref. [1]. They found that certain systems whose Lindblad operators are linked via a parity-symmetry possesses a $\mathcal{PT}$-symmetry breaking phase transition akin to what was found in the non-Hermitian systems we discussed in Ch. 2. In particular they required for the Liouvillian that

$$\mathcal{L}\left[\mathcal{PT}(\mathcal{H}); \mathcal{PT}(j_a), \mathcal{PT}(j_b)\right] = \mathcal{L}\left[\mathcal{H}; j_a, j_b\right]. \tag{3.139}$$

Here, $\mathcal{L}\left[\mathcal{H}; j_a, j_b\right]$ refers to the super-operator that appears in the Lindblad master equation Eq. 2.12. It depends on the Hamiltonian $\mathcal{H}$ as well as the set of jump-operators j_a and j_b acting on subsystem a and b respectively. The symmetries themselves act upon an operator as

$$\mathcal{PT}(O_a) = O_b^\dagger. \tag{3.140}$$

Here, $\mathcal{P}$ is the spatial parity symmetry, which exchanges two sites. $\mathcal{T}$ refers to the time-inversion symmetry. It exchanges gain and loss, e.g. $\sigma^+ \to \sigma^-$ and vice versa. Both the $\mathcal{P}$ and the $\mathcal{T}$ symmetries represent the $\mathcal{Z}_2$-symmetry group, i.e. $\mathcal{P}^2 = \mathcal{T}^2 = \mathbb{1}$. Given this symmetry, the Liouvillian will have a maximally mixed steady state, which lies in a different symmetry sector than the normal state.

A question we found interesting was what the precise conditions on the system and the symmetry are, and if we could generalize it to $\mathcal{Z}_n$-like symmetries. This would lead to a prescription for constructing OQS with possible novel phases and transitions. We find that a sufficient condition for a $\mathcal{PT}$-like phase transition is that the relevant symmetry is part of the *center* of the Hamiltonians symmetry group. This means that the relevant symmetry commutes with all other symmetries of the Hamiltonian. We further find that this only works for $\mathcal{Z}_2$-like symmetries.

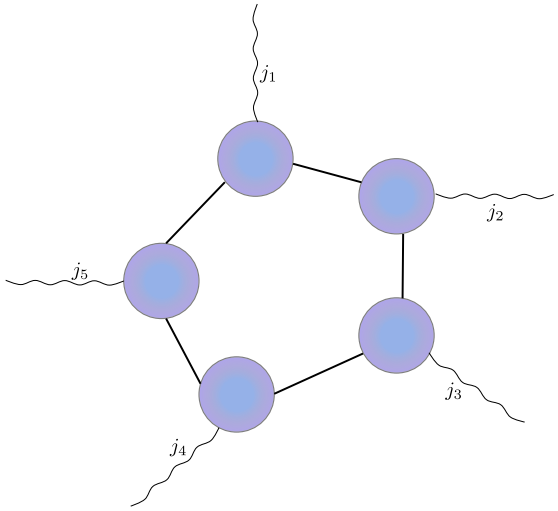

Figure 3.1: Sketch of the discussed model. We have a chain of sites with periodic boundary conditions. Each site is acted upon by a jump-operator j_n. The jump operators on neighbouring sites are related via Eq. 3.141.

We begin by assuming that we are given a Hamiltonian $\mathcal{H}$ which acts on n sites. It has a symmetry $\mathcal{S}$ which commutes with all other symmetries of $\mathcal{H}$, i.e. it lies in the center of the Hamiltonians symmetry group. $\mathcal{S}$ is of order n and generates the cyclic group of order n, $\mathcal{S}^n = \mathbb{1}$. We call j_n the jump-operator that acts on the nth site. Then jump operators on neighbouring sites are related as

$$j_n^\dagger = \mathcal{S} j_{n-1} \mathcal{S}^{-1}, \tag{3.141}$$

see Fig. 3.1 for a sketch of the model. We can then show that 1) if the j_n is non-hermitian the maximally mixed state is only stable for $n = 2$, and 2) for odd orders of the symmetry group only $n = 1$ is possible. Furthermore, in the latter case the jump-operator must necessarily be hermitian. The symmetry $\mathcal{S}$ acts on the mth eigenstate of the Hamiltonian like as well as

$$\begin{aligned} \mathcal{S} \left| E_m \right\rangle &= s_m \left| E_m \right\rangle \\ \mathcal{S}^{n-1} \left| E_m \right\rangle &= (s_m)^{n-1} \left| E_m \right\rangle , \end{aligned}$$

where s_m is the mth eigenvalues of $\mathcal{S}$.

If ρ is diagonal in the eigenbasis of the Hamiltonian it commutes with $\mathcal{H}$, i.e. it is a stationary state. As we have discussed the neighbouring jump-operators are related Eq. 3.141. Similar to the proof found in Ref. [1] we assume to be in the maximally mixed state and check how a perturbation to this state behaves under time evolution. To see that only the maximally-mixed state is stable we make the ansatz $\rho_{a,b}(t) = \delta_{a,b}/D + \Delta_{\rho_{a,b}}(t)$, where D is the dimension of the density matrix. We assume that $\Delta_{\rho_{a,b}}(t=0) = 0$ and ask the question how it evolves in time. We have then

$$\langle E_a|\dot{\rho}|E_b\rangle = \frac{d}{dt}\left(\frac{\delta_{a,b}}{D} + \Delta_{\rho_{a,b}}\right) = \langle E_a|\mathcal{L}[\rho]|E_b\rangle. \tag{3.142}$$

Here $d_t(\delta_{a,b}/D) = 0$ as the derivative of a constant is always 0. With this we have

$$\dot{\Delta}_{\rho_{a,b}} = \langle E_a|\mathcal{L}[\rho]|E_b\rangle = \mathcal{L}[\delta_{a,b}/D] + \mathcal{L}[\Delta_{\rho_{a,b}}] \tag{3.143}$$

$$= -i(E_a - E_b)\rho_{a,b} + \frac{2}{D}\sum_\eta \langle E_a|[j_\eta, j_\eta^\dagger]|E_b\rangle, \tag{3.144}$$

where the first term comes from the unitary part of the Liouvillian $\mathcal{L}_\mathcal{H} = -i[\mathcal{H}, \rho]$. η runs over all jump operators. In the case of $E_a \neq E_b$, the formal solution is, see [1]

$$\Delta_{\rho_{a,b}}(t) \simeq -i\frac{2}{D(E_a - E_b)}\sum_\eta \langle E_a|[j_\eta, j_\eta^\dagger]|E_b\rangle \times \left(-e^{-(E_a - E_b)t}\right). \tag{3.145}$$

This is bounded from above, so in the limit of vanishing dissipation, i.e. $j_\eta \to 0$, $|\Delta_{\rho_{a,b}}| \to 0$. In the case of $E_a = E_b$ we have

$$\dot{\Delta}_{\rho_{a,b}} \propto \sum_\eta \langle E_a|[j_\eta, j_\eta^\dagger]|E_b\rangle. \tag{3.146}$$

We can expand the commutator and insert a resolution of identity, $\mathcal{Z}^{n-1}\mathcal{Z} = \mathcal{I}$:

$$\dot{\Delta}_{\rho_{a,b}} \propto \sum_{\eta=1}^{n} \langle E_a|\,\mathcal{S}^{n-1}\mathcal{S}j_\eta j_\eta^\dagger \mathcal{S}^{n-1}\mathcal{S}\,|E_b\rangle - \langle E_a|\,\mathcal{S}^{n-1}\mathcal{S}j_\eta^\dagger j_\eta \mathcal{S}^{n-1}\mathcal{S}\,|E_b\rangle\,. \tag{3.147}$$

We can reorder this such that neighbouring terms transform into one another:

$$\dot{\Delta}_{\rho_{a,b}} \propto \sum_{\eta=1}^{n} \langle E_a | \mathcal{S}^{n-1} \mathcal{S} j_\eta j_\eta^\dagger \mathcal{S}^{n-1} \mathcal{S} | E_b \rangle - \langle E_a | \mathcal{S}^{n-1} \mathcal{S} j_{\eta+1}^\dagger j_{\eta+1} \mathcal{S}^{n-1} \mathcal{S} | E_b \rangle , \quad (3.148)$$

where we again impose "periodic boundary" conditions on the operator, i.e. $j_{n+1} = j_1$. Transforming the positive term of the right hand side and using the identity in the negative terms yields:

$$\begin{aligned} \dot{\Delta}_{\rho_{a,b}} &\propto \sum_{\eta=1}^{n} ((s_a^*)^{n-1} s_b) \langle E_a | j_\eta j_\eta^\dagger | E_b \rangle - \langle E_a | \mathcal{I} j_{\eta+1}^\dagger j_{\eta+1} \mathbb{1} | E_b \rangle \\ &\propto \sum_{\eta=1}^{n} ((s_a^*)^{n-1} s_b - 1) \langle E_a | j_\eta j_\eta^\dagger | E_b \rangle . \end{aligned}$$

As mentioned before s_a is the ath eigenvalue of $\mathcal{S}$ and hence a root of 1, i.e. $s_a^n = 1$. For the maximally mixed state to be a steady-state, we require this to be zero:

$$0 = \sum_{\eta=1}^{n} ((s_a^*)^{n-1} s_b - 1) \langle E_a | j_\eta j_\eta^\dagger | E_b \rangle , \quad (3.149)$$

For this to vanish as a generic property of the symmetry, we require

$$(s_a^*)^{n-1} s_b = 1. \quad (3.150)$$

Since $\mathcal{S}$ is an element of the center by assumption, we have that the eigenvalues must be identical, i.e. $s_a = s_b$. This is quite easy to via contradiction:

Let $[\mathcal{H}, \mathcal{P}] = [\mathcal{P}, \mathcal{S}] = 0 \; \forall P \in \mathcal{G}(\mathcal{H})$, the symmetry group of $\mathcal{H}$. Let $\mathcal{H}$ be degenerate, i.e. there exists some symmetries which do not commute with each other:

$$\mathcal{H}\phi_0 = E\phi_0$$
$$\mathcal{H}\phi_1 = E\phi_1,$$

then ϕ_0 and ϕ_1 have the same $\mathcal{P}$-eigenvalue.

Proof by contradiction: We have $[\mathcal{H}, \mathcal{X}] = [\mathcal{X}, \mathcal{S}] = 0$ and $\mathcal{X}\phi_0 = x\phi_1$, i.e. $\mathcal{X}$ is one

of the symmetries that we cannot simultaneously diagonalize. We assume that both states have different $\mathcal{S}$-eigenvalues, i.e. $s_0 \neq s_1$.

We want to show either:

- **A)** $[\mathcal{S}, \mathcal{X}] \neq 0$ or
- **B)** $s_0 = s_1$.

Since $[\mathcal{P}, \mathcal{X}] = 0$ by assumption, we have

$$[\mathcal{X}, \mathcal{S}]\phi_0 = (\mathcal{X}\mathcal{S} - \mathcal{S}\mathcal{X})\phi_0 \tag{3.151}$$
$$= \mathcal{X}\mathcal{S}\phi_0 - \mathcal{S}x\phi_1 \tag{3.152}$$
$$= \mathcal{X}s_0\phi_0 - s_1 x\phi_1 \tag{3.153}$$
$$= s_0 x\phi_1 - s_1 x\phi_1 \tag{3.154}$$
$$\neq 0. \tag{3.155}$$

Hence, if the two symmetries commute, then both states must have the same $\mathcal{S}$-eigenvalue.

Furthermore, $\mathcal{S}$ is unitary, i.e. $s_b = s_a = (s_a^*)^*$. Hence we have:

$$(s_a^*)^{n-2} = 1. \tag{3.156}$$

By assumption we have that $\mathcal{S}^n = \mathbb{1}$. The possible eigenstates of the symmetry however have $s_a^{n-2} = 1$. As previously mentioned, the latter are roots of 1. We thus need to find an $(n-2)th$ root, s', that fulfils $(s')^n = 1$.

As a quick reminder, if a number s is a jth root of 1, then it is also an (mj)th root of 1. Let s with $s^j = 1$ be a jth root of 1. Then we have for z^{mj}:

$$s^{mj} = (s^j)^m = s^j \times s^j \times \ldots s^j = 1 \times 1 \times \ldots 1 = 1, \tag{3.157}$$

We now need to find a nth root which is also an $(n-2)$th root or show that such a root does not exist. The latter is much easier. What we need to show is that there is

no $j > 2$ that is both an nth and $(n-2)$th root for even n, i.e. there is no $j > 2$ such that that divides both n and $n-2$. Analogously, there is no $j > 1$ that divides n and $(n-2)$ for odd n. This boils down to showing that the greatest common divisor, *gcd*, of n and $(n-2)$ is 2 for even n.

We can achieve this by using *Euclid's algorithm*. Given two positive integers a and b, with $a > b$, then the common divisors of a and b are the same as $a-b$ and b. *Euclid's algorithm* iteratively replaces the larger of the two numbers by the difference until both sides align:

$$\begin{aligned} \gcd(n, n-2) &= \gcd(n-(n-2), n-2) && (3.158)\\ &= \gcd(2, n-2) && (3.159)\\ &= \gcd(2, n-2-2\cdots-2) && (3.160)\\ &= \gcd(2,2) && (3.161) \end{aligned}$$

In the last equality we used that n was even and subtracting any number of *2s* leaves the result even. Thus the smallest *gcd* of 2 and any other even number must be 2. The statement for odd numbers follows analogously.

We have now shown that in the case of even orders n the only roots s' that fulfil this requirement are of those of second-order, i.e. $s'_a = \pm 1$ for all even symmetries. We have also proven that in the case of odd orders n the only possible root is of first order, i.e. $s'_a = 1$ for all odd symmetries. Thus the only possible symmetries are of order $n = 2$ for even ordered symmetries or $n = 1$ for odd ordered symmetries.

For odd n we necessarily have $n = 1$ and $\mathcal{S} = \mathbb{1}$. Following Eq. 3.141 with only one site this has the consequence

$$j_0^\dagger = j_0. \tag{3.162}$$

Hence, for for odd ordered symmetries the jump operators must be Hermitian. Hermitian jump operators have the consequence that the maximally mixed state is stable at all times, independent of the symmetry or the strength of the dissipation. As above we

will get for the time derivative of some perturbation:

$$\dot{\Delta}_{\rho_{a,b}} \propto \sum_{\eta} \langle E_a | [j_\eta, j_\eta^\dagger] | E_b \rangle. \tag{3.163}$$

This time however the jump-operators are hermitian. We have then:

$$\begin{aligned}
\dot{\Delta}_{\rho_{a,b}} &\propto \sum_{\eta} \langle E_a | [j_\eta, j_\eta^\dagger] | E_b \rangle \\
&= \sum_{\eta} \langle E_a | [j_\eta, j_\eta] | E_b \rangle \\
&= \sum_{\eta} \langle E_a | j_\eta j_\eta - j_\eta j_\eta | E_b \rangle \\
&= 0 \ \forall a, b.
\end{aligned}$$

The maximally-mixed state must thus be a steady-state at all times. As we have seen above, this is in contrast to the case on non-hermitian jump operators. There the maximally mixed state and the normal state of the jump operators lie in two different symmetry sectors and are separated by a phase transition.

In this section we have discussed the conditions under which an OQS can undergo a $\mathcal{PT}$-symmetry breaking phase transition. We found that for such a transition to be possible, the jump-operators on neighbouring sites need to be related by a symmetry of the center of the Hamiltonians symmetry group. In particular, we also saw that is only possible for symmetries of order $n = 2$. This gives us instructions how to construct $\mathcal{PT}$-symmetric systems. We have used this to construct the $\mathcal{PT}$-symmetric LMG dimer which we introduced in the previous sections and which we will further investigate in the next chapter.

3.5 Quantum Trajectories and Monte Carlo Wavefunctions

When analytic results aren't available, i.e. for finite spin sizes, we need to solve the full master equation numerically. In this section we will briefly introduce an import method we use to find the NESS of open quantum systems in Ch. 4 for larger spin sizes.

In this thesis we will often compare results from various methods or different spin sizes with each other. Like this we are able to gauge how well the methods work and how well the quantum physics aligns with our mean-field predictions. For small spin or system sizes we often use *Exact Diagonalization* (ED). ED is a numerical method which diagonalizes a matrix and returns eigenenergies and eigenvectors. In case of non-Hermitian Hamiltonians away from exceptional points it returns complex eigenvalues. The method requires the full system matrix and all its eigenstates to be constructed explicitly, which limits the total system and spin size significantly. By vectorising the density matrix, i.e. $\rho \to |\rho\rangle\rangle$ one can transform an open system problem into a linear algebra problem. This allows one to find target the "lowest-energy" states via well-understood linear algebra based solvers.

An approximative method which targets the states of open quantum systems specifically, was introduced in the nineties by the authors of Ref. [68]. It is known as Quantum Trajectories or the Monte Carlo wavefunction method. The method is based on the insight that the Lindblad master equation of Eq. 2.12 can be rewritten in terms of an effective non-hermitian Hamiltonian

$$H_{\text{eff}} = H - \frac{i}{2}\sum_k \gamma_k A_k^\dagger A_k, \tag{3.164}$$

and a so-called *recycling term*

$$R = \sum_k \gamma_k A_k \rho_s A_k^\dagger. \tag{3.165}$$

Rewritten like this, the master equation reads

$$\frac{d}{dt}\rho_s = -i\left(H_{\text{eff}}\rho - \rho H_{\text{eff}}\right) + R \tag{3.166}$$

The effective non-hermitian Hamiltonian, just like in the previous chapter, describes the coherent dynamics of a system subjected to dissipation. The recycling term on the other hand describes the sudden jumps that occur in the system as the system gets "measured" by the environment. The effective Hamiltonian, due to its non-hermitian

nature, will cause the state to "leak" probability density into the environment, whereas the the recycling term causes the state to collapse into a specific state with unit norm.

When investigating a system, one is often interested in expectation values of operators in a given state. If the system is in a mixed state, as is generically the case in open quantum systems, the expectation values involves both a a quantum mechanical average and an ensemble average:

$$\langle \mathcal{O} \rangle = \mathrm{Tr}[\mathcal{O}\rho] = \sum_n p_n \langle \phi_n | \mathcal{O} | \phi_n \rangle = \sum_n p_n \mathcal{O}_n. \tag{3.167}$$

The latter is a weighted sum pure-state expectation values. The weights of the sum are the classical probability of finding any one state in some ensemble, i.e. if one were to draw a large amount of samples, one would expect them to be distributed according to those weights. This can be used to approximate the last term of Eq. 3.167:

$$\langle \mathcal{O} \rangle \approx \frac{1}{N_s} \sum_s \langle s | \mathcal{O} | s \rangle , \tag{3.168}$$

where the sum runs over the randomly generated sample wave-functions s, and N_s is the total number of samples. In the limit of $N_s \to \infty$, this method becomes exact. A sample is generated by following the stochastic trajectory of some initial state $|\phi(t=0)\rangle$. This state is time-evolved according to the following algorithm, see Ref. [27] for an in-depth review of the method and its application.

We begin with calculating the time-step according to the effective Hamiltonian to first order in δ_t:

$$|\phi(t_0 + \delta_t)\rangle = (1 - iH_{\mathrm{eff}}\delta_t) |\phi(t_0)\rangle . \tag{3.169}$$

The norm of this state is then given by:

$$\langle\phi(t_0)\,|\phi(t_0+\delta_t)\rangle = \langle\phi(t_0+\delta_t)|\,(1+iH_{\text{eff}}^{\dagger}\delta_t)(1-iH_{\text{eff}}\delta_t)\,|\phi(t_0)\rangle \tag{3.170}$$

$$= 1-\delta_t\langle\phi(t_0)|i(H_{\text{eff}}-H_{\text{eff}}^{\dagger})\,|\phi(t_0)\rangle + \mathcal{O}(\delta_t^2) \tag{3.171}$$

$$= 1-\delta_t\sum_k \gamma_k\langle\phi(t_0)|A_k^{\dagger}A_k\,|\phi(t_0)\rangle + \mathcal{O}(\delta_t^2) \tag{3.172}$$

$$\approx 1-\sum_k \delta p_k, \tag{3.173}$$

where $\delta p = \sum_k \delta p_k$ quantifies the amount of norm that dissipates into the environment due to each dissipation channel. One can interpret $1-\delta p$ as the probability that a evolves coherently and δp that a "measurement" occurs. The author of Ref. [27] shows that, under this interpretation one recovers the full master equation.

As a next step, one evolves the state $|\phi(t_0\rangle$ either

1. according to
$$|\phi(t_0+\delta_t)\rangle = \frac{(1-iH_{\text{eff}}\delta_t)}{\sqrt{1-\delta p}}\,|\phi(t_0)\rangle\,, \tag{3.174}$$
with a probability of $1-\delta p$, or

2. according to
$$|\phi(t_0+\delta_t)\rangle = \frac{A_k\,|\phi(t_0)\rangle}{\sqrt{1-\delta p,}} \tag{3.175}$$
with probability δp_k, where a specific A_k is chosen randomly with probability $\delta p_k/\delta p$.

This process will produce a jagged looking trajectory full of random jumps. If we repeat it many times and average over all trajectories, we will eventually arrive at the "true" trajectory, the full quantum system would take towards the steady-state, see Fig. 3.2. In the figure we evolved 100 trajectories using the dissipative LMG model of Eq. 3.5. We show two example trajectories (solid lines) as well as the average over all trajectories (dashed line). As this procedure only cares about an effective Hamiltonian and wave functions, it scales much better than the full open system dynamics. The trade-off is the requirement to keep track of many trajectories and repeating a costly Monte-Carlo step many times.

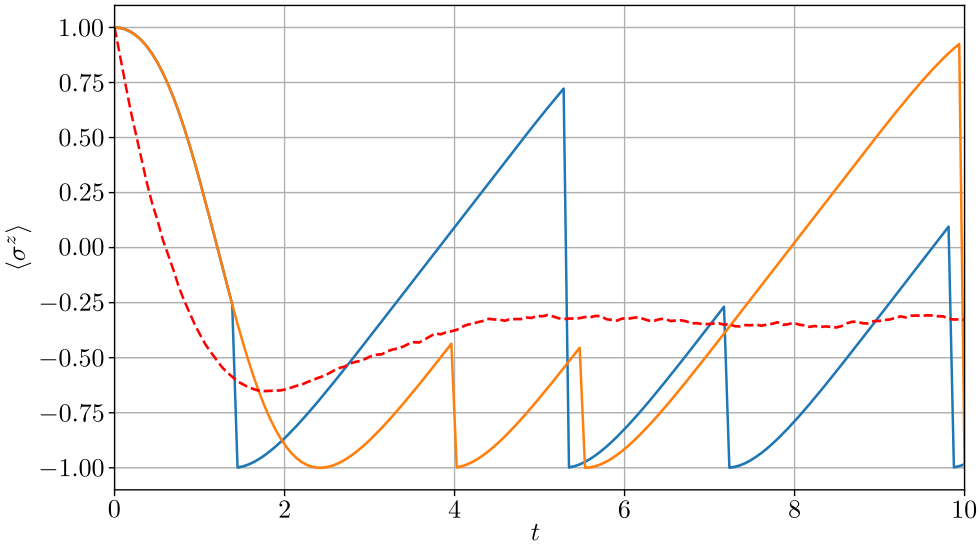

Figure 3.2: The plot shows 2 individual trajectories (solid lines) as well the average over 1000 trajectories (dashed line). The system under consideration is a simple dissipative spin $\mathcal{H} = \sigma^x$ with $\gamma = 1$. One can see clearly distinguished the coherent Rabi oscillations from the incoherent and irregular quantum jumps.

In this chapter we have discussed the Hosltein-Primakoff approximation as well as the mean-field approximation of the $\mathcal{PT}$- and LMG-models. We derived analytic expressions for the S^z-component and the purity P of the $\mathcal{PT}$-model as well as mean-field equations of motion for each model. We concluded the chapter with an introduction quantum trajectories. In the next chapter we will use these methods to compute a linear stability phase diagram of the $\mathcal{PT}$-symmetric LMG dimer model and try to understand its phases and transitions. This phase diagram will contain the number of linearly stable solutions as a function of the system parameters.

Chapter 4

Results

4.1 Introduction

In the previous two chapters we have discussed the theoretical context of our work as well as the methods we employed. In this chapter we will now discuss our findings. As we have mentioned in the first chapter our goal is to investigate the competition between phenomena exclusive to open quantum systems and phenomena which have an analogue in equilibrium systems. To this end we choose two well understood models and investigate how they interact with each other, namely the LMG model, see Eq. 4.1 as well as the $\mathcal{PT}$-dimer model, see Eq. 3.1. The former was chosen for its second-order groundstate phase transition, which survives into the dissipative case. The $\mathcal{PT}$-model on the other hand possesses a phase transition which is fully disconnected from any equilibrium type phase transition. As we will see later, both have a magnetically ordered steady-state and branch out into different phases along different axes of the phase diagram. While the LMG model transitions into a symmetry-broken phase of two valid steady-state, the $\mathcal{PT}$-model will transition into the maximally mixed state. A sketch of the model can be seen in Fig. 4.1.

This chapter will begin by a discussion of the individual models in Secs. 4.2 and 4.3 and then move on to the discussion of the full model in Sec. 4.4. This section begins with a discussion of the phase diagram of linearly stable states as well as a discussion of mean-field trajectories which exemplify the general behaviour of the mean-field equations in

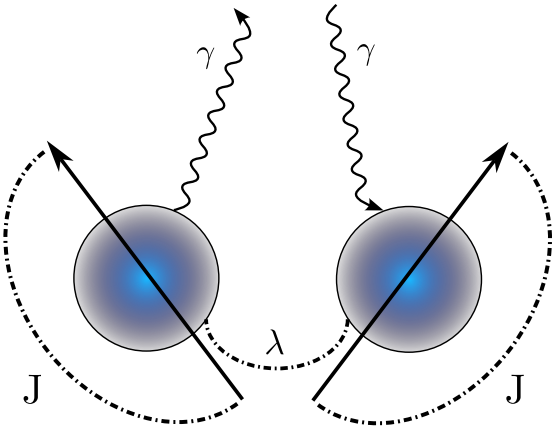

Figure 4.1: The plot shows a sketch of the full model. There are two collective spins connected by a the spin flip interaction of the $\mathcal{PT}$-model whose strength is given by λ/g. Each spin experiences an LMG-non-linearity of strength J/g. The spins are further subject to a field perpendicular to the self-interaction. The field strength $g = 1$ has been chosen as our unit of energy. Both spins are open with a coupling strength of γ/g. One is driven, while the other is dissipative.

those phases. We move on to a comparison of mean-field results and results from exact diagonalization. Again, example trajectories are given for some points along the parameter scans. We end the section by comparing the mean-field trajectories to spin-Wigner calculations in some phases. Overall we find that there is indeed a competition between the second-order phase transitions of the regular LMG model and the $\mathcal{PT}$-symmetry breaking phase transition. This competition leads to a strong deformation of the phase boundaries and creates an incredibly rich phase diagram.

4.2 LMG Model

4.2.1 Hamiltonian, Liouvillian and Mean-field Equations recap

The first part of our $\mathcal{PT}$-symmetric LMG dimer is the LMG model itself. As we have seen Ch. 2 it is a transverse field Ising model with all-to-all coupling in the limit of very large spins. Its Hamiltonian is given by

$$\mathcal{H}_{\mathrm{LMG}} = \frac{J}{s} S_x^2 - g S_z. \tag{4.1}$$

Here g is the strength of the transverse field and will be used as our unit of energy, i.e. $g = 1$ from now on. J/g is the strength of the self-interaction. S_i are spin operators of a spin of size s.

In Ch. 2 we saw the phase transitions of the *LMG* model as a scan over the field strength for (anti-)ferromagnetic self-interaction. When constructing the full model Eq. 4.35, we ran into the issue that in the limit of vanishing field, we would not recover the simple $\mathcal{PT}$-model, as the self-interaction added more than a simple offset. Hence, we fix the field strength as the unit of energy and scan over J/g. For completeness sake we show the ground-state scan below, see Fig. 4.2.

A simple ground-state mean-field calculation in a similar vein as we have done in the previous chapter yields the critical value J_c/g:

$$E = \langle \mathcal{H}_{\mathrm{LMG}} \rangle = -\frac{J}{s}\langle S_x^2 \rangle - \langle S_z \rangle \tag{4.2}$$

At this point we use the mean-field approximation $\langle AB \rangle \approx \langle A \rangle \langle B \rangle$ and break up the correlation:

$$\epsilon \equiv \frac{E}{s} = -\frac{J}{s^2}\langle S_x \rangle^2 - \frac{1}{s}\langle S_z \rangle. \tag{4.3}$$

We now absorb the spin size into the expectation values and define $X := \langle S_x \rangle / s$. To represent a physical state we now require that all expectation values are real and lie between ± 1:

$$\epsilon = -JX^2 - Z. \tag{4.4}$$

Finally, we use the total spin conservation $X^2 + Z^2 = 1$ to get rid of the X-dependence. Note that since Y does not appear in the model, its expectation will always be zero and we can neglect it here:

$$\epsilon = -J(1 - Z^2) - Z. \tag{4.5}$$

Now that we have a simple expression for the energy, we can find the state which

minimizes it by taking the derivative:

$$\frac{d\epsilon}{dZ} = 2JZ - 1 = 0 \tag{4.6}$$

$$\Rightarrow Z = \frac{1}{2J} \tag{4.7}$$

$$\Rightarrow X = \pm\sqrt{1 - \frac{1}{4J^2}} \tag{4.8}$$

This becomes imaginary if $1 < \frac{1}{4J^2}$. Hence mean-field predicts a phase transition at

$$\frac{J_c}{g} = \pm\frac{1}{2} \tag{4.9}$$

We can see in Fig. 4.2 that the mean-field prediction of the phase transition is in excellent agreement with the results we obtained from exact diagonalization for various spin sizes. We can clearly see that the kink at the mean-field approximation of the critical value, $J_c/g = 1/2$, gets more and more pronounced as $S \to \infty$. The insets show the energy E as well as the energy gap δE at each point. The energy gap closes at the critical point and remains closed after the transition. This confirms that this transition is indeed a second-order phase transition.

Note, that the equilibrium model discussed here and depicted in Fig. 4.2 has its spin fully up in the ordered phase. This is in contrast to the dissipative model we discuss in the next section, where the ordered steady-state will be the down state. However, the phase transition of this particular equilibrium model will reappear in the full model, where it connects to the phase transition of the driven spin.

4.2.2 Steady state

In the last section we derived a mean-field approximation of the critical self-interaction strength J_c/g for the equilibrium LMG model. We further compared the results for various spin sizes and found a second-order phase transition at the predicted value.

Let us now see how adding dissipation changes the qualitative and quantitative behaviour of the model. In Ch. 3 we have already introduced the dissipative LMG Eq. 3.5. As a reminder, it is an open LMG whose jump-operator is given by a collective

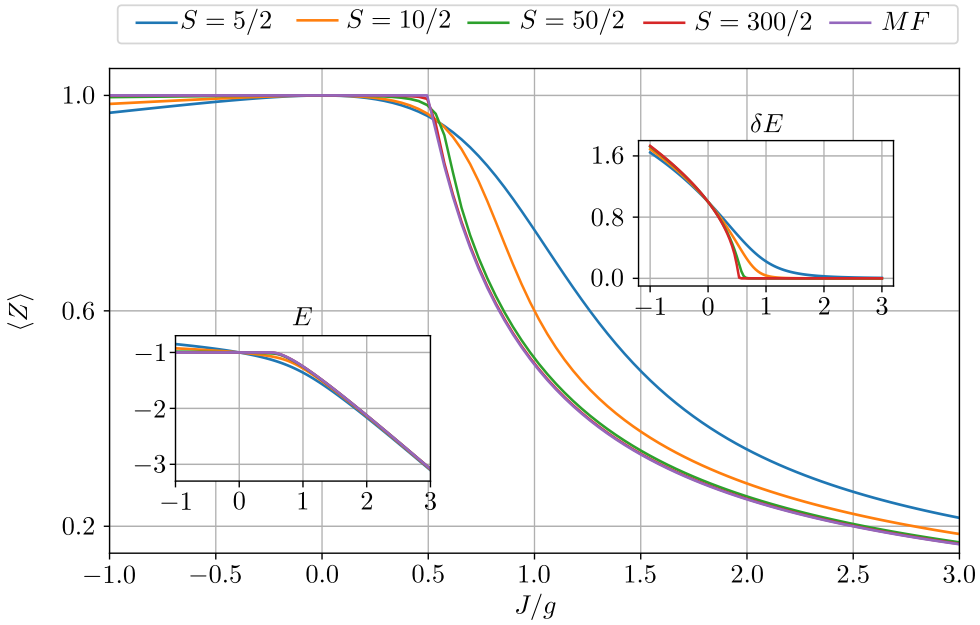

Figure 4.2: A scan over J/g of the equilibrium LMG model Eq. 4.1 of the Z-expectation values. The insets show the energy gap δE as well as the total energy of the ground state E. The closed gap over a large area shows that this is indeed a second-order phase transition.

spin-lowering operator, S^-. With this the Lindblad master equation looks like

$$\mathcal{L}[\rho] = -i\,[\mathcal{H}_{\mathrm{LMG}}, \rho] + \frac{\gamma}{S}\mathcal{D}[S^-][\rho] \tag{4.10}$$

$$\mathcal{D}[S^-][\rho] = S^-\rho S^+ - \frac{1}{2}\{S^+S^-, \rho\}. \tag{4.11}$$

In the previous chapter we have derived the following set of mean-field equations for the spin-components from this master equation

$$\dot{X} = Y + \gamma XZ \tag{4.12}$$

$$\dot{Y} = -X + 2JZX + \gamma YZ \tag{4.13}$$

$$\dot{Z} = -2JYX - \gamma(1 - Z^2) \tag{4.14}$$

If we set them to zero and solve for X, Y, Z, we get the spin components of the steady state. It is easy to see that a state which solves these equations for every set of parameters is $X = Y = 0, Z = \pm 1$. The general solution in the symmetry-broken

phase is

$$X = \pm\sqrt{\frac{\gamma^2 - g\Xi}{2J\Xi}} \tag{4.15}$$

$$Y = -\frac{X\Xi}{\gamma} \tag{4.16}$$

$$Z = \frac{g\Xi}{\gamma^2} \tag{4.17}$$

with $\Xi = J + \sqrt{J^2 - \gamma^2}$. To derive this one has to divide by X, hence this solution cannot be applied to the *normal* phase, where $X = 0$. The *normal* state refers to the state $X = Y = 0, Z = \pm 1$ and is denoted by $\nu_\pm$. We can use this knowledge to make a linear stability analysis and find the critical value at which this solution becomes unstable, see the discussion of linear stability in Ch. 3. As a brief reminder of linear stability analysis, the solution to a set of coupled, non-linear equations is said to be unstable, if at least one eigenvalue of the associated Jacobian is positive. The Jacobian of this set of equations is given by:

$$\mathcal{J}(X,Y,Z) = \begin{pmatrix} Z\gamma & 1 & X\gamma \\ -1 + 2JZ & Z\gamma & 2JX + Y\gamma \\ -2JY - 2\gamma X & -2JX - 2\gamma Y & 0 \end{pmatrix}. \tag{4.18}$$

Plugging in the normal state yields an effective 2×2 matrix.

$$\mathcal{J}(\nu_-) = \begin{pmatrix} -\gamma & 1 & 0 \\ -1 - 2J & -\gamma & 0 \\ 0 & 0 & 0 \end{pmatrix}. \tag{4.19}$$

The eigenvalues of this matrix are given by:

$$\lambda_0 = 0 \tag{4.20}$$

$$\lambda_\pm = -\gamma \pm \sqrt{-1 - 2J}. \tag{4.21}$$

Setting this to zero and solving for J yields the γ-dependent J_c at which the eigenvalues change sign. First note that $\lambda_- < \lambda_+$, so it suffices to check when $\lambda_+ = 0$. Solving this

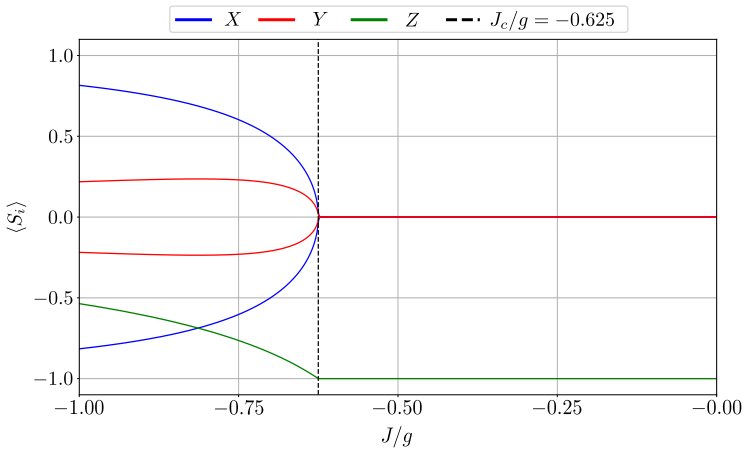

Figure 4.3: This figure shows the solutions of the mean-field equations Eq. 4.12. As was predicted by the linear stability analysis, for $\gamma/g = 0.5$ we see a symmetry breaking phase transition at $J_c/g = -0.625$. Before that the only stable state is the normal state, aligned with the jump-operator.

then yields:

$$J_c = \frac{-(\gamma^2 + 1)}{2}. \tag{4.22}$$

Note here, that if we were to plug in ν_+, we would get for the eigenvalues

$$\lambda'_\pm = \gamma \pm \sqrt{2J - 1}. \tag{4.23}$$

One can see, that the real part of $\lambda_+ \geq 0 \forall J$. Hence, while this state is technically a solution, it is an unstable one.

In all our calculations we use $\gamma/g = 0.5$, hence the mean-field approximation for the critical interaction strength is given by $J_c/g = -0.625$. Fig. 4.3 shows the solutions to the mean-field equations over a range of interaction strengths. The different solutions for X and Y were obtained by time-evolving various different initial conditions. As expected, the normal state goes unstable exactly as the linear stability analysis predicted. Beyond the phase transition we can see two stable solutions emerge, which are degenerate in X and described by the equations 4.15. Fig. 4.4 on the other hand shows a comparison of the mean-field solution of the Z-component with results obtained from exact diagonalization for various spin sizes. One can clearly see that the results from

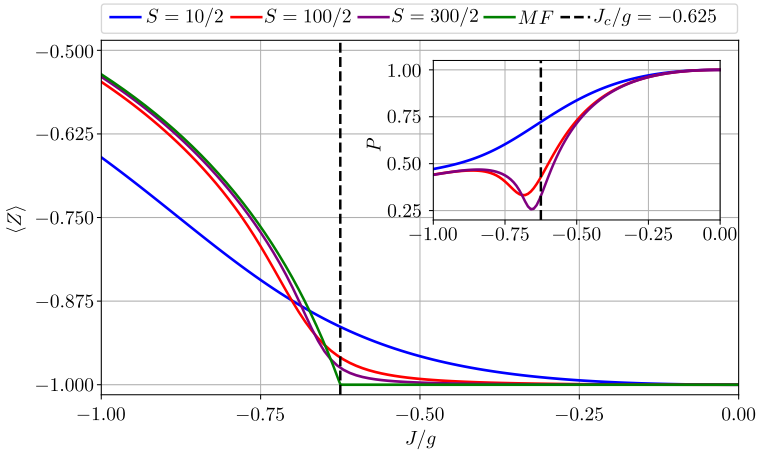

Figure 4.4: Similar to Fig. 4.2 this figure shows a comparison of the mean-field solution for the Z-component with solutions from exact diagonalization. We can see again a good convergence of the full-quantum results towards the mean-field predictions as the spin size increases. The inset shows the purity of the state. We can see a pronounced dip which converges towards the point of the phase transition.

exact diagonalization converge towards the mean-field solution as $S \to \infty$. As in the equilibrium model, this confirms that the mean-field solutions are indeed exact in the thermodynamic limit. This is a second-order phase transition which breaks the $\mathbb{Z}_2$ symmetry of the model. The symmetry-broken states are the solutions $X_\pm$ of Eq. 4.15. Both solutions contribute equally to the expectation value, which causes them to vanish. This is why we have omitted them in the plot. The phase transition we see here is the dissipative analogue of that of the equilibrium model shown in Fig. 4.2. There the ground-state was degenerate in the X-component as well, which leads to a vanishing expectation value. We can see that the dissipative phase transition connects directly to the equilibrium phase transition, when we take the limit $\gamma \to 0$ in Eq. 4.22. In the limit of vanishing dissipation, we recover the critical J_c of the equilibrium model. Note, that in the case of the dissipation, we recover the phase transition of an equilibrium model with negative Field strength $g = -1$.

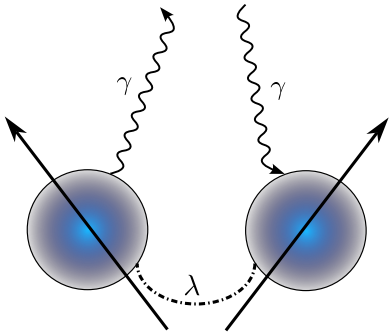

Figure 4.5: The plot shows a sketch of the $\mathcal{PT}$-model. There are two collective spins connected by a the spin flip whose strength is given by λ/g. Both spins are open with a coupling strength of γ/g. One is driven, while the other is dissipative.

4.3 $\mathcal{PT}$-Model

The second part of the LMG-dimer is the $\mathcal{PT}$-model of Eq. 3.1, see Fig. 4.5 for a sketch. In the context of $\mathcal{PT}$-symmetry breaking phase transitions it has been thoroughly discussed by Huber et al. in Ref. [1]. As a brief reminder, the model is described by the following master equation:

$$\mathcal{L}[\rho] = -i\left[\mathcal{H}_{\mathrm{PT}}, \rho\right] + \frac{\gamma}{S}\left(\mathcal{D}[S_a^-][\rho] + \mathcal{D}[S_b^+][\rho]\right) \tag{4.24}$$

$$\mathcal{H}_{\mathrm{PT}} = \frac{\lambda}{2S}\left(S_a^+ S_b^- + S_b^- S_a^+\right) \tag{4.25}$$

$$\mathcal{D}[S_a^-][\rho] = S_a^- \rho S_a^+ - \frac{1}{2}\{S_a^+ S_a^-, \rho\} \tag{4.26}$$

$$\mathcal{D}[S_b^+][\rho] = S_b^+ \rho S_b^- - \frac{1}{2}\{S_b^- S_b^+, \rho\}. \tag{4.27}$$

Here, λ/g is the interaction strength between the two spin and $\gamma/g = 0.5$ as in the previous model. The model has been chosen such that the $\mathcal{PT}$-symmetry breaking phase transition occurs at $\lambda_c = \gamma$. This Lindblad master equation allows for two analytic treatments, mean-field as well as Holstein-Primakoff, see Ch. 3 for the full derivation. We use the mean-field equations to predict a phase diagram.

We use the Holstein-Primakoff transformation to rewrite the spin model as one of two coupled bosonic modes. This allows us to derive analytic expressions for the purity as well as the magnetization. This gives us a good way of ensuring the correctness of

our derivations. As we have seen in Ch. 3 the mean-field equations are

$$\dot{X}_a = \lambda Z_a Y_b + \gamma X_a Z_a \tag{4.28}$$

$$\dot{Y}_a = -\lambda Z_a X_b + \gamma Y_a Z_a \tag{4.29}$$

$$\dot{Z}_a = \lambda(X_a Y_b - Y_a X_b) - \gamma(1 - Z_a^2) \tag{4.30}$$

$$\dot{X}_b = \lambda Z_b Y_a - \gamma X_b Z_b \tag{4.31}$$

$$\dot{Y}_b = \lambda Z_b X_a - \gamma Y_b Z_b \tag{4.32}$$

$$\dot{Z}_b = \lambda(X_a Y_b - Y_a X_b) + \gamma(1 - Z_b^2), \tag{4.33}$$

where X_a is the X-component on site a. Setting these equations to zero and solving for the spin components yields their steady-state values. These can be seen in Fig. 4.6. The main part of the figure shows the Z-component of the solutions for both sites and compares them to the results from exact diagonalization and quantum trajectories for various spin sizes. As the *LMG* model, the $\mathcal{PT}$-model also a possess a normal state, $X_a = 0, Y_a = 0, Z_a = -1, X_b = 0, Y_b = 0, Z_b = \pm 1$. This state is stable for $\lambda/g < 0.5$. At the point of the phase transition, this state transitions into the maximally mixed state. As before, we can see a good convergence towards the mean-field prediction for increasing spin sizes. The inset shows the Holstein-Primakoff approximation for the purity of the state, which we re-derived in **theory** and which was first published in [15]:

$$P = 1 - \frac{\lambda^2}{\gamma^2}. \tag{4.34}$$

One can see that the Holstein-Primakoff prediction of the purity aligns with the discussion of the stability of the maximally-mixed state found in Ch. 3. Take note, that this is not well defined in the limit $\gamma \to 0$ and does not connect to any equilibrium phase transition like the LMG model. This is a further indicator that this is a purely non-equilibrium phenomenon. At the point of the $\mathcal{PT}$-symmetry breaking phase transition, the steady-state gains a $\mathcal{P}$-symmetry, which neither the normal state nor the model possess.

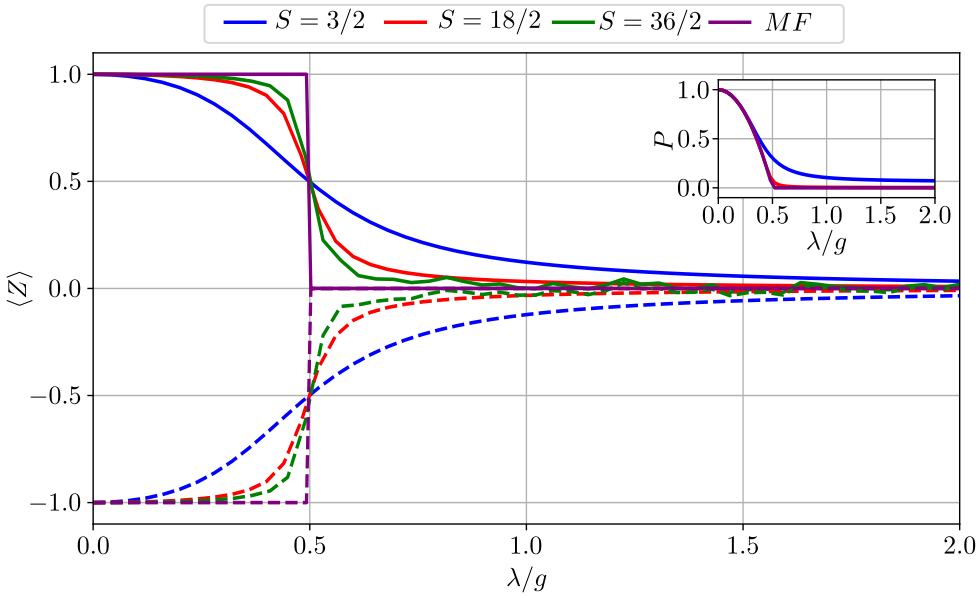

Figure 4.6: This figure compares the Z-expectation values for the dissipative site a (dashed) and the pumped site b (solid) for various spin sizes with the solutions to the mean-field equations (purple). As with the LMG-model, we see a convergence of the results towards the mean-field solutions for increasing spin-sizes. The inset shows the the purity of the steady-states as well as the purity from Holstein-Primakoff (purple).

4.4 LMG-Dimer model

In the last two sections we have seen how the individual models behave as we scan them across their relevant parameter and drive them across their respective phase transitions. We saw that the LMG model possesses a continuous phase transition along it self-interaction strength, while the $\mathcal{PT}$-model has a $\mathcal{PT}$-symmetry breaking phase transition as a function of the interaction strength. In this section we will now introduce the full model and see how those two phenomena influence each other.

4.4.1 Mean-field Equations

As before, the starting point of our investigations is the full quantum model:

$$\mathcal{L}[\rho] = -i\,[\mathcal{H}, \rho] + \frac{\gamma}{S}\left(\mathcal{D}[S_a^-][\rho] + \mathcal{D}[S_b^+][\rho]\right) \tag{4.35}$$

$$\mathcal{H} = \mathcal{H}_{\mathrm{LMG,a}} \otimes \mathbb{1} + \mathbb{1} \otimes \mathcal{H}_{\mathrm{LMG,b}} + \mathcal{H}_{\mathrm{PT}} \tag{4.36}$$

$$\mathcal{D}[S_a^-][\rho] = S_a^- \rho S_a^+ - \frac{1}{2}\{S_a^+ S_a^-, \rho\} \tag{4.37}$$

$$\mathcal{D}[S_b^+][\rho] = S_b^+ \rho S_b^- - \frac{1}{2}\{S_b^- S_b^+, \rho\}, \tag{4.38}$$

where $\mathcal{H}_{\mathrm{LMG,a}}$ and $\mathcal{H}_{\mathrm{LMG,b}}$ refer to the LMG-models of site a and b respectively. While conceptually we coupled two different LMG models via a $\mathcal{PT}$-symmetric model with carefully balanced gain and loss, the total Hamiltonian is just a sum of the individual Hamiltonians. Therefore, the total mean-field equations are just the sum

of the individual models on the respective sites:

$$\dot{X}_a = gY_a + \lambda Z_a Y_b + \gamma X_a Z_a \tag{4.39}$$

$$\dot{Y}_a = -gX_a + 2JZ_a X_a - \lambda Z_a X_b + \gamma Y_a Z_a \tag{4.40}$$

$$\dot{Z}_a = -2JY_a X_a - \lambda(X_a Y_b - Y_a X_b) - \gamma(1 - Z_a^2) \tag{4.41}$$

$$\dot{X}_b = gY_b + \lambda Z_b Y_a - \gamma X_b Z_b \tag{4.42}$$

$$\dot{Y}_b = -gX_b + 2JZ_b X_b - \lambda Z_b X_a - \gamma Y_b Z_b \tag{4.43}$$

$$\dot{Z}_b = -2JY_b X_b + \lambda(X_a Y_b - Y_a X_b) + \gamma(1 - Z_b^2) \tag{4.44}$$

$$\tag{4.45}$$

These equations are notably not symmetric under $J \to -J$, which explains the asymmetry we will find in the phase diagram along that axis. We further have a symmetry $X \to -X$, $Y \to -Y$ and $Z \to Z$. This is just a reflection of the $\mathbb{Z}_2$-symmetry of the original system. Notably, we can also find the symmetry $a \to b$ with $\gamma \to -\gamma$. Now a negative dissipation makes little sense on the level of the master equation. However, as we have seen in the derivation of the equations in Ch. 3, the sign of γ in the mean-field equations follows from the type of coupling present in the master equation. This means that γS^+ leads to $-\gamma$ while γS^- leads to $+\gamma$ in the X and Y equations and vice versa in the Z equations. Hence this symmetry is the mean-field analogue of the $\mathcal{PT}$-symmetry of the master equation.

These equations still have a stable normal state, i.e. $\nu = |\downarrow,\uparrow\rangle\langle\downarrow,\uparrow|$ for small λ/g and small $|J/g|$. In the limit of zero coupling, $\lambda/g = 0$, we recover two independent LMG models, one of which is dissipative and one of which is driven. The driven LMG model connects to the equilibrium LMG model we saw earlier and has its phase transition at $J_c/g = +0.625$ for $\gamma/g = 0.5$. The dissipative LMG model is the one we saw earlier as well. It becomes critical at $J_c/g = -0.625$. In the limit of $J/g = 0$ we recover the $\mathcal{PT}$-model from the previous section.

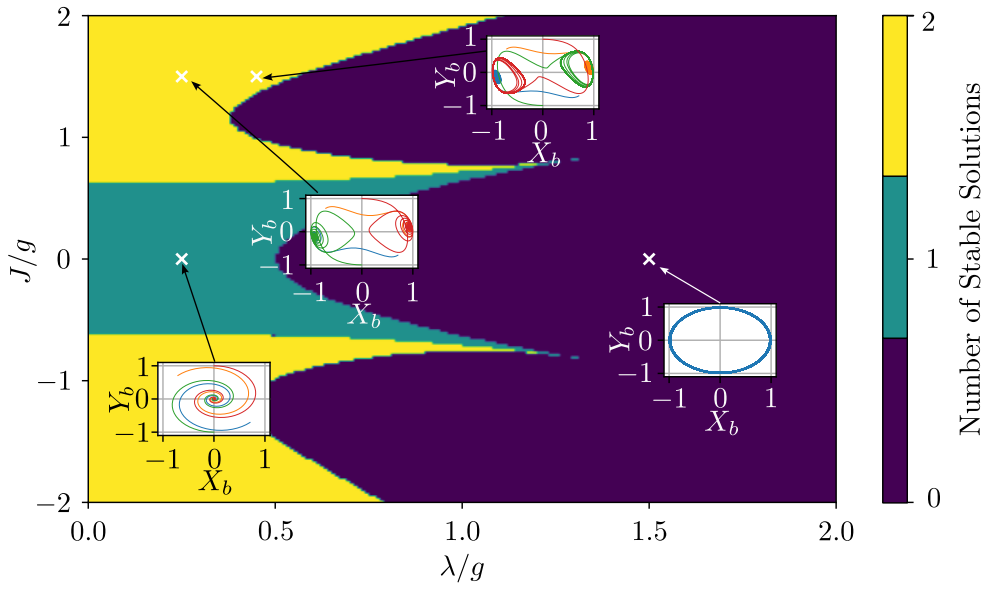

Figure 4.7: This figure shows a scan over the parameter ranges J/g and λ/g respectively at $\gamma/g = 0.5$. One can see three distinct linearly stable phase: The normal phase (turquoise), the LMG phases (yellow), and the $\mathcal{PT}$-phase (purple). The insets show typical mean field trajectories in the $X_b - Y_b$-plane in each of theses phases. At $\lambda = 0.25, J = 0$ we are deep in the normal phase and all initial conditions quickly evolve towards the $X_b = Y_b = 0$. At $\lambda = 0.25, J = 1.5$ we are deep in the LMG phase and the initial conditions spiral towards either of two fixed points, see Fig. 4.1 for more detail. At $\lambda = 0.45, J = 1.5$ two of the initial conditions evolve into stable limit cycles after some time, while the remaining two initial conditions spiral towards the known LMG-fixed points. The final inset at $\lambda = 1.5, J = 0$ shows a single limit cycle. This is the phase that [1] identify as the maximally mixed, or PT phase and [2] as *boundary time crystals*.

4.4.2 Linear Stability Phase Diagram

The first step of our investigation into the full system began by developing the linear stability phase diagram over a wide parameter range. The linear phase diagram was found using brute force integration of many initial conditions and using linear stability analysis to test how many *different* solutions are stable. The Jacobian for the system of equations in Eq. 4.39 is given by

$$J = \begin{pmatrix} Z_a\gamma & 1 & Y_b\lambda + X\gamma & 0 & Z_a\lambda & 0 \\ -1 + 2JZ_a & Z_a\gamma & 2JX_a - X_b\lambda + Y_a\gamma & -Z_a\lambda & 0 & 0 \\ -2JY_a - Y_b\lambda & -2JX_a + X_b\lambda & 2Z_a\gamma & Y_a\lambda & -X_a\lambda & 0 \\ 0 & Z_b\lambda & 0 & -Z_b\gamma & 1 & Y_a\lambda - X_b\gamma \\ -Z_b\lambda & 0 & 0 & -1 + 2JZ_b & -Z_b\gamma & 2JX_b - X_a\lambda + Y_b\gamma \\ Y_b\lambda & -X_b\lambda & 0 & -2JY_b - Y_a\lambda & -2JX_b + X_a\lambda & -2Z_b\gamma \end{pmatrix}. \tag{4.46}$$

The reasoning is that once the number of stable solution changes the dynamical system underwent a bifurcation, which translates to a phase transition of the full quantum system. This method, while crude, gave us an excellent first idea of how the phase diagram looks and what kind of phase we could expect. The diagram, we developed in this fashion can be seen in Fig. 4.7. At each of the 200×200 points we used 64 initial conditions and counted the number of linearly stable solutions we could find. This method allows us to identify 3 distinct linearly stable phases: The normal phase (turquoise), the LMG phases (yellow), and the $\mathcal{PT}$-phase (purple). In the normal phase we find just a single stable state, which coincides with the normal state of the individual models, i.e. $Z_a = -1,\ Z_b = 1$. The LMG phases, upon closer inspection reveal that they are two distinct phases, each with their own set of two stable states, see Fig. 4.3 for reference. As we have discussed previously, the dissipative LMG model of site (a) will undergo a phase transition at negative J/g, while the driven one of site (b) will undergo a phase transition at negative J/g. This is similar to what we saw in Fig. 4.4, excepting that the precise values for X and Y are influenced by λ. While for $\lambda/g = 0$ one site will always remain in the normal state, at finite λ/g, a small perturbation will drive the usually non-critical site out of the normal state as well. Lastly, we find that in a large part of the phase diagram not a single solution is stable. A first explanation can be derived from the phase diagram of the $\mathcal{PT}$-model Fig. 4.6. Beyond the phase

transition, all expectation values and the purity are zero. That means, the state is in the maximally mixed state. The mean-field equations were derived under the condition that $X^2 + Y^2 + Z^2 = S^2$, hence that spin is conserved. This cannot be fulfilled by the maximally mixed state, hence no stable solution exists. Note that this is an artefact of the mean-field approximation that the spin-correlations factorise. In the full quantum model we still have full spin conservation as we have $\langle S_x^2 \rangle + \langle S_y^2 \rangle + \langle S_z^2 \rangle = S^2$.

The second important feature of the phase diagram are the lobes and the bending of the LMG phase boundary. These features are the most striking consequences of the competition between the $\mathcal{PT}$-symmetry breaking phase transition and the second-order phase transition of the LMG-model. From the previous discussions it is clear that the central lobe must correspond to the phase transition we have seen in Fig.4.6. It is stretched and lobe-like shape which remains to be understood. To this end we will make use of linear stability analysis once more. As we have discussed in Ch. 3, a state can only be a stable solution if all eigenvalues of the Jacobian are negative. We know, that at any point in the turquoise region of Fig. 4.7 the normal state is stable. A straightforward path to understanding the shape of the phase boundaries is thus to investigate the eigenvalues of the Jacobian of the normal state. The Jacobian of the normal state looks like

$$J(\nu) = \begin{pmatrix} -\gamma & 1 & 0 & 0 & -\lambda & 0 \\ -1-2J & -\gamma & 0 & \lambda & 0 & 0 \\ 0 & 0 & -2\gamma & 0 & 0 & 0 \\ 0 & \lambda & 0 & -\gamma & 1 & 0 \\ -\lambda & 0 & 0 & -1+2J & -\gamma & 0 \\ 0 & 0 & 0 & -0 & 0 & -2\gamma \end{pmatrix}. \tag{4.47}$$

Looking a bit closer one can see that the 3rd row and column as well as the 6th row and column have zeros in all but one place. Hence the first two eigenvalues are known and the problem reduces to an effective 4x4 matrix. The eigenvalues of this problem

can then be found more readily. The full set is:

$$\epsilon_{1,2} = -2\gamma \tag{4.48}$$

$$\epsilon_3 = -\gamma - \sqrt{-2\sqrt{J^2\lambda^2 + J^2 - \lambda^2} + \lambda^2 - 1} \tag{4.49}$$

$$\epsilon_4 = -\gamma + \sqrt{-2\sqrt{J^2\lambda^2 + J^2 - \lambda^2} + \lambda^2 - 1} \tag{4.50}$$

$$\epsilon_5 = -\gamma - \sqrt{2\sqrt{J^2\lambda^2 + J^2 - \lambda^2} + \lambda^2 - 1} \tag{4.51}$$

$$\epsilon_6 = -\gamma + \sqrt{2\sqrt{J^2\lambda^2 + J^2 - \lambda^2} + \lambda^2 - 1} \tag{4.52}$$

The first step of understanding the center lobe and LMG phase boundary is to find the eigenvalues which change sign. A simple, brute force parameter scan reveals that only ϵ_4 and ϵ_6 can become unstable. We have plotted both eigenvalues in Fig. 4.8, where the eigenvalues ϵ_4 (a) and ϵ_6 (b) have been scanned across the parameter range. To highlight the thresholds the value range has been artificially restricted to $\epsilon = \pm 0.1$. Now that we know which eigenvalues are responsible to destabilize the normal state, we can try to get analytic expressions for the critical $J_c(\lambda)$ and the critical $\lambda(J)$. ϵ_6 can be readily solved for J_c without any further tricks. This yields the following expression:

$$|J_c| = \sqrt{\frac{(\gamma^2 - \lambda^2 + 1)^2 + 4\lambda^2}{4\lambda^2 + 4}}. \tag{4.53}$$

A Taylor series expansion around $\lambda/g = 0$ yields

$$J_c/g = \pm 0.625 \pm \frac{1}{80}\lambda^2 + \mathcal{O}(\lambda^4), \tag{4.54}$$

i.e quadratic corrections to the critical self-interaction strength $J_c \propto \lambda^2$ in λ. In Fig. 4.8 this is shown by the green lines. This explains the shape of the LMG phase transition.

Reaching an expression for the critical $\lambda_c(J)$ is a bit more involved as it requires solving the real part of $\epsilon_4 = 0$ for λ/g. The issue here is the minus sign under the first square root, which is not present in ϵ_6. To get around this issue, one can perform a Taylor series expansion of $\epsilon_4 = 0$ around $J/g = 0$. This will yield an approximate, complex expression for ϵ_4. We can then take the real part of this expression and set it

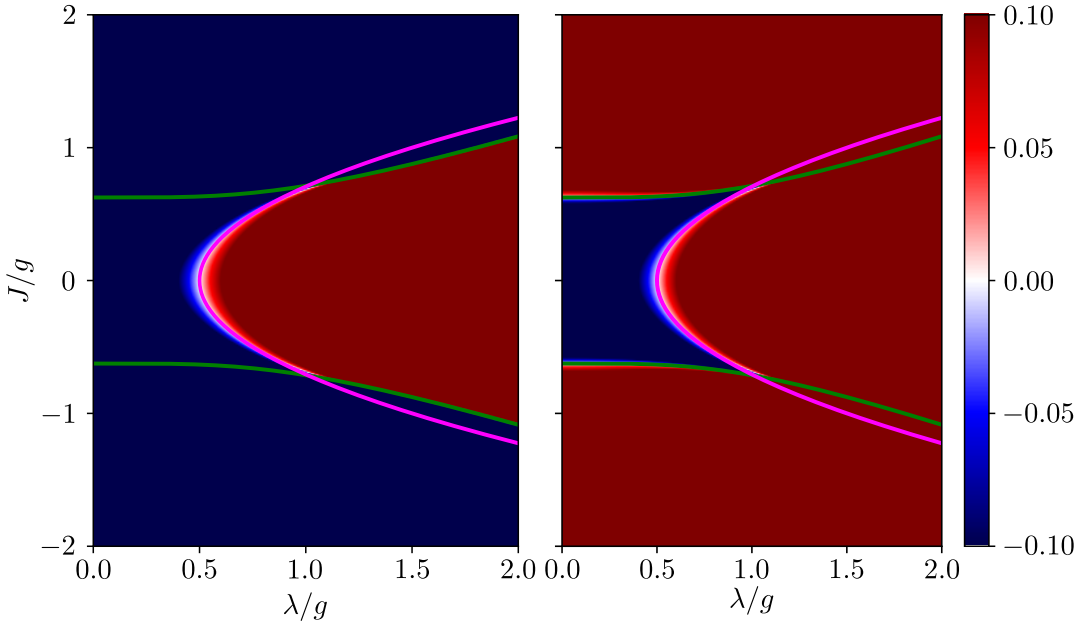

Figure 4.8: This figure shows a scan of the Jacobian eigenvalues which experience a sign change, ϵ_4 (a) and ϵ_6 (b). Each plot has 200×200 points. To highlight the phase boundaries the value range was artificially restricted to $\epsilon \pm 0.1$. These are the eigenvalues which let the normal state become unstable across the LMG-phase transition as well as the $\mathcal{PT}$-transition. The green line shows the critical J_c from Eq. 4.53, while the magenta line shows Eq. 4.57.

to zero, to reach an approximate expression for $\lambda_c(J)$.

$$\mathrm{Re}\{\mathcal{T}(\epsilon_4)|_{J=0}\} = \lambda - \gamma - \frac{J^2}{2}\frac{(\lambda^2+1)}{\lambda^3+\lambda} + \mathcal{O}(J^4) = 0 \tag{4.55}$$

$$\Rightarrow \lambda_c/g \approx \frac{1}{4}\left(1 + \sqrt{1+8J^2}\right) \tag{4.56}$$

$$\approx \frac{1}{4}\left(2 + 4J^2\right). \tag{4.57}$$

In the last line we expanded the expression for λ_c/g once more around small J/g. The expression we get is approximately quadratic in the LMG non-linearity, and as we can see in Fig. 4.8 fits the $\mathcal{PT}$-phase transition quite well for such a crude approximation.

The linear phase digram by itself would suggest that the outer lobes follow a similar mechanism, i.e. in each phase, the interaction strength λ will reach a critical value compared to the dissipation strength and drive the system across a $\mathcal{PT}$-symmetry

breaking phase transition. However, in the LMG phases the stable states differ at each point in parameter space. Thus an analysis of the eigenvalues of the Jacobian for a specific state won't tell us anything useful about the shape of the threshold or the corrections to the critical values. To investigate the outer lobes we will have to manually look at the mean-field trajectories at different points. Inspecting the mean-field trajectories suggest a more complex series of phase transitions, see the insets of Fig. 4.7 and in particular Fig. 4.9. The latter shows the trajectories at six points a long a λ/g-scan at $J/g = 1.5$.

The insets of Fig. 4.7 and the plots of Fig. 4.9 show typical mean-field trajectories in the $X_b - Y_b$-plane. We plot four example trajectories which we found to belong to different basins of attraction, i.e. they are characterised by their initial conditions which are given by:

$$\text{blue}: \ x = 1/\sqrt{2}, y = -1/\sqrt{2}, z = 0 \tag{4.58}$$

$$\text{red}: \ x = -1/\sqrt{2}, y = 1/\sqrt{2}, z = 0 \tag{4.59}$$

$$\text{orange}: \ x = 0, y = -1, z = 0 \tag{4.60}$$

$$\text{magenta}: \ x = 0, y = 1, z = 0 \tag{4.61}$$

In the normal phase at $\lambda/g = 0.25$ and $J/g = 0$ we see that all trajectories spiral towards the same fixed point - $X = 0,\ Y = 0,\ Z = 1$. At the center of the LMG phase at $\lambda/g = 0.25$ and $J/g = 1.5$ we see two separate stable fixed points appear. This suggests that the system underwent a pitchfork-bifurcation. This corresponds to the phase transition we see at the full quantum level, see Fig. 4.2 and Fig. 4.3. In the $\mathcal{PT}$-phase we see a single limit cycle which explains the vanishing expectation values on the quantum level. The interesting feature appears at $\lambda/g = 0.45$ and $J/g = 1.5$. Here we see two stable limit cycles as well as two stable fixed points appear, which become just two stable limit cycles beyond the apparent LMG-$\mathcal{PT}$ threshold. Such a region of bistability where one set of states becomes less and less present while another gains suggests that this is not a $\mathcal{PT}$-symmetry breaking phase transition but a simple first-order phase transition.

A more detailed investigation of mean-field trajectories was done as part of the comparison of mean-field parameter scans and full quantum simulations in Fig. 4.10. Fig. 4.11 shows the mean-field trajectories for the usual initial conditions Eq. 4.58 at five different points along the parameter scan at $J/g = 1.5$. The plots show four distinct phases and a region of bistability. In order from left to right: The LMG phase, the bistable region, the bicyclic phase, the monocyclic phase and finally chaos. The different cycles and fixed points are more pronounced for site b as we start in the phase were the pumped site has undergone a phase transition. The fact that the a site shows similar behaviour at all is not due to a phase transition on the a site, but due to the interaction between the sites. Note how in Eq.4.39 the λ-terms contain information about the X and Y-components of the other site. If the initial conditions lead to different X_b and Y_b, they will naturally lead to slightly different steady states for X_a, Y_a and Z_a as well.

These figures suggest a first-order phase transition from the LMG phase across the bistable region, of two stable limit cycles and two stable fixed points into what we call the bicyclic phase. This phase is characterized by two stable limit cycles. The figures further show that the two limit cycles coalesce into a single cycle, which suggests another second-order phase transition. Here, the bicyclic phase has two stable solutions for each site, which are related by a $\mathcal{Z}_2$-symmetry. This suggests a symmetry-broken phase which transitions into a symmetric state. Finally, we see this Monocyclic phase transition into chaos, where all spin-components on either site have zero expectation. This suggests that it is this last transition that is the $\mathcal{PT}$-symmetry breaking transition of these lobes.

4.4.3 Mean-field Comparisons

The next step of our investigation was concerned with comparing the results from mean-field with the exact behaviour of the full quantum model. The main purpose of these comparisons was again to ascertain how well the full quantum picture converges towards the mean-field predictions. Furthermore, we were interested in how the mean-field parameter scans themselves behave under the full model.

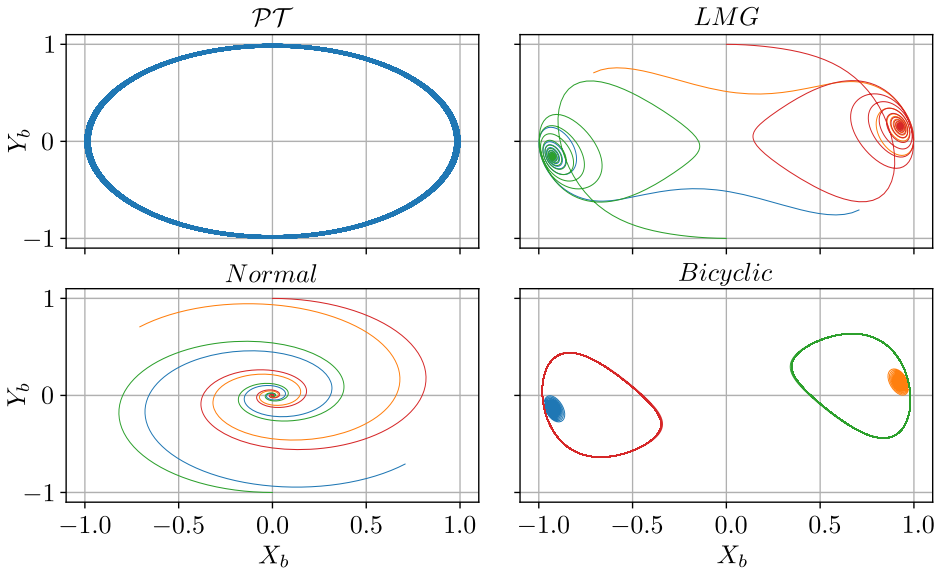

Figure 4.9: This figure shows the enlarged insets from Fig. 4.7. The plots are at $\lambda = 1.5, J = 0$ (a), at $\lambda = 0.25, J = 0$ (b), at $\lambda = 0.25, J = 1.5$ (c) and at $\lambda = 0.45, J = 1.5$ (d). For the bistable region the first 400 data points have been cut off, to emphasis that past the transitory phase the trajectory settles into two limit cycles on top of the two attractive fixed points. As we scanned primarily around the upper lobe, where the b-site becomes critical, we plot all trajectories in the X_b-Y_b-plane.

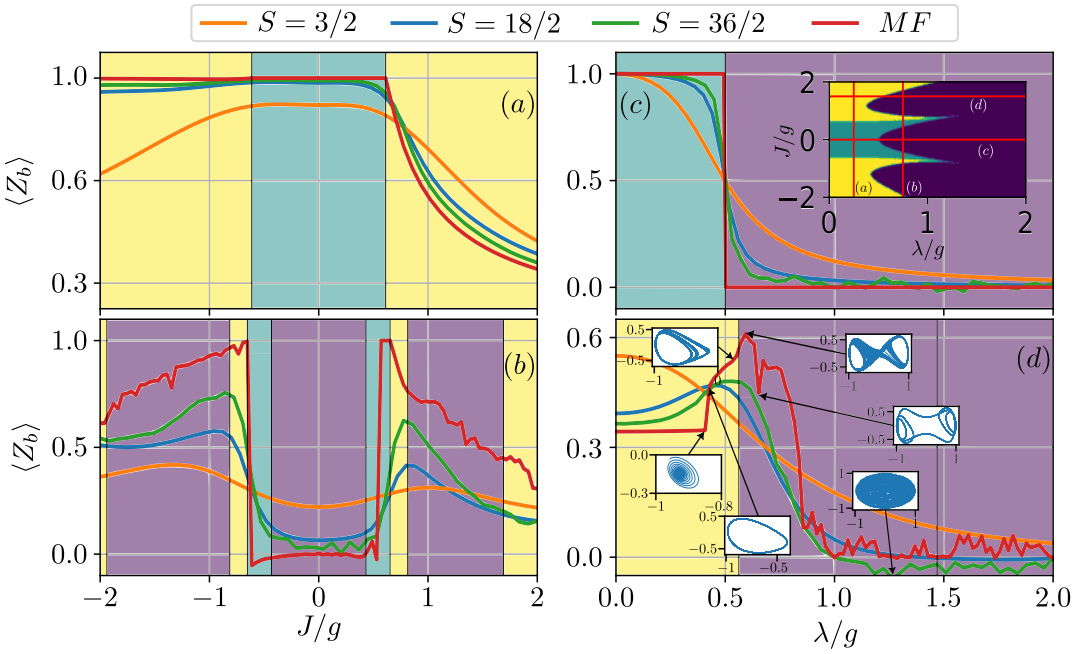

Figure 4.10: This figure compares parameter scans of our mean-field equations (green) with results from exact diagonalization (blue, orange) as well as Quantum Trajectories (green). The background color of the four main plots is chosen to match those of the phase diagram and give an indication of where the phase transitions are. Figure (a) and (b) are scans of the strength of the LMG non-linearity along $\lambda/g = 0.25(0.75)$ respectively. Scans (c) and (d) are along λ at $J/g = 0(1.5)$ respectively. The insets of figure (d) show the mean-field trajectories at different points along the scan.

To this end we began choosing four scans across the phase diagram. We picked two simple ones, which closely mimic the individual models. This was done as a sanity check, to ensure that the full model shows no unwanted or unexpected behaviour in the correct limits. The remaining two scans were more involved and ran across a variety of phase transitions. This made the overall stability of the numerical simulations as well as the overall convergence much worse. The results of these scans can be found in Fig. 4.10. The figure shows the evolution of the Z_b-expectation value along four lines. The background of the individual plots are lightly shaded to match those of the phase diagram, i.e. a yellow background means those parameters belong to one of the LMG phases. The inset in (c) shows the phase diagram as well as the lines along which the scans were performed. Each plot consists of four graphs, which corresponds to $S = 3/2$ (blue), $S = 9/2$ (orange), $S = 36/2$ (green) as well as mean-field (red). The data for $S = 3/2$ and $S = 9/2$ where generated with exact diagonalization, while for $S = 36/2$ we employed quantum trajectories. Plot (a) and (c) show the sanity checks along J/g and λ/g respectively. As in Fig. 4.3 as well as Fig. 4.6 we see an excellent convergence of the full quantum results towards the mean-field predictions. This suggests that the limits of the full model work as intended. Plot (b) shows a scan along J/g at $\lambda/g = 0.75$. This plot was chosen for its eight phase transitions. We can clearly see that while the various, closely packed phase transitions caused the semi-classical numerics some difficulties, it nonetheless follows the curve we would expect from our previous discussion. Crossing from the LMG phase over into the monocyclic phase, we see a smooth rise towards the expectation value of the normal state. This is followed by a sharp drop in expectation in the $\mathcal{PT}$-state. Afterwards we see a similar behaviour play out in reverse, up to the asymmetry in J/g. Other than the scans of the individual models we see a much slower convergence towards the mean-field solution in this case. Plot (d) shows a scan along λ/g at $J/g = 1/5$. Originally, we expected a single phase transition to occur across this line. Our discussion, however, suggested that we should expect a much more complicated picture of four phases and a region of bi-stability. Looking at the actual plot we see various points at which the slope of the graph suddenly changes, which usually indicates a change of state.

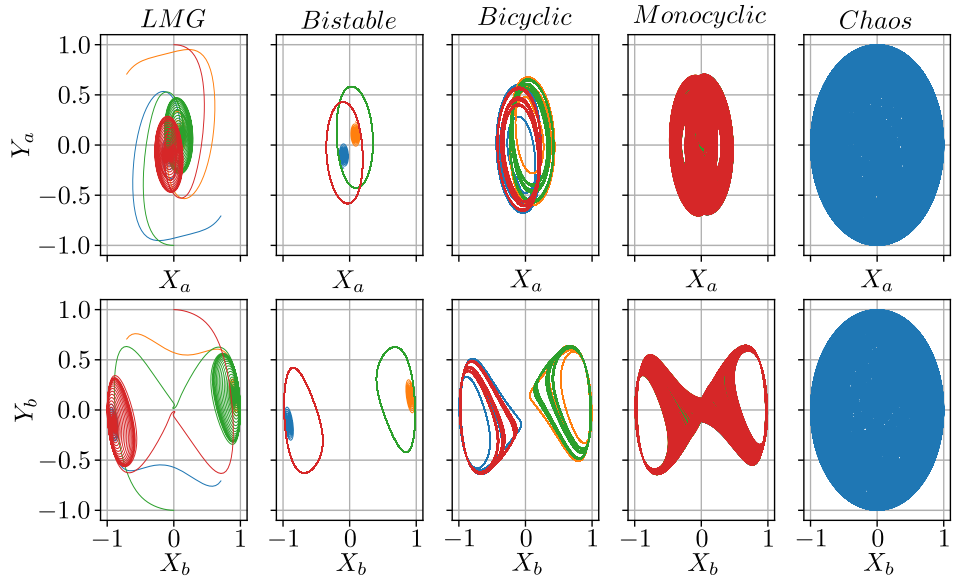

Figure 4.11: This figure shows the insets of Fig. 4.10 for the initial conditions of Eq. 4.58. In reading order the trajectories are at $J = 1.5$ and $\lambda/g = 0.408, 0.428, 0.531, 0.592, 1.469$, where we have omitted the trajectory at $\lambda/g = 0.653$ as we weren't able to ascertain if this was a true feature of the equations or an instability. As with the trajectories in Fig. 4.9 we have cut off the transient phases to emphasise the limit cycles, where appropriate.

The insets of plot (d) show the mean-field trajectories at the points where the slope changes most drastically. One can see again the stable solutions in the LMG phase ($\lambda/g = 0.408$), which evolves into a stable limit cycle before the LMG-PT phase transition ($\lambda/g = 0.428$). At the point of the phase transitions we see what appears to be period doubling in the limit cycles (($\lambda/g \approx 0.531$)). Shortly after he LMG-$\mathcal{PT}$ transition we can see that the initial conditions spreads across the (z=+1) pole of the Bloch sphere ($\lambda/g = 0.592$). At $\lambda/g = 0.653$ we see what appears to be period doubling closer to equator of the sphere, which causes the expectation to dip. This is a feature which is neither persistent across different solvers nor does it not seem present in the full quantum picture. We assume at this point that it is likely a numerical artefact. Towards larger λ/g we see the mean-field trajectory fill the entire bloch sphere, which indicates chaos ($\lambda/g = 1.469$).

The insets are presented in more detail in Fig. 4.11. In that figure we have omitted

the trajectory found at the dip in plot (d) as we weren't able to ascertain if that was a feature or a numerical instability. To understand the remaining five insets better, we used the four initial conditions from Eq. 4.58, which we found to belong to four different basins of attraction. The figure shows the mean-field trajectories for both spins at positive J/g. That is the region in which the pumped site (b) goes critical. Hence, why all effects are much more pronounced in the $X_b - Y_b$-plane. Due to the spin-flip coupling between the two sites we do see similar effects for the dissipative site, albeit much more muted.

From left to right it shows the trajectories are at $J = 1.5$ and $\lambda/g = 0.408$, 0.428, 0.531, 0.592, 1.469. We can clearly see that it transitions from a region of two stable fixed points to a region where both limit cycles and fixed points are stable, to a region where only limit cycles are stable. This suggests a first-order phase transition across a region of bi-stability. As the fixed point before, these two limit cycles are connected via $\mathbb{Z}_2$-symmetry, namely a rotation around the Z-axis. This transitions to a phase of a single limit cycle, which suggests a second-order phase transition. Finally, we see what we assume to be a $\mathcal{PT}$-symmetry breaking phase transition from a single solution to chaos, mimicking the transition from the normal phase to the $\mathcal{PT}$-phase. A visualization of our current working hypothesis is shown in Fig. 4.12. This figure shows a rough sketch of all phase transitions of the top half of the phase diagram of Fig. 4.7. The three main phases are the well known normal phase (turquoise), the LMG phase (yellow) and the $\mathcal{PT}$-phase. Going off of the known $\mathcal{PT}$-symmetry breaking transition, we assume that for such a transition to occur, we require a unique steady state before the transition. We know that the normal phase and the LMG phase are connected via a symmetry breaking phase transition, which creates two fixed points in the LMG phase. This forces the systems through a variety of phases as the coupling strength is increase, as it tries to reach a phase with a unique steady-state from which it can transition into a $\mathcal{PT}$-phase.

We saw in the $\mathcal{PT}$-phase of the center lobe of Fig. 4.7 that the $\mathcal{PT}$-Hamiltonian causes the fixed point of the normal phase to transition into a limit cycle in the $X-Y$-plane in the $\mathcal{PT}$-phase. Something similar occurs in the LMG-phase where the $\mathcal{PT}$-

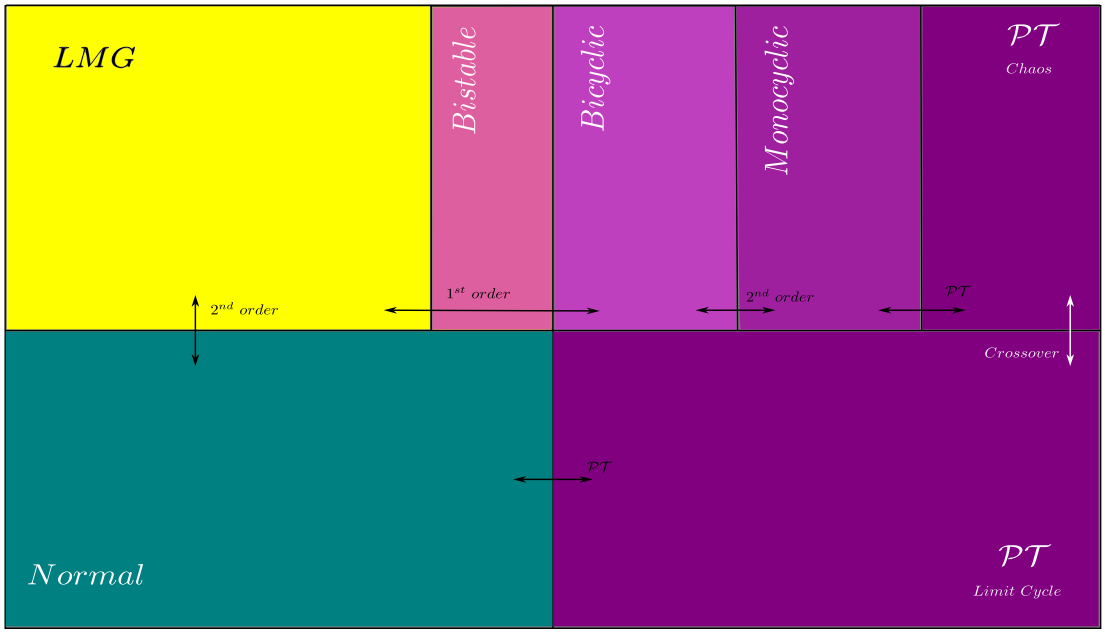

Figure 4.12: A rough sketch of all suspected phases of the model. In addition to the known transitions we see the bistable region, the bicyclic phase, as well as the monocyclic phase. As limit cycles are not detected by simple linear stability analysis, these phases did not appear in the linear stability phase diagram.

Hamiltonian causes each individual fixed point to transition into a limit cycle. However, whereas the limit cycle of the $\mathcal{PT}$-phase is unique and spreads around the entire equator of the Bloch sphere, the limit cycles that occur near the LMG-phase have a finite Z-component. Hence, this cannot be a $\mathcal{PT}$-symmetry breaking phase transition, see Ch. 3. The appearance of limit cycles centred around the fixed points also doesn't change the symmetry properties of the state. Hence this must be a first-order phase transition. This explains the appearance of a region of bistability where both fixed points and limit cycles are stable. As the coupling strength increases we see it expand the limit cycles until they touch and merge at the north pole of the Bloch sphere. At this point the system undergoes a further second-order phase transition to a monocyclic phase. This is now a unique steady-state which attracts all initial conditions. Increasing the coupling any further pushes the system across the $\mathcal{PT}$-symmetry breaking phase transition of the outer lobes. While the coupling Hamiltonian prefers a large limit cycle in the $X-Y$-plane, the LMG non-linearity causes this cycle to topple and spread across the

surface of the Bloch sphere.

4.4.4 Spin Wigner

The final piece we needed was a better understanding of the phase space of the full quantum model. In classical dynamics the phase space is the space spanned by the degrees of freedom as well as their time derivatives. In low-dimensional classical models the phase space gives full information about the state of system and its immediate future. Plotting trajectories in phase space for sufficiently many initial conditions then gives full knowledge of all possible states and evolutions. Here we will compare the trajectories of the mean-field equations of Eq. 4.35 with the so called spin-Wigner distribution in phase space. In bosonic systems one such representation is given by the Wigner functions or Wigner quasi-probability functions. Others such as P and Q functions also exist. Wigner functions assign each point in position-momentum space a probability density, which allows for a neat visualization of the states in phase space. Spin-Wigner functions are analogous but not entirely equivalent to the bosonic Wigner functions. They are the absolute value squared of the expectation value of a spin-coherent state

$$\mathcal{W}(\theta, \phi) = |\mathrm{Tr}[\rho_{ss}\kappa(\theta, \phi)]|^2. \tag{4.62}$$

Here, $\phi \in [0, 2\pi)$ and $\theta \in [0, \pi]$ are spherical coordinates of a point on the surface of the Bloch sphere. $\kappa(\theta, \phi)$ is the coherent state density matrix at that point and ρ_{ss} is the steady-state density matrix. Preceding the discussion of our results will be a brief derivation of these spin-coherent states.

In Bosonic systems a coherent state is the state of the harmonic oscillator which most closely resembles a classical harmonic oscillator, in the sense that it minimizes the amplitude-phase uncertainty. Furthermore, the peak of its probability distribution always follows the classical trajectory under time evolution. For spins something similar can be defined, in the sense that spin-coherent states minimizes the uncertainty of S_x, S_y, S_z. The following derivation follows in broad strokes the one found in [102].

We begin our derivation of the spin-coherent state by defining the vacuum state to

be $|0\rangle = |s, -s\rangle$, i.e. the down state. Then we have:

$$S^2 |s, m\rangle = s(s+1) |s, m\rangle \tag{4.63}$$

$$S^z |s, m\rangle = m |s, m\rangle \tag{4.64}$$

$$S^+ |s, m\rangle \propto |s, m+1\rangle \tag{4.65}$$

$$S^- |s, m\rangle \propto |s, m-1\rangle \tag{4.66}$$

$$S^- |0\rangle = 0. \tag{4.67}$$

We can then write $n = m + s$. We further have the identities:

$$S^+ S^- = S^2 - S_z^2 + S_z \tag{4.68}$$

$$S^- S^+ = S^2 - S_z^2 - S_z. \tag{4.69}$$

These allow us to determine the normalization constants of the operators S^+ and S^-:

$$\langle n| S^- S^+ |n\rangle = \langle n| S^2 - S_z^2 - S_z |n\rangle \tag{4.70}$$

$$= (2s - n)(n + 1) \tag{4.71}$$

$$\Rightarrow S^+ |n\rangle = \sqrt{(2s - n)(n + 1)} |n + 1\rangle \tag{4.72}$$

as well as:

$$\langle n| S^+ S^- |n\rangle = \langle n| S^2 - S_z^2 + S_z |n\rangle \tag{4.73}$$

$$= n(2s - n + 1) \tag{4.74}$$

$$\Rightarrow S^- |n\rangle = \sqrt{n(2s - n + 1)} |n - 1\rangle . \tag{4.75}$$

With this we are in a position to calculate $(S^+)^p |n\rangle$:

$$(S^+)^p |n\rangle = \sqrt{(2sn - n)(n + 1) \cdots (2s - n - p + 1)(n + p)} |n + p\rangle . \tag{4.76}$$

Acting on the vacuum state, this simplifies to:

$$(S^+)^p \left|0\right\rangle = \sqrt{\frac{2s!p!}{(2s-p)!}} \left|p\right\rangle . \tag{4.77}$$

In analogy with the Bosonic coherent states we define the state:

$$\begin{aligned} \left|\mu\right\rangle &= \frac{1}{\sqrt{N}} e^{\mu S^+} \left|0\right\rangle && (4.78)\\ &= \frac{1}{\sqrt{N}} \sum_{p=0}^{\infty} \frac{\mu^p}{p!} (S^+)^p \left|0\right\rangle && (4.79)\\ &= \frac{1}{\sqrt{N}} \sum_{p=0}^{2S} \mu^p \sqrt{\frac{2s!}{(2s-p)!p!}} \left|0\right\rangle . && (4.80) \end{aligned}$$

The normalization of this state is then:

$$\begin{aligned} 1 = \left\langle\mu|\mu\right\rangle &= \frac{1}{N} \sum_{p,q=0}^{2S} \mu^{*p}\mu^q \sqrt{\frac{2s!}{(2s-p)!p!}} \sqrt{\frac{2s!}{(2s-q)!q!}} \left\langle p|q\right\rangle && (4.81)\\ &= \frac{1}{N} \sum_{p=0}^{2s} |\mu|^{2p} \frac{2s!}{(2s-p)!p!} && (4.82)\\ &= \frac{1}{N} \sum_{p=0}^{2s} |\mu|^{2p} \binom{2s}{p} && (4.83)\\ &= \frac{1}{N} (1+|\mu|^2)^{2s}. && (4.84) \end{aligned}$$

Hence,

$$\sqrt{N} = (1+|\mu|^2)^s. \tag{4.85}$$

With this the coherent state is given by

$$\left|\mu\right\rangle = \frac{1}{(1+|\mu|^2)^2} e^{\mu S^+} \left|0\right\rangle . \tag{4.86}$$

In this formulation the state is parametrized by the real part $\mathcal{R}(\mu)$ and the imaginary part $\mathcal{I}(\mu)$. A more useful parametrization can be derived by projecting every point of a sphere uniquely onto the plane spanned by $\mathcal{R}(\mu)$ and $\mathcal{I}(\mu)$, see Fig. 4.13.

Thus one finds a parametrization of the state in terms of the two angles $\phi \in [0, 2\pi)$

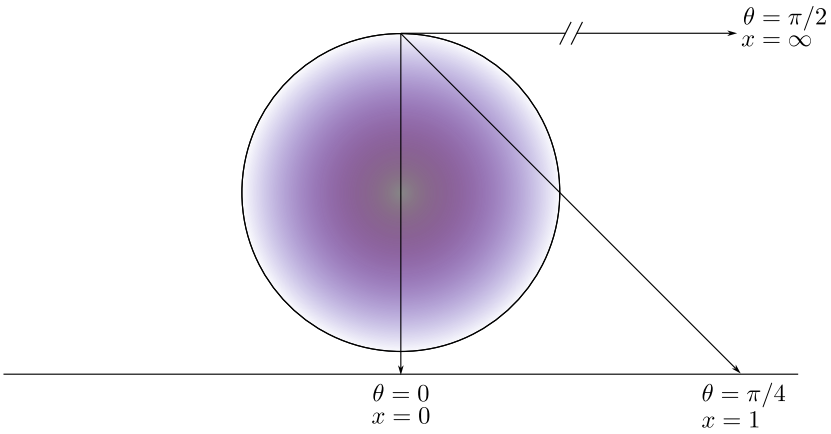

Figure 4.13: A sketch of the conversion between the two coordinate systems. Each point of the sphere is uniquely projected onto the sphere and vice versa. A slight issue arises at the north pole of the sphere, which is projected to infinity.

and $\theta \in [0, \pi]$ we have seen above:

$$\mu = e^{i\phi}\tan(\theta/2). \tag{4.87}$$

We then have $|\mu|^2 = \tan^2(\theta/2)$ and $1 + |\mu|^2 = \sec^2(\theta/2)$:

$$|\mu\rangle \to |\theta, \phi\rangle = \frac{1}{\sec^2\left(\frac{\theta}{2}\right)} \exp\left(e^{i\phi}\tan\left(\frac{\theta}{2}\right) S^+\right)|0\rangle\,. \tag{4.88}$$

With this the coherent state density matrix we have used in Eq. 4.62 is given by:

$$\kappa(\theta, \phi) = |\theta, \phi\rangle\langle\theta, \phi|\,. \tag{4.89}$$

Now we have derived a spin-coherent state parametrized by the spherical angles θ and ϕ. This will allow us to get a decent first impression of the behaviour of the full quantum model, by visualizing it on the surface of the Bloch Sphere. At this stage we need to note that these are not fully analogous to bosonic coherent states. The most important difference comes from the fact that the spin Hilbert space is limited, while the bosonic Fock space is not. Bosonic coherent state truly are an infinite superposition of Fock states, and each time one applies the annihilation operator a, the number of states at the top don't change. This is contrast to spin-coherent state. Each time we

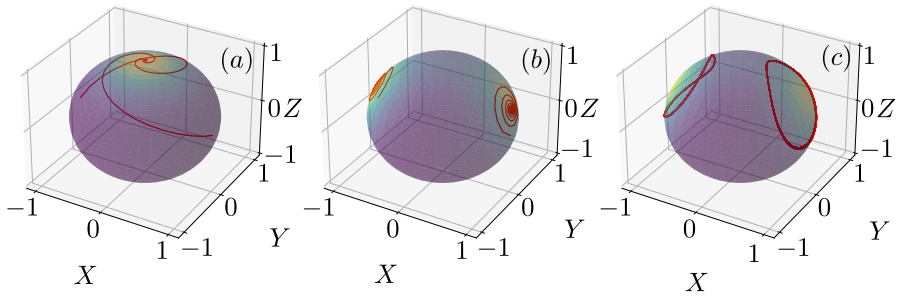

Figure 4.14: This Plot shows a comparison of spin-Wigner functions for S=6/2 with mean-field trajectories in 3 distinct phases. The comparisons are done for the driven site b. (a) Normal Phase at $J/g = \lambda/g = 0$, (b) LMG Phase at $J/g = 1.5$, $\lambda/g = 0$ and (c) Bicyclic Phase at $J/g = 1.5$, $\lambda/g = 0.5$.

apply either of the spin-lowering operator, we effectively remove a state from the finite sum, until at last we reach the bottom. This doesn't change the fact, though, that they are still very useful tools to represent spin states in their phase space.

In quantum mechanics one does not have absolute knowledge of position and momentum. One can however calculate probabilities and plot those in phase space. These phase-space probability functions are known as Wigner-functions. For spins something closely related exists, called spin-Wigner functions. They assign each point on the bloch sphere a probability density, which allows for a neat visualization. In our case ,they are the expectation values of a spin-coherent state with a non-equilibrium steady-state. Ordinary coherent states are states of the linear harmonic oscillator. They are known to be the most "classical" quantum states in the sense that they minimize the uncertainty between position and momentum as well as that the time evolution of the probability distribution they define, is centred around the classical trajectory. Ordinary coherent states can be derived as the eigenstates of the annihilation operator. Spin-coherent states are the spin-analogues of coherent states. They were derived to be the most

classical spin, i.e. a point on the Bloch-sphere.

The spin-Wigner function on site b is then given by $\mathcal{W}_b$:

$$\mathcal{W}_b(\theta,\phi) = \left| Tr\left[\rho_{ss}^b \kappa(\theta,\phi)\right]\right|^2 \tag{4.90}$$

$$\kappa(\theta,\phi) = |\theta,\phi\rangle\langle\theta,\phi| \tag{4.91}$$

$$|\theta,\phi\rangle = cos^{2s}(\theta/2) exp\left[tan(\theta/2) exp(i\phi) S^-\right]|\uparrow\rangle\,. \tag{4.92}$$

Here ρ_{ss}^b is the partial density matrix of site b. $\kappa(\theta,\phi)$ is the spin-coherent state density matrix parametrized by spherical angles. As the spin has a fixed length, the radius was taken to be constant and omitted. The spin-coherent state itself is given by the last expression. In Fig. 4.14 the results of full scans over θ and ϕ has been plotted onto sphere for the normal phase (a), the LMG phase of site b (b) as well as the bistable phase (b). The liens in red show sample mean-field trajectories. In all cases we see excellent agreement of the center of the spin-wigner function and the fixed-point or the centres of the limit cycles respectively. This agreement between the full quantum simulation and the mean-field results gives us confidence that the conclusions drawn from mean-field are really there in the full quantum dynamics.

4.5 Summary and Outlook

In this part of the thesis we discussed the competition of equilibrium and dissipative phenomena in the context of a collective spin-dimer. We found that the $\mathcal{PT}$-symmetry breaking phase transitions occur between phases with a unique steady-state and a phase of vanishing expectation values. The parameter which drives the system across this transition is the coupling strength, which mixes the states of the two spins.

We began our investigation with a detailed discussion of the phase diagrams of the individual models, namely the LMG-model of Eq. 4.1 as well as the $\mathcal{PT}$-model of Eq. 3.1. We choose the open LMG model for its symmetry breaking phase transition which is directly connected to an equilibrium phase transition. The $\mathcal{PT}$-model was chosen for its well understood $\mathcal{PT}$-symmetry breaking phase transition, which is a

purely non-equilibrium phenomenon.

Using linear stability analysis we developed a first phase diagram, which separates phases by the number of stable states. We find two different, linearly stable phases and one large phase of no stable solutions. The linearly stable phases are the normal phase, in which the only stable solution is the state dictated by the Lindblad operators as well as the LMG phases. The LMG phases are technically two different phases as the either the dissipative or the driven state becomes critical, while the other remains the in normal state.

As part of a closer investigation of the mean-field trajectories we compared parameter scans across the phase diagram with results from the full quantum model. We found the full quantum model to overall converge well towards the mean-field predictions. We also found that the scans possessed more structure than the linear stability phase diagram would suggest. Closer investigation of the mean-field trajectories revealed that the picture was more complicated than linear-stability suggested. We found that between the LMG phase and the phase of zero stable solutions is not a $\mathcal{PT}$-symmetry breaking phase transition but a first-order phase transition from two fixed points to two stable limit cycles. We further found another second-order phase transition which restores the original $\mathbb{Z}_2$-symmetry of the normal state. This monocyclic phase finally transitions into $\mathcal{PT}$-symmetric state.

This suggests that a $\mathcal{PT}$-symmetry breaking phase transition is generally preceded by a phase with a unique steady-state. As of yet, this is a conjecture and we have not yet found a rigorous proof.

Finally, we used spin-Wigner functions to compare the mean-field predictions to quasi-probability functions of the full spin systems. We found that the trajectories either converge or encircle the regions of highest probability density.

Possible avenues of future research include working out the precise mechanics of the $\mathcal{PT}$-symmetry breaking transition. Furthermore, one could attempt to find a generalization of the symmetry conditions of $\mathcal{PT}$-symmetry breaking to $\mathcal{Z}_n$ which include possible generalization of the $\mathcal{T}$-symmetry.

Part II

Liouville Density Machines

Chapter 5

Introduction

5.1 Review of Numerical Methods

In this part of the thesis we will discuss a neural quantum state for non-equilibrium steady states which we developed in Ref. [5]. Similar to the previous part, our discussion will come in three parts. In this chapter we will discuss the context of our research as well as review the relevant literature. Ch. 6 will then focus on the the concrete ansatz we propose as well as its shortcomings and how we handle them. It will derive and discuss two optimization schemes, one could use and discuss the MCMC method, which is necessary to estimate the gradient of the cost with respect to the network parameters.

In the previous part of the thesis we investigated a $\mathcal{PT}$-symmetric LMG-dimer. We found that the competition of equilibrium-connected phenomena, like the LMG-transition, as well as purely dissipative effects such as the $\mathcal{PT}$-symmetry breaking transition, leads to a rich phase diagram. One of the reasons we chose the LMG-dimer was its accessibility to analytic methods like the mean-field approximation, and the subsequent numerical integration of just six equations of motion. Furthermore, the linear scaling of the state space with the size of the spin made exact numerical simulations of comparatively large spins possible.

These large spin-sizes and small spatial dimensions are the crux of the matter though. In the case of the LMG model we have a single degree of freedom, but as

soon as we go to larger models we run into an exponentially scaling state space. This is even worse in open quantum systems where the state is given by a density matrix which grows as the square of the Hilbert space of the equilibrium model. Naturally, this drastically limits the size of systems that are accessible to numerical simulations and makes it very difficult to make concrete statements about which phases are stable in the thermodynamic limit of most systems.

Luckily, nature is local. As a consequence, while the state space might grow exponentially fast, few of those states contribute with a finite weight to the groundstate of equilibrium systems or the steady states of open quantum systems, see Refs. [67, 103]. This fact allowed the emergence of two rough categories of approaches to emerge.

One set is stochastic in nature and uses the fact that the weights with which each state contributes can be regarded as a probability. These probabilities can be used to generate configurations either directly or as a Markov chain, see Ch. 6, and arrive at an approximation of the ground- or steady state distribution. Generally, all of that is necessary for this is knowledge of a function which is proportional to the true probability distribution. This set of methods consists of the many different Monte Carlo methods which have been developed since as early as the 1930s by Fermi [104]. The other set attempts to compress the state by filtering out the most important basis states, i.e. those which contribute with the greatest weight. The most important methods of this class are based on tensor networks.

Both types of algorithms are concerned with finding an accurate and efficient way to represent the problem using a smaller space of parameters. One does so stochastically by moving through configuration space and spending more time in high-weight regions. The other does so by fixing a number of parameters and optimizing them such that the ansatz minimises the systems energy. A method which bridges the apparent gap between stochastic methods and compression methods is called *Variational Monte Carlo* (VMC). In VMC one defines an "ansatz" or "trial" wavefunction, which parametrises the true wavefunction in some way. By expanding the energy in terms of this ansatz wavefunction, one can cast it into a form which can be estimated via *Markov Chain Monte Carlo* (MCMC). Similarly, one can estimate the gradient of the energy with

respect to the ansatz parameters with Monte Carlo. This allows for very straightforward optimisation of the ground- or steady state distribution. The expanded energy looks like

$$E_\alpha = \sum_s \left[\frac{|\Psi_\alpha(s)|^2}{|\Psi_\alpha|^2} \times \sum_{s'} \langle s|H|s'\rangle \frac{\Psi_\alpha(s')}{\Psi_\alpha(s)} \right], \tag{5.1}$$

where s and s' run over all possible basis states and were introduced in the expansion of the energy expectation value. Here Ψ_α is an ansatz parametrized by a set of parameters α. The first factor on the right-hand-side defines a probability distribution over the basis configurations:

$$p(s) = \frac{|\Psi_\alpha(s)|^2}{|\Psi_\alpha|^2}, \tag{5.2}$$

while the second factor is called the "local energy":

$$E_{\text{loc}}(s) = \sum_{s'} \langle s|H|s'\rangle \frac{\Psi_\alpha(s')}{\Psi_\alpha(s)}. \tag{5.3}$$

By drawing samples from the unknown probability distribution via MCMC, one can estimate the energy as a simple average over the samples, see Ch. 6 and Refs. [16, 105, 106]. The quality of convergence critically depends on the quality of trial wavefunction, i.e. the closer the parameter structure of the ansatz function the easier and better the overall convergence. One such ansatz wavefunction was recently proposed by the authors of Ref. [17]. Their proposed ansatz is called *Neural Quantum States* (NQS) and is based on the ability of *Neural Networks* (NN) to efficiently represent complex probability distributions. It further uses their non-local nature to efficiently encode long range correlations. It has shown great promise in both 1D and 2D equilibrium systems and some attempts at extensions to non-equilibrium steady state (NESS) have been made. This part of the thesis is concerned with developing and benchmarking an ansatz density matrix for a NESS. It makes use of the Choi-isomorphism which has already been used by the authores of Ref. [19]. Similar to vectorized density matrices in MPS the proposed ansatz is not generally physical. As we will see in Ch. 6 and Ch. 7, it nevertheless converges towards a physical NESS in all cases and outperforms the *Neural Density Machine* (NDM) ansatz, which was the state-of-the art NESS NQS

at the time of writing.

Now we have a rough overview of some of the most widely used methods in the context of this thesis as well as our goal. We will spend the next few paragraphs briefly going into more detail on Monte Carlo and Tensor network methods and elucidate their strengths and weaknesses and where our ansatz fits in. In the next chapter we will give a technical introduction to our ansatz as well as an explanation of why and how it can find a physical steady state even though it is neither Hermitian nor positive.

The first set of methods we have to discuss are the stochastic Monte Carlo methods. In the previous part of the thesis we already encountered two examples of Monte Carlo implementations. The first was the groundstate Monte Carlo method we used for the 2D classical Ising model, where we started from a "cold" state and randomly flipped spins until we reached the ground state configuration, see Ch. 2. The second implementation were the quantum trajectories we used to approximate the steadystate density matrix. At each time step we flipped a weighted coin and decided either to evolve it coherently or perform a quantum jump. Performed over enough trajectories the estimate will become exact, see the Ch. 3 as well as Refs. [27, 68, 69].

The precursor of modern Monte Carlo was first developed and used by Enrico Fermi in the 1930s. It was later extended by Ulam and von Neumann while they were working at Los Alamos. Ref. [104] contains a summary of the history of the method. Since its inception Monte Carlo has been widely used to solve integrals [107], optimization problems, or to generate samples from an unknown probability distribution [108, 109]. All of these applications make use of an underlying probability distribution in one way or another. Integration techniques for example often use the ratio of some trial space to the value of the integral. Probably the most famous example of this is the calculation of π. One takes a quarter circle confined to a box and randomly generates dots in the total space. As $N \to \infty$ the ratio of dots inside the circle to the dots outside the circle will approach $\pi/4$, see [110] for an excellent introduction to Monte Carlo methods.

Drawing samples from an unknown porbability distribution is the application that is most relevant to this thesis. It is incredibly useful when one cannot normalise their wavefunction due to the sheer size of the state space but still requires an estimate

of distribution of the basis states in the ground state or steady state. The standard algorithm for this is called "Markov Chain Monte Carlo" (MCMC), see Ch. 6 and in particular Ref. [16] for a detailed discussion of the algorithm, its history and its convergence properties.

MCMC and in particular the Metropolis-Hastings algorithm have found many applications, from finding the ground state of the Ising model at different tempertures, see Ch. 2, over the estimation of spin-glass states [111–113], to the estimation of expectation values and gradients, see for example Ch. 6 and Ref. [16] for the general derivation as well as Ch. 7 and Ref. [5, 17] for concrete applications.

In particular the authors of [111] proposed an interesting extension of the MCMC algorithm, which proves very useful. In their proposal several Markov chains at different "temperatures" run in parallel and exchange samples at set steps in the optimization. The "temperature" in this case is a factor which scales the acceptance probability of samples. Low temperatures strongly favouring low-energy configurations, while high temperature chains will scan large areas of configuration space. This has the effect that main Markov chain will more likely find the global energy minimum more reliably. This has been successfully applied to spin glasses [111], correlated electronic structure problems [114] and the 1D Hubbard model [115], among others. For a detailed review see Ref. [116].

5.2 Matrix Product States and Tensor Networks

In the last section we briefly discussed the most widely regarded family of stochastic methods. We will now turn our attention towards compression algorithms and specifically Tensor Networks.

One of the most powerful compression algorithms for 1D quantum states are *Matrix Product States* (MPS) [117]. They are derived by considering the set of expansion parameters of an arbitrary wavefunction as a tensor.

$$|\Psi\rangle = \sum_{\{\phi_i\}} \Psi_{\phi_1\phi_2\ldots\phi_N} |\phi_1 \ldots \phi_N\rangle \tag{5.4}$$

Here ϕ_i denotes one of D local physical states. This tensor is the iteratively broken apart into a product of smaller tensor via a single value decomposition:

$$\Psi_{\phi_1\phi_2\ldots\phi_N} = \Psi_{\phi_1,(\phi_2,\ldots\phi_N)} = \sum_{a_1} A^{\phi_1}_{1,a_1} \Sigma_{a_1,a_1} (V^*)_{a_1,(\phi_2\ldots\phi_N)} \tag{5.5}$$

$$\equiv \sum_{a_1} A^{\phi_1}_{1,a_1} \Psi_{a_1\phi_2\ldots\phi_N} \tag{5.6}$$

Here, $A^{\phi_1}_{1,a_1}$ represents the state of site 1 and its correlations with the rest of the chain. Note that A not only has a *physical index* ϕ_1 but also so called bond-indices a_1, which store a sites correlations with the rest of the chain. After the full tensor has been completely broken apart the final MPS reads:

$$|\Psi\rangle = \sum_{\{\phi_i\}} \sum_{\{a_i\}} A^{\phi_1}_{1,a_1} A^{\phi_2}_{a_1,a_2} \ldots A^{\phi_{N-1}}_{a_{N-2},a_{N-1}} A^{\phi_N}_{a_{N-1},1} \left|\phi_1 \ldots \phi_N\right\rangle . \tag{5.7}$$

The total dimension of these auxiliary indices is called the *bond dimension* and it determines the total correlation capacity of the states. The original state can be reconstructed by *contracting* i.e. summing over bond indices:

$$C_{a,c} = \sum_b A_{a,b} B_{b,c}. \tag{5.8}$$

This example shows simple matrix multiplication. Two matrices share an index, b. Once that is contracted, the remaining matrix is indexed by a and c. An equally important example is that of an expectation value:

$$D = \sum_{a,b} A_a B_{a,b} C_b. \tag{5.9}$$

After this contraction no index is left, which means the result must be a scalar. This is exact and can represent any state in the Hilbert space as long as the size of these bond dimensions grow exponentially. Fig. 5.1 shows a graphical representation of an MPS (a). The physical indices ϕ_i are represented by the horizontal lines, whereas the bond indices a_i are represented by the vertical lines. The colored circles represent the tensors

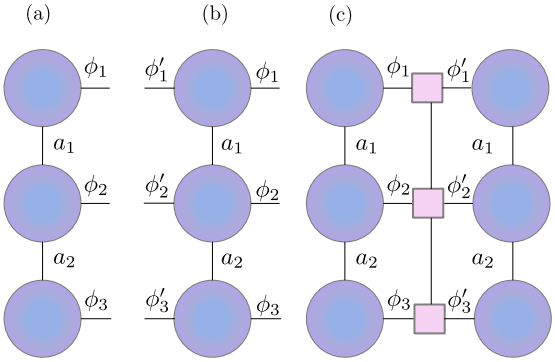

Figure 5.1: This figure shows three diagrammatic representation of a matrix product state (a), a matrix product operator (b) as well as of an expectation value (c). The horizontal lines are called "legs" and represent the physical indices ϕ_i as well as their conjugates ϕ'_i, whereas the vertical lines represent the bond indices a_i. The expectation value is calculated by contracting, i.e. summing over all shared indices.

which describe the states of the sites $A^{\phi_i}_{a_{i-1},a_i}$. Fig. 5.1(c) shows diagrammatically how an expectation value can be calculated. After physical indices are connected to a corresponding local operator all indices are summed over, i.e. "contracted".

The SVD decomposes a matrix M into singluar values as well as left and right singular vectors. The singular values correspond to the importance or weight with which each singular vector contributes to the original matrix. Hence, the main use of the SVD step is to make a low-rank approximation [66, 67, 118], i.e. find a smaller matrix $\bar{M}$ which nevertheless contains most of the important information of the original matrix. As this happens during the break up of the wavefunction, this is a very simple and highly efficient way of compressing the exponentially large wavefunction. This way of compressing the state leads to a so-called *truncation error*.

Operators can be decomposed in a similar fashion, except they will have two physical indices instead of one. They can be connected to MPS by *contracting* the shared physical index. This allows one to calculate expectation values. For MPS one can always find so-called canonical forms, which make contracting and calculating expectation values very straight forward [66, 67].

MPS turned out to be the theoretical foundation of the *Density Matrix Renormalization Group* algorithm (DMRG). A very powerful groundstate algorithm proposed in the 1990s, see Ref. [64]. A time evolution method based on a Trotter-Suzuki

decomposition [119] was developed in 2004, called the *Time Evolving Block Decimation* (TEBD), see Ref. [65]. It decomposes a global time evolution operator into a product of local time evolution operators which act only on two neighbouring sites:

$$e^{-i\mathcal{H}\Delta t} = e^{-ih_1\Delta t/2}\dots e^{-ih_{N-1}\Delta t/2}e^{-ih_{N-1}\Delta t/2}\dots e^{-ih_1\Delta t/2} + \mathcal{O}(\Delta t^3). \tag{5.10}$$

The operators h_i are called bond-gates and are defined to act on the sites connected by the ith bond, i.e. i and $i+1$ in the case of a chain. Each bond h_i is acted upon twice, once sweeping forward along the chain and once backward. In addition to the truncation error above it adds the *Trotter Error* which stems from the approximate decomposition of the time evolution operator. We must note here that coherent evolution drives up the entanglement, which generally limits the time one can evolve an MPS. Both methods have extensions to the thermodynamic limit, see [120] for iDMRG and [121] for iTEBD.

Over the years MPS have proven to be exceptionally powerful and efficient when it comes to accuracy and speed. They are, however, not without flaws. For one, the truncation error limits it to low-entangled states. Highly entangled states require a large bond-dimension which causes the method to become inefficient. Furthermore, the way they are decomposed makes handling long-ranged Hamiltonians cumbersome during TEBD. While these Hamiltonians can be handled via so-called *swap-gates*, their states tend to exhibit a larger entanglement. Generally, they are best suited for representing short-range 1D, gapped Hamiltonians [66, 67]. The entanglement of low-energy states of such Hamiltonians has been proven to follow a so called area-law [122–124], i.e. it grows with the area between two subsystems instead of their volume.

The extension to two and higher spatial dimensions is called *Projected Entangled Pair States* (PEPS), see Ref. [125]. To truncate the tensor of PEPS in the context of real or imaginary time evolution there are two proposed truncation schemes. After a time step the bond dimension will have increased. The simple update scheme (SU) [126] will truncate it "locally", i.e. simply cut it back to the bond dimension using SVD. The "full update" scheme (FU) [127] instead takes the entire wavefunction into account when choosing which singular values to neglect. This is optimal yet very costly.

PEPS have certain issues that MPS do not have. For one they do not allow for an exact canonical form, which makes calculations of expectations values and entanglement spectra more difficult. Furthermore, exact contractions of PEPS is always exponentially costly in systems size [67, 128]. For both issues approximate methods have been developed, see Ref. [67] and the references therein. Nevertheless, PEPS are severely limited compared to their 1D counterparts.

As we have discussed in Part I and the introduction to this part, we are interested in investigating the NESS of open quantum systems. As we have seen in Ch. 2 this generally involves density matrices or, using the Choi isomorphism [19], density kets. These scale much worse than pure states, exacerbating the need for efficient numerical methods. An issue we have in open quantum systems which does not exist in this form in equilibrium systems is that the NESS is the end-point of a time-evolution. As we have seen in Ch. 3 the Liouvillian contains both coherent and incoherent parts. The first will generally increase the entanglement while the incoherent part will drive the system into a steady-state. If the dissipation is weak, the system will pass through a high-entanglement region before a NESS is reached, which will inevitably rake up a large truncation error or blow up the bond dimension. In either case, this renders the weak-dissipation limit difficult to access with these methods.

In the previous section we have seen that MPS have proven to be extremely effective at representing groundstates in equilibrium systems. Here we will discuss various methods which have since been put forward to extend them to open systems. For a more detailed discussion see Ref. [77].

One of the first methods put forward are *Matrix Product Density Operators* (MPDOs), see Ref. [129]. Similar to MPS they decompose the tensor of coefficients of the full density matrix as a product of tensors. Each tensor represents then the mixed state of a site as well as the correlations with the rest of the chain. This MPDO can be written in terms of a pure state by employing the local purification method described in Ref. [130].

Purification is a method which relates a mixed state on a Hilbert space to a pure

state on a larger Hilbert space. It uses the Schmidt decomposition of pure states

$$|\Psi\rangle = \sum_i s_i |A_i\rangle \otimes |B_i\rangle \tag{5.11}$$

which writes a pure state as a tensor product of the states of two subsystems of the total system. A_i and B_i are the ith Schmidt basis vectors of subsystem A and B respectively. s_i is the ith expansion coefficient. Consider now a mixed state whose eigen-decomposition is known

$$\rho = \sum_i p_i |\phi_i\rangle \langle\phi_i| . \tag{5.12}$$

By adding so called auxiliary sites a_j we can artificially enlarge the Hilbert space in which the physical state lives and define the following pure state using the Schmidt decomposition:

$$|\psi\rangle = \sum_j \sqrt{p_j} |\phi_j\rangle \otimes |a_j\rangle . \tag{5.13}$$

The original density matrix can be easily recovered by tracing out the virtual sites:

$$\rho = \mathrm{Tr_a} \left[|\psi\rangle \langle\psi| \right] \tag{5.14}$$

$$= \mathrm{Tr_a} \left[\sum_{ij} \sqrt{p_i}\sqrt{p_j} |\phi_i\rangle \langle\phi_j| \otimes |a_i\rangle \langle a_j| \right] \tag{5.15}$$

$$= \sum_i p_i |\phi_i\rangle \langle\phi_i| . \tag{5.16}$$

The resulting state can then be time evolved using the TEBD algorithm, where any operator only acts on the physical sites. The virtual sites are left untouched by any operation and exist only to enlarge the Hilbert space. Note, that the decomposition of a physical density matrix guarantees that MPDOs are physical themselves.

A method presented in [19] makes use of the Choi-Isomorphism instead of a local purification. This relates a matrix to a vector

$$\rho = |\psi\rangle \otimes \langle\psi| \rightarrow |\rho\rangle\rangle = |\psi\rangle \otimes |\psi\rangle . \tag{5.17}$$

This is a simple way of making the density matrix representable as an MPS and open it TEBD. However, this does not guarantee a physical density matrix across the entire evolution. As long as the time evolution is governed by a Liouvillian, this should still lead to a physical NESS. This is similar to the approach we took in Ch. 6 and Ch. 7.

An alternative approach was taken by the authors of [131]. They used that the operator $\tilde{H} = \mathcal{L}^\dagger \mathcal{L}$ is hermitian and that the ground state is equal to the NESS of $\mathcal{L}$. This opens $\tilde{H}$ up to variational approaches which targets the groundstate directly. This was later extended to infinite chains in [132]. An issue with this is that while $\mathcal{L}$ might be strictly local in its interactions, $\mathcal{L}^\dagger \mathcal{L}$ will be highly non-local. In addition to this issue, if $\mathcal{L}$ has small eigenvalues close to a transition, then $\mathcal{L}^\dagger \mathcal{L}$ will have even smaller eigenvalues, effectively leaving some states extremely long-lived. This might make a treatment more cumbersome. See for this the discussion in Ref. [133].

The first foray into 2D open quantum systems in the thermodynamic limit was done by the authors of [134]. Similarly to the authors of Ref. [19] they made use of the Choi-Isomorphism. For the time-evolution they employ the SU proposed in [126]. For the efficient evaluation of observables they employed the corner transfer matrix method outlined in Ref. [135]. The authors discuss the shortcomings of time-evolution for finding the NESS in the context of PEPS. As mentioned above, coherent time evolution causes the entanglement to increase, which limits the time one can evolve. This limits the method to strong dissipations. The authors suggest that one could evolve to the NESS in a strong dissipation limit and use the resulting state as the initial state at slightly weaker dissipations to reach sensible NESS in the weak dissipation limit.

It was pointed out by the authors of [133] that SU is not optimal. While it reaches a fixed point for a wide range of parameters, this point might go unstable if the bond dimension is reached. Furthermore, there are parameter ranges where no NESS is ever found. The authors believe, that there is a bond dimension for which SU will produce sensible NESS, but they were not able to find it.

A different approach was taken by the authors of Ref. [136]. They too vectorize the density matrix and do a full time integration using TEBD. The main difference to [134] lies in the update scheme used to truncate the bond dimension. While [134]

employs simple updates and truncates locally, the authors of Ref. [136] use a full update scheme adapted from Ref. [137]. The corner transfer matrix method they employ follows Ref. [138]. The authors were able to show that the full updates allow for much better convergence, albeit at a much higher numerical cost. In particular a strong and moderate damping they see excellent or good convergence towards. In the weak dissipation limit the results are excellent for small times and begin to diverge at longer times, as expected from an entanglement-limited method. This is a non-trivial limitation as the Lindblad master equation is derived explicitly in the limit of weak dissipation. This restricts the applicability of this class of methods to problems where large dissipations can be justified. Overall, tensor network methods remain unbeaten in one spatial dimension but tend to suffer in two and higher dimensions as well as for long range interacting problems.

As we have mentioned above, recently a new class of ansatz wavefunction for VMC was proposed by Carleo and Troyer [17, 139]. This class of ansatz wavefunctions is based on neural networks and their exceptional capacity to extract the most relevant features of a given set of data. Already in their seminal paper they showed that their ansatz beat PEPS in a 10×10 AF Heisenberg model in accuracy. A few attempts have since been made at defining a positive-hermitian *Neural Quantum State* (NQS) ansatz for NESS density matrices. The ansatz we proposed in [5] and which we will discuss further in the following chapters will forgo physicality constraints in favour of efficiency.

In the following sections we will give a brief overview of the equilibrium and open quantum system NQS ansatze in 1D and 2D in a similar fashion to MPS and PEPS above. We will discuss their strengths and weaknesses and attempt to elucidate where our ansatz fits into this picture.

5.3 Neural Network Quantum States

In recent years Neural Networks have found broad applications in a variety of fields and many different architectures have been developed. Several of these architectures have since found applications in physics as *Neural Quantum States* (NQS). Before moving

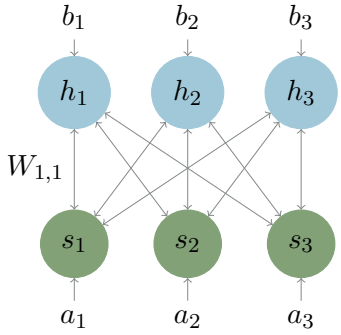

Figure 5.2: This figure shows a schematic representation of the RBM architecture. RBMs are bipartite networks consisting of hidden units denoted by h_1 and visible units denoted by s_i and represented by the blue and green circles respectively. Each unit has a bias denoted as b_i for the hidden biases and a_i for the visible biases. The ith visible unit and the jth hidden unit are connected by a weight $W_{i,j}$. The weights and biases of the network are the parameters of the network which will be optimized to represent some probability distribution.

on to NQS, we briefly introduce some neural network nomenclature. Generally, neural networks consist of various layers of nodes or units, which are connected via links. Each node and link has an associated parameter. The node-parameter are called "biases", while the link-parameter are called "weights". Layers which are used to provide input or which provide an output are dubbed "visible", while all other layers are called "hidden".

The architecture which is probably simplest and most widely used are the so-called *Restricted Boltzmann Machines* (RBMs) [17, 139–142]. RBMs consist of one visible and one hidden layer with no intra-layer connections, see Fig. 5.2 for a schematic. The units of the visible layer correspond to the physical degrees of freedom s, whereas the "hidden" are artificial helper nodes h. These nodes can take two different but arbitrary values. This is sometimes referred to as "labelling freedom". The inter-layer connections can be either dense, i.e. each hidden node is connected to each visible node, or sparse.

Classically, the parameters α of an RBM are real-valued. They infer a probability

distribution over the input samples

$$P_\alpha(\vec{v},\vec{h}) = \frac{e^{(-E_\alpha(\vec{s},\vec{h}))}}{Z_\alpha} \tag{5.18}$$

$$Z_\alpha = \sum_{s,h} e^{(-E_\alpha(\vec{s},\vec{h}))}, \tag{5.19}$$

by minimizing a free-energy like quantity:

$$E_\alpha(\vec{s},\vec{h}) = \sum_j a_j s_j + \sum_i b_i h_i + \sum_{ij} W_{ij} h_i s_j. \tag{5.20}$$

Here, α stands for the network parameters (weights and biases), s_j denotes the state of the jth visible unit (up, down; 0,1). This can for example be used in recommender systems, where each sample represents a person and each input represents, say, a movie they like $s_j = 1$, dislike $s_j = 0$, or have not seen yet $s_i = -1$. The latter is not a viable input value and merely tells the program to ignore that node in the evaluation. In such an inference step one would first calculate the conditional activation of the hidden nodes depending on the input, while ignoring $s_i = -1$

$$p(\vec{h}|\vec{s}) = \prod_j p(\vec{h}_j|\vec{s}), \tag{5.21}$$

and from that hidden vector the conditional activation of the visible nodes

$$p(\vec{s}|\vec{h}) = \prod_k p(\vec{s}_k|\vec{h}). \tag{5.22}$$

This yields a new vector $\tilde{s}$ in which previously unseen movies $s_i = -1$ are now either marked as probably disliked $s_i = 0$ or as probably liked $s_i = 1$. The probability with which each is flipped, can be used to rank the recommendations. While we do not much care about movie recommendations, the ability of learning and inferring from a probability distribution is exactly what a numerical ansatz for a wave-function needs to do. This, their simplicity and their obvious ties to two coupled classical Ising chains, has led to RBMs to be chosen as the first Neural Quantum State (NQS) in 2017 [17].

We now know understand the basic structure and classical uses of RBMs. In the following few paragraphs we will discuss how to use them as neural quantum states. What we wish an NQS to learn is the probability distribution over the basis states within the ground-state. Taking inspiration from the classical RBM we can identify $P_\alpha(s,h) \to \Psi_\alpha(s,h)$. We are however interested in the marginal probability distribution which only depends on s. Hence we define the following ansatz wave-function:

$$\Psi_\alpha(s) = \sum_{\{h_i\}} e^{\sum_j a_j s_j + \sum_i b_i h_i + \sum_{ij} W_{ij} h_i s_j}. \tag{5.23}$$

Here $\{h_i\}$ denotes the set of all hidden units and s_j denotes the spin-component in z-direction of the jth spin. Hence, s is some spin-configuration in the z-basis. As before each visible unit can only take two values and we have to make a choice on basis. The sum then runs over both values each hidden unit can take. We can use the labelling-freedom of RBMs and choose for the hidden units $h_i = \pm 1$. This allows us to perform the sum explicitly and simplify the expression:

$$\Psi_\alpha(s) = e^{\sum_j a_j s_j} \times \prod_{i=1}^{M} 2\cosh\left[b_i + \sum_j w_{ij} s_j\right]. \tag{5.24}$$

This wave function ansatz now allows us to define an energy which we can later minimize. As the network now represents an actual physical quantity, the energy is no longer something abstract, but the actual physical energy:

$$E_\alpha = \frac{\langle \Psi_\alpha | \, H \, | \Psi_\alpha \rangle}{|\Psi_\alpha|^2}. \tag{5.25}$$

This is not an expression which is of much use to us. To reach an expression we can

easily handle, on a configuration-to-configuration basis, we need to do a little algebra:

$$E_\alpha = \frac{1}{|\Psi_\alpha|^2} \sum_{s,s'} \Psi^*_\alpha(s)\Psi_\alpha(s')\langle s|H|s'\rangle \tag{5.26}$$

$$= \frac{1}{|\Psi_\alpha|^2} \sum_{s,s'} \frac{|\Psi_\alpha(s)|^2\Psi_\alpha(s')}{\Psi_\alpha(s)}\langle s|H|s'\rangle \tag{5.27}$$

$$= \sum_s \left[\frac{|\Psi_\alpha(s)|^2}{|\Psi_\alpha|^2} \times \sum_{s'} \langle s|H|s'\rangle \frac{\Psi_\alpha(s')}{\Psi_\alpha(s)} \right] \tag{5.28}$$

$$= \sum_s p(s;\alpha) \times E_{\mathrm{loc}}(s;\alpha). \tag{5.29}$$

With this we have two expressions, which can be calculated for an individual spin-configuration. As we will see, this will come in handy during training, when we generate configurations, or samples, using Monte Carlo, see 6.4 for the detailed algorithm. Here, $p(s;\alpha)$ defines the probability distribution over the sample space. The so-called "local energy" is defined by

$$E_{\mathrm{loc}}(s;\alpha) = \sum_{s'} \langle s|H|s'\rangle \frac{\Psi_\alpha(s')}{\Psi_\alpha(s)}. \tag{5.30}$$

The sum runs over states which are connected via the Hamiltonian. As long as the Hamiltonian is sparse, i.e. local in its interactions, this can be evaluated very efficiently.

A difference to the classical RBM, which we have not yet discussed, is that the wave function has both a probability amplitude as well as a phase. To be a proper ansatz wave function, the RBM needs to learn both. There are broadly speaking two ways of handling this. Either one has two separate networks which learn the different parts, or one employs complex parameters. Both ways have been discussed in the literature and successfully implemented, see Refs. [17, 21, 143]. We will make use of complex-valued parameters.

There are several important reasons for the wide use of RBMs. For one, and this cannot be overstated, they are exceedingly simple and easy to implement. The logarithmic derivative, which plays an important role in the optimization of the variational energy Eq. 5.1, can be calculated analytically and hard-coded, see Ch. 6. This makes for a very efficient calculation of the derivatives. Furthermore, they are very

well understood in terms of tensor network theory. In particular [18, 141] have worked out under which circumstances RBMs can be mapped unto MPS and vice versa. This allowed them to find upper bounds of the RBMs entanglement capacity. They could show that *sparse* RBMs follow a similar area-law as MPS, while *dense* RBMs follow indeed a volume-law. This opens up a large class of states to numerical studies that were not accessible by TNs before. For further studies into the expressivity of NQS see Refs. [144, 145], and for discussion of a correspondence of deep learning and the renormalization group see Ref. [146]. In contrast to *Recurrent Neural Networks* (RNNs) for example, RBMs are amenable to simple symmetrization which increases their performance drastically, see Ref. [143] for a detailed discussion of the comparison as well as Ref. [147] for discussion of possible symmetrization strategies for RNNs. RBMs have been successfully used to study the groundstate of the 1D *Transverse Field Ising* model (TFI) as well as the 2D Heisenberg model [17]. Further studies include quenched TFIs [148] as well as the $J_1 - J_2$-model [149]. A recent publication by Ciuti et al. discusses possible ways of doing accurate time evolution with autoregressive models, see Ref. [150]. This could be of interest when one were to consider RNNs as candidates for an open-system density matrix.

Another architecture which has found some application as a NQS are the aforementioned RNNs, see Refs. [147, 151–154]. RNNs belong to the class of autoregressive models. RBMs and other "feed-forward" type models take as input a configuration and provide as output the complex amplitude $\Psi_\alpha(s)$. A RNN on the other hand recurrently builds a configuration from scratch as

$$\Psi_\alpha(\vec{s}) = \Psi_\alpha(s_1) \times \Psi_\alpha(s_2|s_1) \times \cdots \times \Psi_\alpha(s_N|s_1, s_2, ..., s_{N-1}), \tag{5.31}$$

by feeding the configuration and the state of the hidden units back into itself. This allows one to draw independent samples from the overall probability distribution without resorting to MCMC. As well discussed in Ref. [143] this has the advantage of not having to care about autocorrelation times, however, it is also not parallelizable in a similar fashion as MCMC. Furthermore, it is also not as amenable to symmetrization strategies

as non-autoregressive models which can significantly hamper performance.

The last major class of NQSs we will discuss here are *Convolutional Neural Networks* (CNNs), see Refs. [155–158]. CNNs use a set of convolutional filters on each layer to better capture spatial correlations. The structure and process are explained in Ref. [156]. The authors of Ref. [159] have shown that deep CNN are more efficient at representing volume-law entangled states than shallow RBMs. CNNs have the advantage of being a deep architecture by design, as seen in Ref. [141, 159] drastically improves their entanglement capacity. As discussed in Ref. [156] the parameter structure is also somewhat independent of input size. The authors use the same CNN for the $J_1 - J_2$-model at various sizes. They mention that a well converged ansatz at smaller size can help convergence at a larger size. As discussed by the authors of Ref. [143] CNNs also appear to be suited for scaling to larger system sizes, due to the favourable scaling of parameter number and evaluation cost in system size compared to RBMs and RNNs. The main trade-off is that it is much more complex in structure and implementation. Furthermore, while the number of parameters might remain constant at increasing system size it could be overkill at smaller system sizes, drastically reducing optimal convergence time.

NQS have also been used to study the dynamics and NESS of driven-dissipative open quantum systems. In this section we will briefly discuss the three main ways this has been attempted in the literature as well as their strengths and weaknesses. As we have seen with TNs, open quantum systems pose a more complex challenge than equilibrium systems. For one, we have both coherent and incoherent dynamics. We also have that the system state is generally mixed and must be described by a positive-semi definite and hermitian matrix with unit trace. Developing an ansatz which is guaranteed to fulfil these physicality constraints is as difficult for NQS as it was TNs. As far as we are aware, the only way of guaranteeing a physical density matrix at every step of the optimization is some sort of purification scheme. These are similar to those used previously with TNs and are based on the ansatz from Ref. [130].

Early ansatze sought to purify RBMs, see Refs. [21, 160–163]. All of them have in common the use some additional hidden layer of auxiliary sites, which encode the

systems entanglement with the environment. Tracing these auxiliary sites out then leaves a mixed state. While they may differ in the exact details of the parameter structure or protocols for restoring the system density matrix from the pure state, they are ultimately quite similar in spirit and performance. In Ch. 7 we will use in particular Ref. [21] as that ansatz is pre-implemented in the *NetKet* library [164].

More recently [165] proposed a purified deep autoregressive network. It has shown an improved accuracy over the shallow networks, at the cost of higher complexity. As an autoregressive network, special care needs to be taken when symmetrizing the state if it is possible at all. This could diminish its scalability. Another extension on purified RBMs are the purified CNNs of [166]. This ansatz' parametrisation is scale invariant and translational symmetry is easy to implement. It has been shown to improve upon the results of Ref. [21] for a fifth of the parameters.

In particular the shallow ansatze suffer from their inability to represent mixed product states without the use of hidden units. As we will see in Ch. 7, this drastically reduces their correlation capacity and severely limits their ability to efficiently represent stationary states for many models of interest.

Another very powerful ansatz, which nevertheless does not guarantee physicality, involves the use of *Positive Operator Valued Measures* (POVMs), see Refs. [153, 167, 168]. The POVM formulation uses that given an informationally complete set of measurement operators $M^{\mathbf{a}}$, one can define a probability distribution over all possible measurement outcomes.

$$P^{\mathbf{a}} = \mathrm{Tr}\left(\rho M^{\mathbf{a}}\right). \tag{5.32}$$

Here, for a single-spin POVM $M = \{M^a\}$ is a positive semi-definite matrix with the normalization $\sum_a M^a = \mathbb{1}$, [167]. The N-spin operator corresponding to a specific measurement $\mathbf{a} = a_1 \cdot a_2 \ldots a_N$ is then just the tensor product

$$M^a = M^{a_1} \otimes \cdots \otimes M^{a_N}. \tag{5.33}$$

Solving Eq. 5.32 for ρ yields

$$\rho = P^{\mathbf{a}} \left(T^{\mathbf{a}\mathbf{a}'} \right)^{-1} M^{\mathbf{a}}, \tag{5.34}$$

with $T^{\mathbf{a}\mathbf{a}'} = \mathrm{Tr}\left(M^{\mathbf{a}} M^{\mathbf{a}'} \right)$ [168]. One can now take the time derivative of Eq. 5.32. Together with the Lindblad master equation Eq. 2.12 and Eq. 5.34 one then reaches a master equation for $P^{\mathbf{a}}$:

$$\dot{P^{\mathbf{a}}} = \mathcal{L}^{\mathbf{a}\mathbf{b}} P^{\mathbf{b}}. \tag{5.35}$$

This is the Lindblad master equation in terms of the measurement outcomes. It can be split into a unitary $\mathcal{F}^{\mathbf{a}\mathbf{b}}$ and a dissipative part $\mathcal{D}^{\mathbf{a}\mathbf{b}}$

$$\mathcal{L}^{\mathbf{a}\mathbf{b}} = \mathcal{U}^{\mathbf{a}\mathbf{b}} + \mathcal{D}^{\mathbf{a}\mathbf{b}}, \tag{5.36}$$

where the unitary part is given by

$$\mathcal{U}^{\mathbf{a}\mathbf{b}} = \mathrm{Tr}\left(-i\mathcal{H} \left[T^{-1\mathbf{b}\mathbf{b}'} M^{\mathbf{b}'}, M^{\mathbf{b}} \right] \right) \tag{5.37}$$

and the dissipative part by

$$\mathcal{D}^{\mathbf{a}\mathbf{b}} = \mathrm{Tr}\left(\sum_k A_k T^{-1\mathbf{b}\mathbf{b}'} M^{\mathbf{b}'} A_k^\dagger M^{\mathbf{a}} - \frac{1}{2} \{ T^{-1\mathbf{b}\mathbf{b}'} M^{\mathbf{b}'}, M^{\mathbf{a}} \} \right), \tag{5.38}$$

see the supplementary material of Ref. [168]. The operators A_k are the Lindblad or jump-operators. This equation has as its steady state the probability distribution which with Eq. 5.34 leads to the stead-state density matrix. As $P^{\mathbf{a}}$ is a probability distribution itself, one can use any network architecture suited to learning probability distributions to represent it. The authors of Ref. [168] have presented a time dependent variational principle to solve Eq. 5.35. The main weakness they identify is the lack of guaranteed positivity of their ansatz. The results however, speak for excellent expressibility of their ansatz in the NESS.

An alternative route has been taken by the authors of Ref. [169]. Similar to the authors of Ref. [19] 15 years before them they employed the Choi-Isomorphism to

rewrite the density matrix as a density ket. Numerically the state is represented by a RBM with one additional "fictitious" unit per visible unit which takes care of the additional two local basis states. Similar to the TN case, this approach does not guarantee physicality. To work around this, the authors use that $\mathcal{L}^\dagger\mathcal{L}$ is a hermitian operator whose groundstate, $|\rho_0\rangle\rangle$ corresponds to the NESS of $\mathcal{L}$,

$$\mathcal{L}\rho_0 = 0. \tag{5.39}$$

They then use an ordinary variational approach to target the groundstate of hermitian operator. This approach has several issues however. The first is the use of the hermitian operator $\mathcal{L}^\dagger\mathcal{L}$. As discussed previously, while L might be sparse, the number of non-zero elements of $\mathcal{L}^\dagger\mathcal{L}$ grows approximately quadratically in system size and possesses long-range interactions. This increases both memory and computation cost.

5.4 Liouville Density Machines

In the last section we have discussed various approach of representing the NESS of a Lindbladian system as a NQS. A common issue we encountered is the waste of correlation capacity on uncorrelated states. In the purified ansatze an additional layer of hidden units is introduced to incorporate the mixedness. In the ansatz of Ref. [169] part of the mixedness was taken care of by the incorporation of a second unit per spin. To represent arbitrary mixed product states, correlations between these units were required however.

This issue is what we attempt to iterate upon in our publication Ref. [5]. Our ansatz is based on the insight of the authors of Ref. [20]. They developed an extension of RBMs to three possible input values and showed that it was the most compact representation possible. We used this insight to develop an RBM ansatz that makes full use of the Choi-Isomorphism and lives entirely in Liouville space. Our ansatz makes full use of the advantages of a dense RBM, i.e. volume-law capacity, labelling freedom and analytical gradients without having to use hidden units, i.e. correlation capacity, on product states.

In Ch. 6 we will explain the architecture in more detail, as well as how and why we can find the steady-state despite having a technically non-physical ansatz. In Ch. 7 we will present and discuss our results and discuss possible avenues for improvement.

Chapter 6

LDM Theory

In the previous chapter we have discussed various different approaches to numerical simulations of correlated many-body systems as well as their advantages and disadvantages. A method which is of particular interest to us is *Variational Monte Carlo* (VMC). In VMC one defines an ansatz or trial wave function whose number of parameters grows polynomial in system size. These parameters are then iteratively updated until the ansatz represents a target state with the desired accuracy. A class of ansatz functions which has been proposed recently are based on neural networks, and most importantly the *Restricted Boltzmann Machine* (RBMs). In this chapter we propose and discuss an extension to RBMs which targets the non-equilibrium steady state of open quantum systems. We will build upon our previous of Sec. 5.3 and discuss how such an RBM can be used to find the ground state using stochastic gradient descent in Sec. 6.1. In Sec. 6.2 we will introduce our ansatz. In Sec. 6.3 we discuss the *Stochastic Reconfiguration*, an extension of stochastic gradient descent which will help us to reliably reach the steady-state with our ansatz. Finally, in Sec. 6.4 we discuss the Markov chain Monte Carlo method we have briefly mentioned in Ch. 5 in more detail and provide pseudocode for a simple implementation.

6.1 Ground State Algorithm

In Sec. 5.3 we have discussed various possible neural quantum state ansatze with a particular focus on RBMs. We have introduced the general architecture as well as how it can be used to represent a quantum state. We have, however glanced over one of the central aspects of neural networks: the optimisation. Training a neural network often entails the minimisation of some cost function. Classically, cost functions are functions which measure the distance of the network's prediction from some the ground truth, i.e the expected outcome, in the case of the supervised learning, or from the original input in the case of unsupervised learning. Here, supervised learning means that a set of labelled data exists. The network will then be trained to align its own output given some input data with the corresponding label. In unsupervised learning the data is not labelled and the network attempts to find patterns and fit probability distributions by mimicking the input data, i.e. the parameters are optimized such, that the output of the network is as close to the input as possible. This is usually done by minimizing some sort of cost or energy function.

In the case of neural network quantum states the physical energy plays the role of the cost function. In this section we will briefly explain how to find the ground state of a complex-valued NQS. This algorithm is very similar to how we will find the steady-state and there is merit in explaining it here first.

As we have seen above, the energy for some set of parameters is given by

$$E_\alpha = \sum_s p(s;\alpha) \times E_{\mathrm{loc}}(s;\alpha). \tag{6.1}$$

To understand how to minimize this it is illustrative to think of the energy as the height of hilly landscape and the parameters as coordinates. The gradient, i.e. the derivative of the energy with respect to its parameters is the vector which points in the direction of the steepest ascent.

$$f(\alpha) = \nabla E_\alpha \tag{6.2}$$

If we were to follow the gradient, i.e. add it to the parameters, we would be sure to

move towards the nearest peak of the landscape. Similarly, we move in the opposite direction, we are sure to move away from the peak and towards some minimum

$$\alpha' = \alpha - \eta f(\alpha), \tag{6.3}$$

where η is the "learning rate". It determines how far we follow the gradient. If η is small we are most likely to always follow the optimal route down the energy landscape, but it will likely take a long time to converge. On the other hand, if η is very large, one is more likely to overshoot in a certain direction, i.e. actually go up in energy. If the path down the energy landscape is reasonably flat, this can speed up convergence.

This idea is called gradient descent. There are a few issues with this. For one, we are taking the derivative of a real-valued-complex-parametrised function. To do that, we will make use of the so-called "Wirtinger" calculus. Another issue is the usual "curse of dimensionality", i.e. the Hilbert space grows exponentially in systems size. This means that calculating the normalization of the probability distribution in Eq. 5.29 is impossible. Local minima are another issue. They can cause *Stochastic Gradient Descent* (SGD) to get stuck at suboptimal solutions. Lastly, we don't know yet what the gradient actually looks like.

6.1.1 Wirtinger Calculus:

Wirtinger Calculus as we employ it here has been thoroughly discussed in the Ref. [170] and we will merely give a very brief introduction to the idea. Generally, any function of a complex variable z can be written as

$$f(z) = u(x, y) + iv(x, y), \tag{6.4}$$

where $z = x+iy$. Complex functions are said to be holomorphic if they are differentiable in the complex plane, i.e. when they fulfil the Cauchy-Riemann equations. As $f(z)$ is strictly real in the case of a cost function, it cannot be holomorphic. i.e. no complex derivative exists. What Wirtinger now used was that one can treat a real-valued function $f : \mathbb{R}^2 \to \mathbb{R}^2$ ($\mathbb{R}$) in the complex plane by introducing conjugate coordinate

$z^* = x - iy$ to $z = x + iy$. This allows us to do a coordinate transformation from $(x, y) \to (z, z^*)$ and $f(x, y) \to f(z, z^*)$ by calculating the inverse relations $x = (z+z^*)/2$ and $y = -(z - z^*)/2$. With this we can then write the complex derivative of $f(z, z^*)$ as

$$\frac{\partial f}{\partial z} = \frac{1}{2}\left(\frac{\partial f}{\partial x} - i\frac{\partial f}{\partial y}\right) \tag{6.5}$$

$$\frac{\partial f}{\partial z^*} = \frac{1}{2}\left(\frac{\partial f}{\partial x} + i\frac{\partial f}{\partial y}\right). \tag{6.6}$$

Eq. 6.5 is now the complex derivative we have been looking for. Concretely, we have $f(z) = E_\alpha$, where α is a vector of complex parameters. Hence, whenever we write something like $\partial E_\alpha / \partial \alpha_i$ it is

$$\frac{\partial E}{\partial \alpha_i} = \frac{1}{2}\left(\frac{\partial E}{\partial \mathcal{R}(\alpha_i)} - i\frac{\partial E}{\partial \mathcal{I}(\alpha_i)}\right), \tag{6.7}$$

that we implement numerically.

6.1.2 Gradient Descent

Now that we have a notion of what it means to take the complex derivative of a non-holomorphic function, let us move on to the remaining two issues: The exponentially large state space and the concrete expression of the derivative of the energy with respect to the parameters α.

The expression of the derivative is independent of the concrete variational ansatz and has been derived in Ch.6.3 of [16]. Here we just give a summary of the key steps without going into great detail. We begin with the formal expression for the gradients

$$f_i = \frac{\partial E_\alpha}{\partial \alpha_i} = \frac{\partial}{\partial \alpha_i}\frac{\langle \Psi_\alpha | H | \Psi_\alpha \rangle}{|\Psi_\alpha|^2}. \tag{6.8}$$

and note that the parameter dependence lies wholly with the state Ψ_α. By introducing the logarithmic derivative

$$O_i(s) = \frac{1}{\Psi_\alpha(s)}\frac{\partial \Psi_\alpha(s)}{\partial \alpha_i}, \tag{6.9}$$

we can write a small variation of the state as

$$|\Psi_{\alpha+\delta\alpha_i}\rangle = (1 + \delta\alpha_i O_i)\,|\Psi_\alpha\rangle + \mathcal{O}(\delta\alpha_i^2). \tag{6.10}$$

As a next step we define a normalised wave-function:

$$|\nu_{0,\alpha}\rangle = \frac{|\Psi_\alpha\rangle}{||\Psi_\alpha||}, \tag{6.11}$$

and a set of states orthogonal to it:

$$|\nu_{i,\alpha}\rangle = (O_i - \bar{O}_i)\,|\nu_{0,\alpha}\rangle\,, \tag{6.12}$$

with $\bar{O}_i = \langle\nu_{0,\alpha}|\,O_i\,|\nu_{0,\alpha}\rangle$. Next we work out the normalised state with varied parameters:

$$|\nu_{0,\alpha+\delta\alpha_i}\rangle = \left(1 + \mathcal{I}(\delta\alpha_i\bar{O}_i)\right)|\nu_{0,\alpha}\rangle + \delta\alpha_i\,|\nu_{i,\alpha}\rangle + \mathcal{O}(\delta\alpha_i^2). \tag{6.13}$$

With this the derivative formally becomes:

$$\frac{\partial E}{\partial\alpha_i} = \lim_{\delta\alpha_i\to 0}\frac{\langle\nu_{0,\alpha+\delta\alpha_i}|\,H\,|\nu_{0,\alpha+\delta\alpha_i}\rangle - \langle\nu_{0,\alpha}|\,H\,|\nu_{0,\alpha}\rangle}{\delta\alpha_i} \tag{6.14}$$

$$= 2\mathcal{R}\left(\frac{\langle\Psi_\alpha|\,H(O_i - \bar{O}_i)\,|\Psi_\alpha\rangle}{||\Psi_\alpha||}\right). \tag{6.15}$$

Using the usual resolution of identity $1 = \sum_s |s\rangle\langle s|$ we are left with:

$$f_i = -2\mathcal{R}\left(\sum_s p(s;\alpha)E^*_{\mathrm{loc}}(s;\alpha)(O_i(s) - \bar{O}_i)\right). \tag{6.16}$$

This is a closed expression for the gradient of a variational energy, which is fully independent from the parameter-structure of the underlying ansatz. In the case of RBMs the O_i can be calculated analytically. This allows one, in principle, to evaluate this expression quite easily numerically. However, the sum in Eq. 6.16, the sum in the local energy in Eq. 5.30, and the normalization of the probability run over all states in state space. This is the aforementioned curse of dimensionality, which for larger systems, renders the expression entirely intractable.

The way around this is to use a *Markov Chain Monte Carlo* approach to draw N random samples from the probability distribution $p(s;\alpha)$. See Sec. 6.4 for an explanation of the algorithm we use. Using this algorithm we have a number of samples which approximate the underlying probability distribution. This allows us to estimate the necessary expectation values in Eq. 6.16 by simply averaging over the samples. The samples are drawn proportional to the underlying distribution. In the limit of $N \to \infty$ the distribution will be reproduced exactly and the method becomes exact. Hence, by increasing the number of samples one can increase the accuracy. This comes at the cost of increasing computation time, however.

$$f_i = -2\mathcal{R}\left(\frac{1}{N}\sum_{n=1}^{N} E^*_{\mathrm{loc}}(s_n;\alpha)(O_i(s_n) - \bar{O}_n)\right) \tag{6.17}$$

$$\bar{O}_i \approx \frac{1}{N}\sum_{n=1}^{N} O_i(s_n) \tag{6.18}$$

Since we are no longer averaging over all possible configurations, but only over a handful of high-probability samples, this derivative is inherently *stochastic* in nature. Hence, why the optimization algorithm is called *Stochastic Gradient Descent*.

6.2 Liouville Density Machines for Open Quantum Systems

6.2.1 Lindbladian Dynamics in Liouville Space

As we have seen in Part I of this thesis, the presence of an external environment fundamentally changes the nature of the dynamics of a quantum system. The state is no longer captured by a wavefunction and the non-unitary dynamics cannot be described by the Schrödinger equation. Instead, the natural description is in terms of a reduced density operator for the system, ρ, and a master equation which defines its time evolution. This then allows for energy dissipation, decoherence and, most importantly for the present manuscript, the relaxation into a non-equilibrium steady-state in the long time limit.

If the coupling to the environment is weak and structureless, one can assume that

system-induced correlations within the bath decay faster than the effects of the bath on the system. This leads to the particularly simple Lindblad master equation of Eq. 2.12. As we have seen the time evolution of the density operator is then governed by the formal expression

$$\rho(t) = \mathrm{e}^{\mathcal{L}t}\rho(0), \tag{6.19}$$

such that in the long time limit the stationary state satisfies

$$\lim_{t\to\infty} \mathcal{L}\rho(t) = 0. \tag{6.20}$$

To simplify what follows both mathematically and numerically we recast Eq. (2.12) in Liouville space (sometimes also referred to as Choi's space). In this space the density matrix is reshaped into a vector,

$$\rho = \sum_m \sum_n \rho_{m,n} \left|m\right\rangle \left\langle n\right| \to \left|\rho\right\rangle\rangle = \sum_{m,n} \rho_{m,n} \left|m,n\right\rangle\rangle. \tag{6.21}$$

Here the density matrix is expanded in the basis $\{|m\rangle\}$ with expansion coefficients $\rho_{m,n}$. The double-ket notation, $|\cdot\rangle\rangle$, used above denotes a vectorized operator which lives in a Hilbert space consisting of two copies of the original, $|\rho\rangle\rangle \in \mathcal{H}\otimes\mathcal{H}$. As we will discuss below, this allows us to cast the Lindblad master equation in a simpler form which allows us to use "simple" linear algebra methods to solve it. Then superoperators which act on these operator-kets are elements of Liouville space $L \in (\mathcal{H}\otimes\mathcal{H})^*\otimes(\mathcal{H}\otimes\mathcal{H})$ [40,169]. Here we often abbreviate the double index (m,n) with a single index s which runs over the ket- and bra-indices of the density matrix $\sum_{m,n}\rho_{m,n}\left|m,n\right\rangle\rangle \equiv \sum_s \rho(s)\left|s\right\rangle\rangle$. With this Eq. (2.12) now reads:

$$\frac{d}{dt}\left|\rho\right\rangle\rangle = L\left|\rho\right\rangle\rangle. \tag{6.22}$$

where

$$L = -i\left(H \otimes \mathbb{1} - \mathbb{1} \otimes H^T\right) \tag{6.23}$$

$$+ \sum_k \left[A_k \otimes A_k^* - \frac{1}{2}\left(\mathbb{1} \otimes (A_k^\dagger A_k)^T + (A_k^\dagger A_k) \otimes \mathbb{1}\right)\right] \tag{6.24}$$

is the matrix form of the superoperator $\mathcal{L}$ that acts from the left on a density-ket, $|\rho\rangle\rangle$. This then allows us to use standard linear algebra results to find the eigenvalues and eigenkets of the matrix L, such that

$$L\,|\rho_i\rangle\rangle = \lambda_i\,|\rho_i\rangle\rangle. \tag{6.25}$$

A stationary state has $\lambda_i = 0$ while all other states have $\mathcal{R}(\lambda_i) < 0$.

As we have seen above, the size of the required Liouville space scales much more quickly than the already exponentially growing Hilbert space. For example, for spin-1/2 lattice problems, the state vector of a closed system grows as $\mathcal{O}(2^N)$, with the system size N. The density matrix, on the other hand, grows as $\mathcal{O}(4^N)$ and hence the Liouvillian has up to $\mathcal{O}(16^N)$ elements which limits the size of accessible systems even further. In the following sections we will detail how we use the NQS approaches outlined above to make progress on these problems.

6.2.2 Finding the Steady State

We will now discuss how we will find the steady-state. Many routes to accessing larger system sizes with numerical simulations are variational methods [77,103]. For example, tensor network methods [19] can be seen as variationally finding the steady-state by optimizing over the set of states captured by a given tensor network architecture, while corner space RG [70] optimizes a particular (small) set of basis states which can be used to build up to larger system sizes, see also Ch. 5 for a more in-depth discussion these methods. As we will see later, neural network techniques make use of the same underlying mathematical structures. Crucial to these methods is the use an ansatz function which specifies the full state with a finite number of parameters, which we denote by α. We may then write $\rho(s;t) \to \rho_\alpha(s;t)$ and optimize over α, to find the

closest representation of the steady-state within this class. For this approach to be an efficient solution, the number of parameters must grow at most polynomially with the system size.

To find the steady-state, $\lim_{t\to\infty}\rho(t) \equiv \rho_{ss}$, we require a cost function which measures how close the ansatz is to the true stationary density operator. To do this we make use of the fact that $L\,|\rho_{ss}\rangle\rangle = 0$ and that for all other states this quantity is finite. This gives us a cost function to optimize as well as a metric for how well the variational state parametrizes the true steady-state. The cost function we wish to optimize is given by the quantity

$$|\mathrm{C}_\alpha|^2 = \left|\frac{\langle\langle\rho_\alpha|L|\rho_\alpha\rangle\rangle}{\langle\langle\rho_\alpha|\rho_\alpha\rangle\rangle}\right|^2, \tag{6.26}$$

this uniquely vanishes in the steady-state. Note that the vectors appearing above are in Liouville space, hence the denominator involves the sum over all elements of the density matrix $\langle\langle\rho_\alpha|\rho_\alpha\rangle\rangle = \sum_s |\rho_\alpha(s)|^2$. Expanding this cost function yields a form that can easily evaluated via Markov chain Monte Carlo

$$\begin{aligned} C_\alpha &= \frac{\langle\langle\rho_\alpha|L|\rho_\alpha\rangle\rangle}{\langle\langle\rho_\alpha|\rho_\alpha\rangle\rangle} && (6.27)\\ &= \frac{1}{\sum_{s'}|\rho_\alpha(s')|^2}\sum_{s,s'}\rho_\alpha^*(s)\rho_\alpha(s')\langle\langle s|L|s'\rangle\rangle && (6.28)\\ &= \frac{1}{\sum_{s'}|\rho_\alpha(s')|^2}\sum_{s,s'}\frac{|\rho_\alpha(s)|^2\rho_\alpha(s')}{\rho_\alpha(s)}\langle\langle s|L|s'\rangle\rangle && (6.29)\\ &= \sum_s p(s;\alpha)C_{\mathrm{loc}}(s;\alpha), && (6.30) \end{aligned}$$

where

$$p(s;\alpha) = \frac{|\rho_\alpha(s)|^2}{\sum_{s'}|\rho_\alpha(s')|^2}, \tag{6.31}$$

defines a probability distribution over the entire density matrix which we can draw samples from. The local cost associated to each element of this distribution is then

$$C_{\mathrm{loc}}(s;\alpha) = \sum_{s'} \langle\langle s|L|s'\rangle\rangle \frac{\rho_\alpha(s')}{\rho_\alpha(s)}. \tag{6.32}$$

Here we split the cost function into a probability distribution as well as a "local cost" in a similar fashion to the groundstate example above. The states s' which connect via the matrix element of the Liouvillian to the original state s are generated during the Metropolis-Hastings step and can be accessed at any later stage of the process, see Sec. 6.4 for details on the algorithm used. Since, for a local Liouvillian, the number of non-zero elements grows only polynomially in system size, the evaluation of the matrix elements of L can also be done efficiently. The samples we draw follow the distribution $p(s;\alpha)$, and so the cost can be calculated as a simple mean over the local costs [16]

$$C_\alpha \approx \frac{1}{N_s} \sum_s C_{\mathrm{loc}}(s;\alpha), \tag{6.33}$$

where N_s is the number of samples and the sum runs over the Monte Carlo samples.

Along with an estimate for the cost function we also need a way of updating the parameters, α such that the state we find is optimised. The simplest way to do this is via stochastic gradient descent (SGD), where the gradients of C_α are also estimated with the Monte Carlo samples and at each step in the simulation the parameters are updated according to Eq. 6.3. There are several problems with this approach, e.g. it has been shown [171] that SGD has severe problems with steep energy surfaces. The main problem for the present case is that L also has a left eigenstate with eigenvalue 0,

$$\langle\langle \mathbb{T}| \, L = 0. \tag{6.34}$$

This is the trace-state which is defined as

$$\langle\langle \mathbb{T}|\rho\rangle\rangle = \mathrm{Tr}\left[\rho\right], \tag{6.35}$$

and since the dynamics of any physical master equation is necessarily trace preserving we find the result above. This means that there is another state which optimizes

the cost function. A solution to both of these problems is to instead use Stochastic Reconfiguration (SR) [16, 171] to update the parameters.

6.3 Stochastic Reconfiguration

The stochastic reconfiguration can be derived by asking which parameter update γ,

$$\alpha \to \alpha' = \alpha + \eta\gamma, \tag{6.36}$$

best approximates a step in real time. Here, η is the learning rate we have used before in SGD and γ is the vector which contains the individual parameter updates. Since the trace state cannot be found by a real-time evolution generated by L this guarantees that we will find the correct steady-state when optimizing the cost, Eq. (6.26). Furthermore, SR takes into account the curvature of the energy landscape, speeding up the optimization on flat areas and slowing down in the presence of strong curvature. The derivation of the SR update in this section is based on the ones found in Refs. [16, 171, 172]. We recommend especially [16] for various additional ways of deriving SR and Ref. [171] for an in-depth discussion of the properties of the quantum Fisher matrix which plays an important role in SR.

Consider an ansatz function $|\rho_\alpha\rangle$ with variational parameters α. For the derivation, we assume that the ansatz is normalised: $||\rho_\alpha||^2 = \langle\rho_\alpha|\rho_\alpha\rangle = 1$. We can use this to define a semi-orthogonal basis consisting of $|\rho_{i=0,\alpha}\rangle = |\rho_\alpha\rangle$, the ansatz function, as well as its derivatives

$$|\rho_{i,\alpha}\rangle = (O_i - \langle O_i\rangle)\,|\rho_{0,\alpha}\rangle\,, \tag{6.37}$$

where $\langle O_i\rangle = \langle\rho_{0,\alpha}|\,O_i\,|\rho_{0,\alpha}\rangle$ and O_i is the logarithmic derivative operator $O_i(s) = \frac{1}{\rho_\alpha(s)}\frac{\partial}{\partial_{\alpha_i}}\rho_\alpha(s)$. A variation by a small parameter shift γ then yields:

$$|\rho_{\alpha+\gamma}\rangle \approx \sum_{i=0}^{N_p} \gamma_i\,|\rho_{i,\alpha}\rangle\,, \tag{6.38}$$

where N_p runs over all parameters and γ_i is the update to the ith parameter. Let us now suppose we are given some Liouvillian L, then real-time evolution over some small time-step δt is given by $\mathrm{e}^{-\delta t L}\left|\rho_\alpha\right\rangle$. Expanding this around a small time-step yields

$$\mathrm{e}^{-\delta t L}\left|\rho_{0,\alpha}\right\rangle \approx (1-\delta t L)\left|\rho_{0,\alpha}\right\rangle . \tag{6.39}$$

We now have:

$$\left|\rho_{\alpha+\gamma}\right\rangle \approx \sum_{i=0}^{N_p} \gamma_i \left|\rho_{i,\alpha}\right\rangle \tag{6.40}$$

$$\left|\tilde{\rho}_{0,\alpha}\right\rangle \approx (1-\delta t L)\left|\rho_{0,\alpha}\right\rangle . \tag{6.41}$$

The idea is now to project both sides into the non-orthogonal basis and ask, under which conditions they become equal [172]:

$$\langle\rho_{i,\alpha}|\tilde{\rho}_{0,\alpha}\rangle = \langle\rho_{i,\alpha}|\rho_{\alpha+\gamma}\rangle \tag{6.42}$$

$$\Rightarrow \langle\rho_{i,\alpha}|(1-\delta t L)\left|\rho_{0,\alpha}\right\rangle = \langle\rho_{i,\alpha}|\sum_{j=0}^{N_p}\gamma_j\left|\rho_{j,\alpha}\right\rangle \tag{6.43}$$

$$\Rightarrow -\delta t\langle\rho_{i,\alpha}|L\left|\rho_{0,\alpha}\right\rangle = \sum_{j=1}^{N_p}\gamma_j\langle\rho_{i,\alpha}|\rho_{j,\alpha}\rangle \tag{6.44}$$

$$\tag{6.45}$$

The left-hand side now reads

$$-\delta t\langle\rho_{0,\alpha}|(O_i^* - \langle O_i^*\rangle)L\left|\rho_{0,\alpha}\right\rangle = -\delta t(\langle O_i^* L\rangle - \langle O_i^*\rangle\langle L\rangle), \tag{6.46}$$

while the right-hand side reads

$$\sum_{j=1}^{N_p} \gamma_j \langle \rho_{0,\alpha} | (O_i^* - \langle O_i^* \rangle)(O_j - \langle O_j \rangle) \rho_{0,\alpha} \rangle \tag{6.47}$$

$$\sum_{j=1}^{N_p} \gamma_j (\langle O_i^* O_j \rangle - \langle O_i^* \rangle \langle O_j \rangle) \tag{6.48}$$

Equating both sides yields:

$$-\delta t (\langle O_i^* L \rangle - \langle O_i^* \rangle \langle L \rangle) = \sum_{j=1}^{N_p} \gamma_j (\langle O_i^* O_j \rangle - \langle O_i^* \rangle \langle O_j \rangle). \tag{6.49}$$

Identifying the forces $f_i = \langle O_i^* L \rangle - \langle O_i^* \rangle \langle L \rangle$ and the quantum Fisher matrix $S_{i,j} = \langle O_i^* O_j \rangle - \langle O_i^* \rangle \langle O_j \rangle$ we can write this more succinctly

$$-\delta t f = S\gamma, \tag{6.50}$$

where we identify the learning rate $\eta = \delta t$. The solution of this system of linear equations γ are the parameter updates which most closely resemble a step in real-time of size δt. The matrix S is defined to be positive, however when estimating it via Monte Carlo sampling, it can happen that some eigenvalues vanish and S becomes singular. One can work around this problem by either calculating the pseudo-inverse or adding a small regularization, $\lambda \approx 10^{-3}$, to the diagonal. We employ the latter method here. With this the parameter update becomes

$$\gamma = -\delta t \left(S + \lambda\right)^{-1} f. \tag{6.51}$$

As discussed, updating the parameters like this will guarantee that we find the correct steady state in the long time limit, which also fixes any possible issues arising from local minima. The Fisher matrix can be regarded as something akin to a metric tensor, see Ref. [171], which contains information of the curvature of the cost landscape. Dividing by its inverse as the effect of accelerating the learning in flat areas, where other solvers might get stuck as well as treading more carefully in the vicinity of large curvature, where other solvers might overshoot.

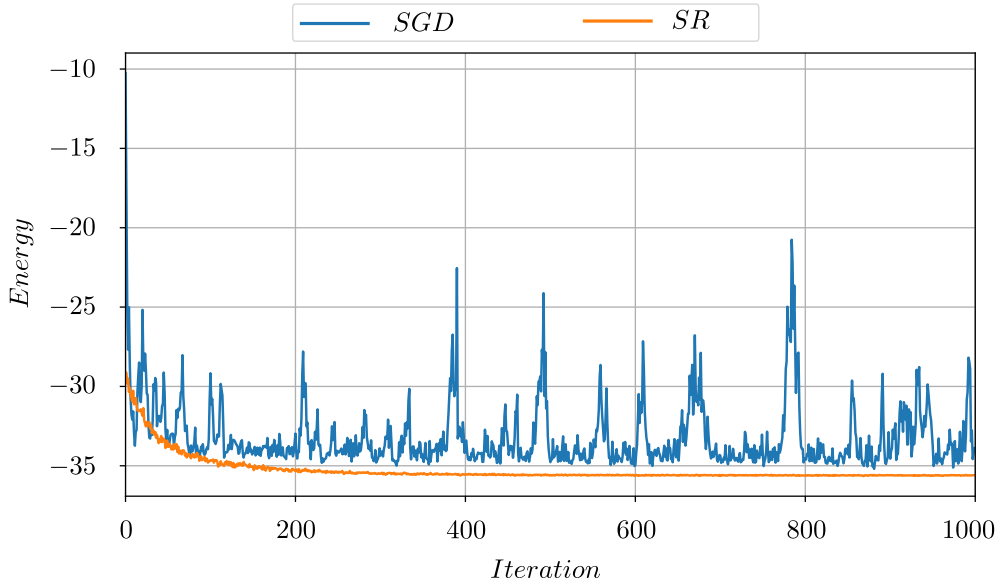

Figure 6.1: The plot shows the convergence behaviour of SGD and SR towards the groundstate energy of a 1D Heisenberg model with 20 sites. The learning rate was chosen to be $\eta = 0.001$, while the diagonal shift of the SR was chosen to be $\lambda = 0.1$, see Sec. 6.3 for an introduction to Stochastic Reconfiguration.

For an example convergence plot see Fig. 6.1. It shows the convergence towards the groundstate energy of a 20 site 1D-Heisenberg model with $J = 1$. It compares SGD with the SR. We choose a symmetrized RBM as implemented in NetKet [164]. We see that while SGD does get close to the minimum reached by SR, the convergence is much less stable. This is one of the reasons why we use the SR algorithm for this kind of optimisation problem.

6.4 Markov Chain Monte Carlo Sampling

In the previous section we have discussed a powerful extension of the SGD, which will allow us to reliably find the correct steady-state. Similar to SGD, stochastic reconfiguration requires expectation values which in turn require sums over an exponentially fast growing state space. In this section we will discuss a way of mitigating this issue.

Since the size of the required state space grows exponentially fast with the system

size, it quickly becomes impossible to calculate expectation values and gradients exactly. This requires us to draw sample states from the total space in a way that follows the true probability distribution parametrized by the variational ansatz.

The algorithm we employ to generate the samples is the Metropolis-Hastings algorithm. It can be used to draw samples from an unknown distribution, as long as we have a function which is at least proportional to that distribution. We achieve this by realizing that the relative probability of two configurations, $p(s')/p(s)$, is independent of the exact normalization of the distribution. This means, that if $p(s')/p(s) > 1$, the we know immediately that $p(s') > p(s)$, i.e. s' has a higher probability. We can use this to iteratively generate a new sample from a previous one, by flipping a spin, for example. In this way a Markov Chain of samples is created that can be used to estimate expectations and gradients.

In the following paragraphs we will discuss the algorithm in a bit more detail. We will do so for a spin-1/2 groundstate model for the sake of simplicity. Everything generalises to larger local dimensions without issue. Let $\Psi_\alpha(x)$ be the function that is proportional to the desired distribution $|\Psi_\alpha|^2$. Further, let $Q(x|y) = Q(y|x)$ be the symmetric, conditional probability that determines the jumps. In the literature this is often referred to as the *trial probability*. Note, that we will never use an explicit expression for $Q(x|y)$. In case of flipping one random spin, the probability to flip any spin is always $1/N$ independent of the current configuration. Hence, $Q(x|y) = Q(y|x)$ is trivially fulfilled.

Generating a new sample We begin with discussing again how a sample is generated and what is ultimately added to the chain. Suppose we are given a configuration s of N spins. In the Z-basis this is an array of $0's$ and $1's$ denoting the up- and down-state of each spin respectively. The first step will be to randomly determine one of those spins as the one to flip. In a next step we compare the probabilities of the two configurations. If the new one is more probable, we will always accept it. Otherwise, we accept it with a probability equal to the ratio. If the new configuration is rejected, we add the old configuration to the chain again.

1: **function** GENERATESAMPLE $(\Psi_\alpha(), s)$
2: $L = \text{len}(s)$
3: $i = \text{randint}((1, L))$
4: $s' = \text{copy}(s)$
5: $s'[i] = (s'[i] + 1)\%2$
6: **if** $\text{random}(0, 1) < abs\left(\frac{\Psi_\alpha(s')}{\Psi_\alpha(s)}\right)^2$ **then**
7: **return** $s',\ \Psi_\alpha(s')$
8: **else**
9: **return** $s,\ \Psi_\alpha(s)$
10: **end if**
11: **end function**.

Initial Sample, Burn In and Sweeps We will now discuss how to initialize the Markov chain. A possibility is to generate some random configuration. An issue with this is that a randomly chosen initial configuration is unlikely to lie within the equilibrium probability distribution of the Markov process. This may add some finite weight to configuration which would otherwise not be part of the equilibrium distribution. The solutions is a so called *burn-in*. One generates a number of samples using the above procedure and keeps the last as the initial configuration for the Markov chain. Sometimes, this process is also called a sweep. The idea behind this is that any Markov process which fulfils ergodicity and detailed balance will necessarily thermalize after a number of steps and only samples with a finite weight are left.

1: **function** SWEEP $(\Psi_\alpha(), Nb, s)$
2: **for** $i = 1$ to Nb **do**
3: $s,\ p = \text{GenerateSample}(\Psi_\alpha(), s)$
4: **end for**
5: **return** $s,\ p$
6: **end function**.

A further issue with the Markov Chain Monte Carlo algorithm is that neighbouring samples aren't independent from one another and the chain is strongly autocorrelated.

This has the effect of skewing the estimated probability distribution and all derived expectation values. Luckily, the *correlation time* and the *thermalization time* coincide, see Ch. 3.8 of Ref. [16]. Hence, one can simply generate Nb samples at each step and only add the last one to the chain.

Markov Chain Monte Carlo With this we have all the necessary ingredients for the full algorithm. We begin by generating a random configuration. As discussed this is very likely to be a vanishing-weight configuration, so we perform a burn-in. This yields a configuration which lies somewhere in the equilibrium distribution of the Markov chain, i.e has a finite contribution to the state parametrized by α. We add this as the first configuration to the Markov Chain, and save the state in a separate one. Both the configurations and states can then later be used to calculate expectation values and gradients. We then repeat the process for N_s times.

1: **function** MCMC $(\Psi_\alpha(), L, Ns, Nb)$
2: $s0 = \text{randint}((0,1), \text{size} = L)$
3: $\text{ConfigChain} = \text{array}((Ns, L))$ ▷ Stores the Configurations
4: $\text{StateChain} = \text{array}(Ns)$ ▷ Stores the States
5: $\text{ConfigChain}[1,:],\ \text{StateChain}[1] = \text{Sweep}(\Psi_\alpha(), Nb, s0)$
6: **for** $i = 2$ to Ns **do**
7: $\text{ConfigChain}[i,:],\ \text{StateChain}[i] = \text{Sweep}(\Psi_\alpha(), Nb, \text{ConfigChain}[i-1,:])$
8: **end for**
9: **return** ConfigChain, StateChain
10: **end function**.

In this chapter we discussed RBMs and how they can be used as neural quantum states. We introduced the basics of the Wirtinger calculus as a means to deal with complex-valued networks. We further introduced the *Liouville Density Machines* ansatz for the stead-states of open quantum systems. We further discussed possible issue that may arise on the way towards the steady-state and how to mitigate them via *Stochastic Reconfiguration*. Finally, we discussed *Markov Chain Monte Carlo* sampling and its pitfalls.

In Ch. 7 we will see how this machinery performs when compared to the *Quantum Trajectories* method introduced in Ch. 3, *Matrix Product States* as well as the *Neural Density Machines* we have discussed in Ch. 5.

Chapter 7

Results

In Ch. 5 we discussed the theoretical context of our methods and how it fits in between tensor network based methods and other neural quantum state based methods. In Ch. 6 we then proposed a novel ansatz to represent the steady-state of open quantum systems as well as how to optimize it. The proposed LDMs are highly compact representations of *non-equilibrium steady states* (NESS). They make full use of the volume-law correlation capacity of RBMs without having to sacrifice capacity to represent mixedness, see Ch. 5.

In this chapter we wish to investigate the convergence properties of LDMs as well as benchmark them against various other methods. We will begin with the transverse-field Ising model with longitudinal dissipation of Eq. 7.1 for different system sizes in Sec. 7.1. For this model we will also investigate how the state approaches physicality, i.e. how the positivity and hermiticity evolve as the optimisation progresses. In Sec. 7.2 we will look at a transverse-field Ising model with transverse dissipation, i.e. the Hamiltonian has been rotated around the Y-axis, while the original dissipation has remained invariant. This has the effect that the dissipation no longer breaks the $\mathbb{Z}_2$-symmetry of the Hamiltonian, which suggests that it is possible that the model undergoes a second-order phase transition in the thermodynamic limit. This naturally leads to an increased correlation content in the states, which makes it much more difficult, albeit more interesting, than the original model. To better understand the performance of our ansatz we compare it with MPS and *Neural Density Machines* (NDMs) at each step. Finally, in Sec. 7.3 we will have a brief look at the total information content of the steady states of each model.

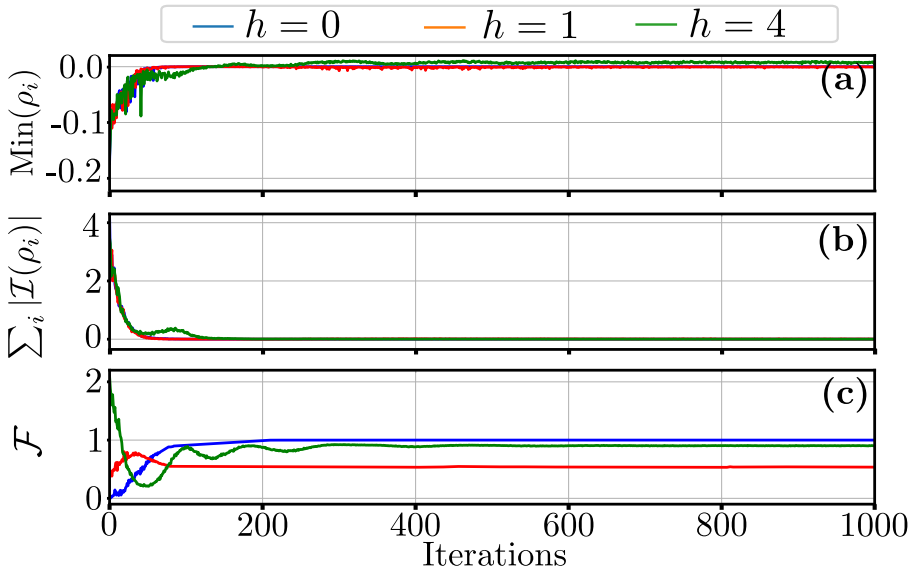

Figure 7.1: Properties of the state obtained by using SR at three different values of h and $J/\gamma = 2$. We used 4500 samples, a learning rate of $\eta = 10^{-2}$ and a regularization of $\lambda = 10^{-2}$. Panel (a) shows the real part of the minimum eigenvalue of the full density matrix obtained from the LDM. In (b) we show the sum of the absolute value of the imaginary parts of the eigenvalues of the density matrix. Panel (c) gives the fidelity of the ansatz with the exact density matrix.

To this end we will look at the purity as a stand in for the von Neumann entropy as well as the negativity as a measure for the entanglement content. Large parts of this chapter, including figures, captions and text are taken without explicit citation from our own paper [5].

7.1 Transverse Field Ising Model

To benchmark and understand the strengths and limitations of the LDM ansatz we study the stationary state of the 1D dissipative transverse-field Ising (TFI) model [10, 21, 51, 153, 169, 173]. The system consists of a chain of spin-1/2 particles. The Hamiltonian part of the evolution is governed by

$$H = \frac{J}{4}\sum_{i}^{N-1}\sigma_i^z\sigma_{i+1}^z + \frac{h}{2}\sum_{i}^{N}\sigma_i^x. \tag{7.1}$$

Here, N is the number of sites, σ are the usual Pauli matrices, J is the interaction strength and h is the strength of the transverse field. The dissipation is governed by excitation loss on each site, so the jump operators which appear in the Liouvillian of Eq. 2.12 are $A_i = \sigma_i^-$. We choose the units of the interaction and field such that the dissipation strength is $\gamma = 1$. In all calculations that follow we set the interaction strength to $J/\gamma = 2$ to be able to compare with the results from Ref. [21].

The steady-state of this model then has simple solutions in two limiting cases. When $h \to 0$ the dissipation dominates the dynamics and the stationary state is a pure product-state with all the spins pointing down

$$\lim_{h\to 0} \rho_{ss} = \bigotimes^{N} |\downarrow\rangle \langle\downarrow| . \tag{7.2}$$

This follows easily from the commutation of ρ_{ss} with the Hamiltonian and the fact that $\sigma^- |\downarrow\rangle = 0$, i.e. the steady-state is the dark state of the dissipators. In the opposite limit where $h \to \infty$ there is only competition between the local onsite field and the dissipation and so the steady-state ends up again as a product-state, but this time the state on each site is mixed

$$\lim_{h\to \infty} \rho_{ss} = \bigotimes^{N} \frac{1}{2} \left(|\uparrow\rangle \langle\uparrow| + |\downarrow\rangle \langle\downarrow| \right) . \tag{7.3}$$

At intermediate values of h the steady-state interpolates between these two, building up complex long range classical and quantum correlations.

To test that the state we obtain is physical, we construct the full density matrix from the LDM. In the top panel of Fig. 7.1 we show how the real part of the smallest eigenvalue of this constructed density matrix evolves. For a randomly initiated state the minimum eigenvalue is negative, which indicates a non-physical density matrix. However, as the optimisation goes on the minimum eigenvalues become closer to 0 or positive, indicating that the final density matrix is positive semi-definite.

The middle panel of this figure shows the imaginary parts of all eigenvalues. They are quickly suppressed as the stochastic reconfiguration leads the ansatz towards the true steady-state. This, together with the positive-semi-definiteness of the ansatz in

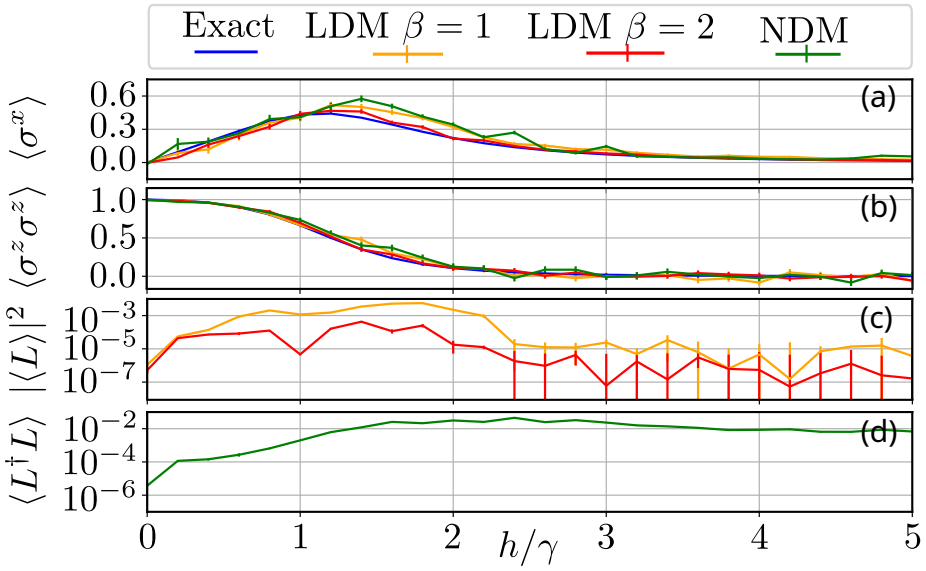

Figure 7.2: Comparison of the steady-state of Eq. (7.1) using both the NDM and LDM approaches. The system size, $N = 6$, is small enough that exact diagonalization is possible. (a) The expectation value of σ_i^x as a function of h. (b) The expectation value of the $\sigma_i^z \sigma_{i+1}^z$ correlation function. In both cases the expectation value is taken on the central site(s). The blue lines show the exact result, the NDM with $\beta = 1$ is green, the LDM with $\beta = 1(2)$ is orange (red). (c) The absolute value squared of the cost function in Eq. 6.26 for the two LDM results. (d) The expectation value $\langle L^\dagger L \rangle$ used as a cost function for the NDM ansatz employed by NetKet. For both cases with $\beta = 1$ we used 4500 samples and optimized for 1000 steps with a learning rate of $\eta = 10^{-2}$ and a regularization of $\lambda = 10^{-2}$, for the expectation values we used 500 diagonal samples. In the $\beta = 2$ case we used 6000 samples and 2000 steps and 800 diagonal samples. The other meta parameters were the same in both cases.

the steady-state, shows that we are able to reach the physical NESS of the system. In Fig. 7.1(c) we compare the fidelity of the ansatz with the exact steady-state. We see that, as we will see in the results of Fig. 7.2, the fidelity is highest in the cases where the transverse field strength is either very large or very small and the fidelity is lowest where the steady state has large entanglement around $h = \gamma$. A fidelity $\mathcal{F} > 1$ can be explained with the imaginary parts of the eigenvalues.

We will now compare the results of the LDM ansatz to those obtained using the NDM approach as implemented in the NetKet library [164]. For small system sizes we will also be able to compare to results obtained from exact diagonalization, these are calculated using QuTIP [174]. As a first example we look at the case of a small

system with $N = 6$. Our findings are summarised in Fig. 7.2. In each case we randomly initialise the parameter values and at each step we take Monte Carlo samples to approximate the cost function

$$|\mathrm{C}(\alpha)|^2 = \left| \frac{\langle\langle \rho_\alpha | L | \rho_\alpha \rangle\rangle}{\langle\langle \rho_\alpha | \rho_\alpha \rangle\rangle} \right|^2 , \tag{7.4}$$

and the best updates to the parameters. At the end of each run we produce a new Markov chain, but this time sample from a probability distribution which follows the diagonal of the density matrix. This allows us to estimate the expectation value of observables of interest. Since there are fewer diagonal states than entries in the full density matrix we usually only need about 500-800 diagonal samples.

In panels (a)–(b) of Fig. 7.2 we show the expectation value of σ_i^x on the central site and the $\sigma_i^z \sigma_{i+1}^z$ correlation function on the central pair of sites as a function of the field strength, h. This gives a good indication of how well the various approaches are able to produce single site observables. We see that, in general, there is good agreement between the exact results and those obtained using both the LDM and NDM approaches. In all cases the agreement is worst in the central region where $1 \leq h/\gamma \leq 2.5$, which is in agreement with the results of Ref. [21]. For the LDM a hidden unit density of $\beta = 1$ corresponds to 132 parameters for the NDM this is 174 parameters. We see that even with only 3/4 of the parameters the LDM generally gives as good or better results than the NDM. By increasing the number of hidden units in the LDM we also increase the number of parameters so that, at $\beta = 2$, there are 246 parameters. We see that for the LDM ansatz increasing the value of β and hence the number of parameters used is able to significantly decrease the deviation from the exact result, thus we may use the hidden unit density as a way of checking for convergence when exact results are no longer possible. We can also see this effect more clearly in Fig. 7.2(c) and (d) where we show the Monte Carlo estimated cost function for each ansatz. The value of the cost function is significantly decreased at all values of h when β is increased. We also see that for the LDM ansatz the cost function is at a maximum in the regions where the convergence to the steady-state is worst, this allows us to use this estimate to again judge the accuracy of our results for system sizes where exact

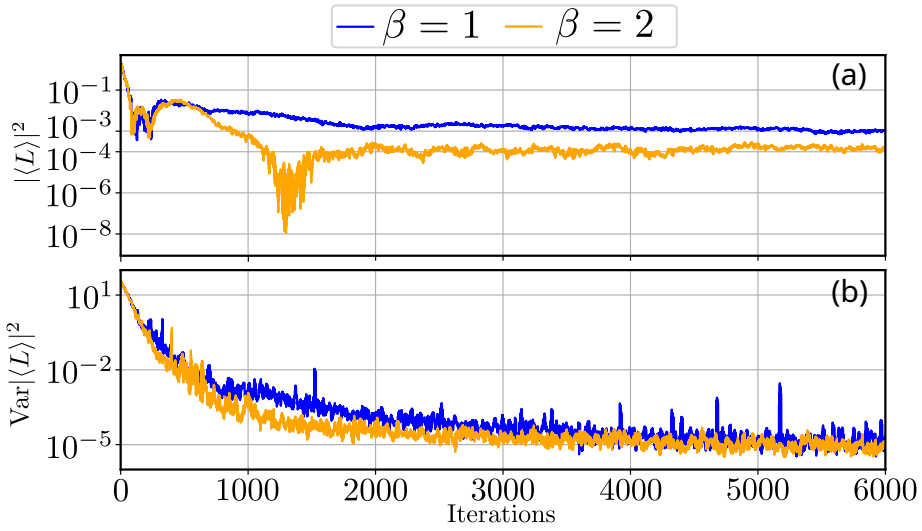

Figure 7.3: Convergence of the LDM ansatz for two different hidden unit densities. Panel (a) shows the running estimate for the cost function while panel (b) is the variance in the same quantity. Increasing the hidden unit density improves the accuracy of the results. Both calculations were done at $h/\gamma = 1$ using the same parameters as Fig. 7.2.

methods are unavailable. This is not true of the NDM approach where the cost function reaches a maximum at intermediate values of h and does not significantly decrease as h increases further. The ill convergence of the NDM is because the mixed product state, described in Eq. (7.3), is not so easy to represent in a purification ansatz. Such a mixed state requires a large amount of entanglement between the real and auxiliary spins. The LDM approach on the other hand can represent this state exactly without using hidden units, which makes convergence easier.

In Fig. 7.3 we show how the cost function of the LDM evolves for two different values of β over 6000 steps at one of the most difficult points, $h = \gamma$. By increasing the number of variational parameters from 132 to 246 we were able to reduce the cost function by an order of magnitude. We also see that simply checking the value of the cost function does not give an accurate stopping condition for the algorithm. After around 1400 steps the cost function for $\beta = 2$ is very small but the variance is quite large. This means that the LDM has not found an eigenstate of the Liouvillian but is still giving a small value for the cost function. We propose that a condition based on a combination of both of these quantities can give a good way to automatically stop the

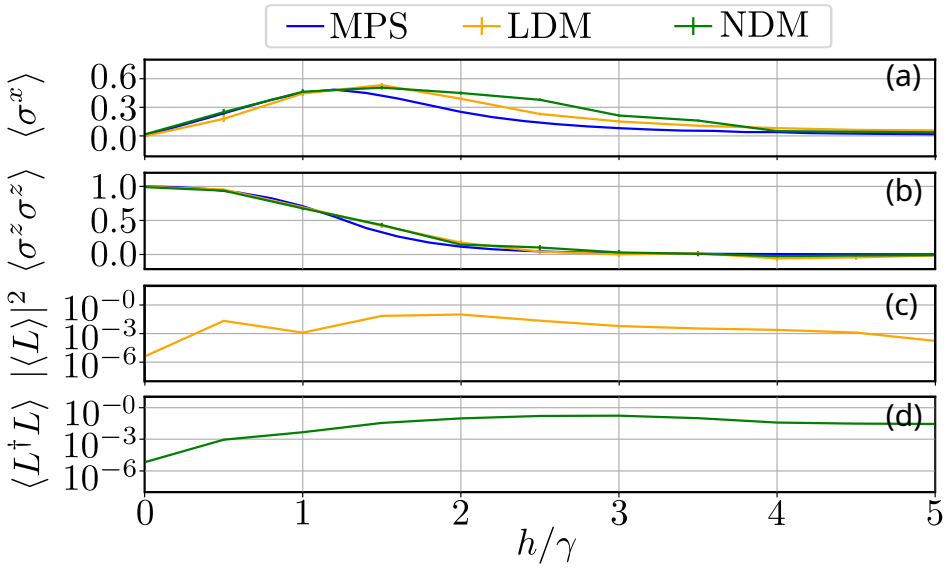

Figure 7.4: Steady-state of Eq. (7.1) as a function of field strength for a system size $N = 16$. The expectation value of σ_i^x and $\sigma_i^z \sigma_{i+1}^z$ on the central site(s) are shown in panels (a)–(b) and the relevant cost functions in panels (c)–(d). Results are compared to those obtained from MPS simulations.

learning process when a good approximation to the steady-state has been reached.

We now go on to examine how the accuracy of these approaches scales to larger system sizes. At $N = 16$ it becomes difficult to use exact methods to compare against, however this model is straightforward to solve with MPS simulations which we found to be fully converged for a bond-dimension of $\chi = 7$. Results of these calculations are shown in Fig. 7.4. We used $\beta = 1.4$ in the case of LDM and $\beta = 1$ for the NDM to ensure that both approaches use a similar number of parameters. The NDM has 1104 parameters, while the LDM has 1126. For reference, a bond dimension of $\chi = 7$ corresponds to 1952 matrix elements in the MPS. We evolved for 7000 steps with a learning rate of $\eta = 10^{-3}$ and a regularization of $\lambda = 3 \times 10^{-3}$. We used 9000 samples as well as 800 diagonal samples to estimate the expectation values. We see very similar behaviour to the $N = 6$ case, both approaches are more difficult to converge in the region of intermediate h/γ and the cost function for the LDM has a peak in this region. In Fig. 7.5 we show how the convergence can again be improved by increasing the hidden unit density. Here we choose $h = 2\gamma$ as this is the point where the convergence

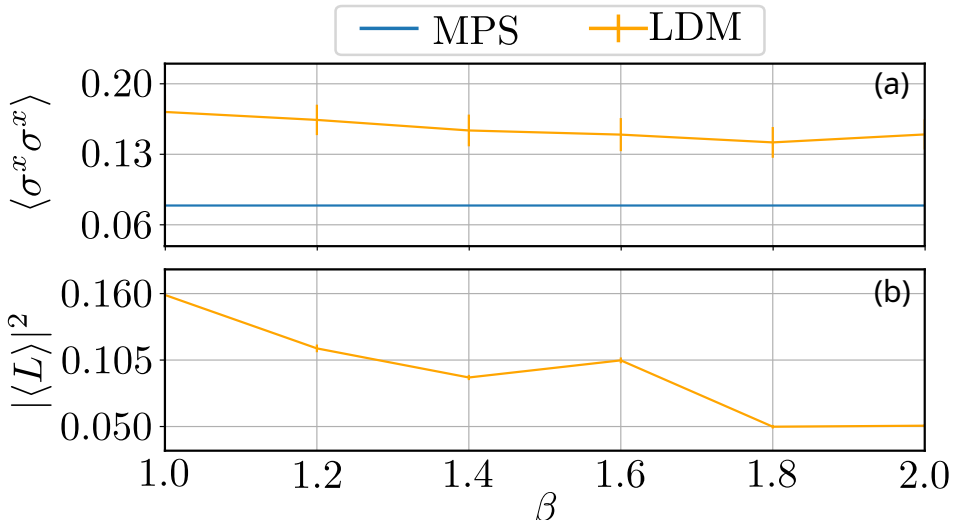

Figure 7.5: Improvement of convergence as a function of β for the $N = 16$ TFI model at $h = 2\gamma$. In (a) we show the $\sigma_i^x \sigma_{i+1}^x$ correlation function and in panel (b) the estimate for the cost function. All calculations ran for 7000 steps. To accommodate for higher parameter counts we increased the number of samples with β from 9000 at $\beta = 1$ to 17000 at $\beta = 2$. Other parameters are the same as in Fig. 7.4.

is worst. We see that as β is increased the cost function decreases towards zero and the expectation value moves towards that found in the MPS simulation. The expectation value here is a two-point correlation function which, in general, are harder to converge than single-site operators.

In this section we saw that, while the LDM ansatz forgoes explicit physicality constraints throughout its optimisation, the use of Stochastic Reconfiguration enforces the correct, physical steady-state. We also benchmarked the LDM ansatz vs NDM and MPS in the context of the transverse-field Ising model with longitudinal dissipation. We found that it presents an improvement over the NDM ansatz, in particular in the intermediate regime of $1 \leq h/\gamma \leq 2.5$. This improvement becomes more pronounced as the number of sites increases.

7.2 Rotated TFI

We will now move on to the the *rotated* transverse-field Ising model. As discussed above, we reach this model by rotating the Hamiltonian around the Y-axis, while keeping the

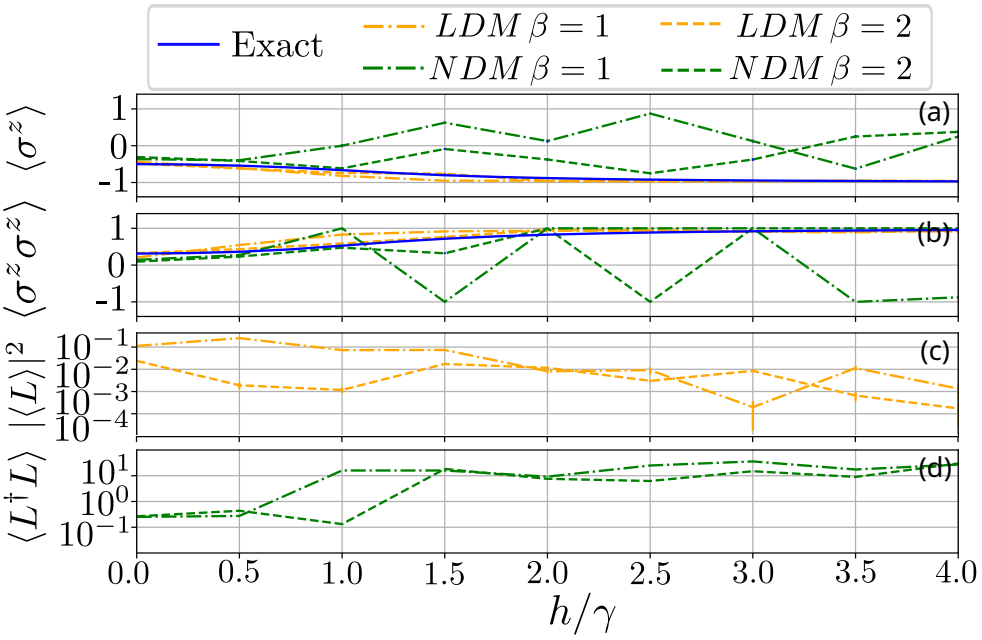

Figure 7.6: Optimizing the rotated TFI model as in Eq. 7.5 for $N = 6$. The exact results are in blue, those obtained with the LDM are orange and the NDM in green. Different hidden unit densities are shown by different line-styles. In panel (a) we give the steady-state expectation value of σ_i^z and in (b) we show the two-point correlation function $\langle \sigma_i^z \sigma_{i+1}^z \rangle$. Panels (c) and (d) show the relevant cost functions for each ansatz.

dissipation fixed [10, 173, 175]

$$H = \frac{J}{4} \sum_{i=0}^{N-1} \sigma_i^x \sigma_{i+1}^x + \frac{h}{2} \sum_{i=0}^{N} \sigma_i^z. \tag{7.5}$$

This has the result of making the convergence of both neural network approaches considerably worse. In this case the dissipation does not explicitly break the $\mathbb{Z}_2$ symmetry of the model as the interaction term is perpendicular to the dissipation. Therefore the competition between the coherent and dissipative dynamics gives rise to complex correlations in the steady-state. This leads to a very rich mean-field phase diagram in high dimensions with possibilities for both first- and second-order phase transitions between different magnetic orderings [51, 175, 176]. In 1D these phase transitions turn into continuous crossovers, but complex correlations still build up when $h \sim J \sim \gamma$. For a detailed review of the behaviour of this model in 1D see Ref. [10].

In the last section we saw that the ansatz converges towards a physical state and can be improved by increasing the number of parameters. We will therefore focus our attention on the convergence of both the LDM and NDM approaches towards the steady-state of this model. As we will see, obtaining convergence is much more difficult for either ansatz and requires a higher degree of optimisation. We will therefore restrict ourselves to a system size of $N = 6$. While small, this is sufficient to see the overall differences in capabilities of the two ansatze. The results of our investigations are shown in Fig. 7.6 for $N = 6$ sites. In all cases the optimisation was run for 4000 steps, with a learning rate of $\eta = 10^{-3}$ and 2000 diagonal samples to estimate the expectation values. For $\beta = 1$ we used 4500 samples and a regularization of $\lambda = 10^{-3}$. For $\beta = 2$ the number of samples was increased to 18000 and the regularization was 10^{-2}.

In panels (a) and (b) of Fig. 7.6 we show how both a single site and two-site observables varies with the applied field h. We see that even when using a large amount of samples and parameters, the NDM ansatz is not able to find a good approximation to the exact result, while the LDM is able to get much closer to the expected result, especially at small and large values of h. We see that for both approaches the cost function estimate is much larger than it was for the simpler model described by Eq. (7.1). This is because the steady-state in this case has much more complex correlations than in the previous model, simple expressions like those in Eqs. (7.2)–(7.3) are not available, except at very large $h \to \infty$ where the steady-state is the same as given in Eq. (7.2). We next go on to show how using measures of the entanglement found in the steady-state can give good intuition for when these kinds of difficulties arise.

7.3 Entanglement Properties

One of the main reasons for the development of the LDM ansatz was the lack of a thorough understanding of what class of states the NDM were well suited to represent. From [10] we know that MPS are capable of representing the steady-state of Eq. 7.5 with a bond dimension of $\chi = 20$ for $N = 40$. This suggests that a very compact representation is possible. During preliminary investigations we found, however, that NDM are incapable of representing the steady-states of this model efficiently. To

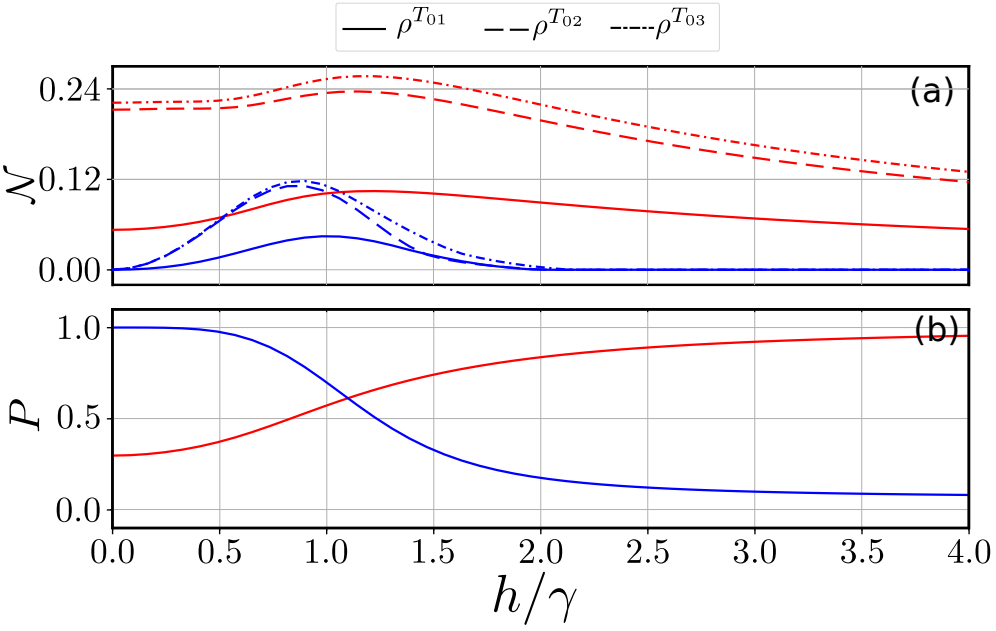

Figure 7.7: (a) The steady-state entanglement negativity, defined in Eq. (7.6) and (b) purity, $P = \mathrm{Tr}[\rho^2]$, for the $\sigma^x\sigma^x$-model (red) and the $\sigma^z\sigma^z$-model (blue). Comparing with the results of Figs. 7.2 and 7.6 we observe a correlation between a large negativity and poor accuracy of the neural network.

further understand which classes of models the ansatze are well suited to represent, we will investigate the entanglement present in the steady-states of both models over a range of parameters. Contrary to pure states, quantifying the amount of correlations that are present in a mixed state isn't as simple as just calculating the entanglement entropy between two halves of the system [177]. For our purposes we find that the negativity [178, 179]

$$\mathcal{N} = \frac{||\rho^{T_A}|| - 1}{2}, \tag{7.6}$$

provides a useful measure of the correlations which are difficult to represent using the LDM approach described above. Here, $||\rho^{T_A}||$ denotes the trace norm of the partially transposed density matrix with the transpose taken over the degrees of freedom labeled by A. This quantity gives a measure for the separability of a state. If two subsystems are entangled, the partial transpose can lead to negative eigenvalues, which leads to a trace norm greater than one and hence a non-zero negativity.

Panel (a) of Fig. 7.7 shows the negativity for both models considered in this paper for the three different possible bipartitions of a four-site system. In the case of the simpler model in Eq. (7.1) with the $\sigma^z\sigma^z$ interaction we see a clear peak in the negativity at around $h \sim 0.9\gamma$ for all partitions and a fast decay to zero at values of h above and below this point. This is because of the two limiting cases described in Eqs. (7.2) and (7.3) which both have zero negativity. The peak corresponds well to the range of h-values which were the the most difficult to find convergence with the neural networks.

In case of the more difficult model described in Eq. (7.5) with $\sigma^x\sigma^x$ interactions we see a much higher negativity across the whole range of values of h. This ties in well with our experience that this model is much harder to properly converge using both the LDM and NDM approaches across the board, with LDMs still converging much better overall. We see that there is no region where the negativity reaches zero.

This model does not have a simple product state steady-state anywhere in the observed parameter range, which suggests that LDMs are able to handle the higher information content of the states more efficiently. These results are in line with what we expected when we designed the ansatz following Ref. [20].

7.4 Conclusion and Outlook

In summary we have proposed a NNQS ansatz which compactly represents density matrices in Liouville space, allowing us to find the steady-state of lattice models described by a Markovian master equation. This LDM approach was shown to be able to calculate the steady-state of a 1D open transverse field Ising model with 6 and 16 sites. The results were compared to the powerful NDM ansatz as implemented in NetKet. We found that our approach is always able to reach a comparable accuracy and in many cases is better able to find steady-state, especially when it contains a lot of correlations. We were able to show that the accuracy of this approach is able to be systematically improved by increasing the number of hidden units and hence free parameters in the ansatz.

This permits a clear understanding of the class of states accessible to the LDM

ansatz. As we show in Figs. 7.2 and 7.4, the most difficult regions to find convergence are very strongly correlated with parameters where the true steady-state has high negativity. This is in contrast with the NDM approach where there is difficulty representing mixed states with no correlations leading to a plateaus in the cost function which do not significantly decrease as the steady-state becomes more separable.

The results shown here are just a starting point for examining the usefulness of neural network approaches to finding the steady-state of open quantum systems. RBMs are the simplest network architecture and extending the approach presented here to deep networks such as as deep RBMs [180], Recurrent Neural Networks [181], or transformers [182], provides a route to improving both the accuracy and numerical efficiency. While the models studied here are very simple and accessible by other methods such as tensor network based techniques, the lack of an underlying lattice geometry for these neural networks can be exploited to study models with long range interactions and higher spatial dimensions.

Apart from an investigation of various architectures, a natural next step would be an extension to larger spin sizes. The authors of [20] have shown in great detail how their ansatz extends from spin-1/2 to spin-1 systems and in [5] we have shown how to extended it to spin-1/2 density matrices in a similar fashion. The number of parameters grows linearly in spin size, i.e.

$$N_p = N(d-1) + NM(d-1) + M, \tag{7.7}$$

where N is the number of spins, M is the number of hidden units and d is the local dimension of the Liouville space, i.e. $d = 4$ for spin-1/2. A possible issue is that each local state needs to be assigned a numerical label. As discussed in Ch. 6, common labels are Ising like: $[-S, \cdots, 0, \cdots S]$ or numerical: $[0 \cdots d-1]$. An issue that could arise for larger spin sizes is that the ansatz is exponential in label-sizes and thus highly sensitive to changes in parameters. This could be mitigated by moving the ansatz into so-called log-space. Here, the object of interest is not the wave-function ψ but the log of the wave function $\log\psi$.

The advantages of CNNs discussed in Ch. 5 make CNN excellent candidates for

future extensions of LDMs. Now that we know that a compact representation is possible, we will want to go to 2D and more involved systems. CNN with their more efficient encoding of volume law entanglement seem well suited to this endeavour.

Bibliography

[1] Julian Huber, Peter Kirton, Stefan Rotter, and Peter Rabl. Emergence of PT-symmetry breaking in open quantum systems. *SciPost Phys.*, 9:052, 2020.

[2] Yuma Nakanishi and Tomohiro Sasamoto. Dissipative time crystals originating from parity-time symmetry. *Phys. Rev. A*, 107:L010201, Jan 2023.

[3] Mattias Fitzpatrick, Neereja M. Sundaresan, Andy C. Y. Li, Jens Koch, and Andrew A. Houck. Observation of a dissipative phase transition in a one-dimensional circuit qed lattice. *Phys. Rev. X*, 7:011016, Feb 2017.

[4] S. R. K. Rodriguez, W. Casteels, F. Storme, N. Carlon Zambon, I. Sagnes, L. Le Gratiet, E. Galopin, A. Lemaître, A. Amo, C. Ciuti, and J. Bloch. Probing a dissipative phase transition via dynamical optical hysteresis. *Phys. Rev. Lett.*, 118:247402, Jun 2017.

[5] Simon Kothe and Peter Kirton. Liouville-space neural network representation of density matrices. *Phys. Rev. A*, 109:062215, Jun 2024.

[6] L. D. Landau and E. M. Lifshitz. *Statistical Physics*. Pergamon Press, 1969.

[7] Subir Sachdev. *Quantum Phase Transitions*. Cambridge University Press, 2 edition, 2011.

[8] Julien Vidal, Rémy Mosseri, and Jorge Dukelsky. Entanglement in a first-order quantum phase transition. *Phys. Rev. A*, 69:054101, May 2004.

[9] Julien Vidal, Guillaume Palacios, and Rémy Mosseri. Entanglement in a second-order quantum phase transition. *Phys. Rev. A*, 69:022107, Feb 2004.

[10] Chaitanya Joshi, Felix Nissen, and Jonathan Keeling. Quantum correlations in the one-dimensional driven dissipative xy model. *Phys. Rev. A*, 88:063835, Dec 2013.

[11] Ş. K. Özdemir, S. Rotter, F. Nori, and L. Yang. Parity–time symmetry and exceptional points in photonics. *Nature Materials*, 18:783–798, August 2019.

[12] Carl M. Bender and Stefan Boettcher. Real spectra in non-hermitian hamiltonians having pt symmetry. *Phys. Rev. Lett.*, 80:5243–5246, Jun 1998.

[13] Hamidreza Ramezani, Tsampikos Kottos, Ramy El-Ganainy, and Demetrios N. Christodoulides. Unidirectional nonlinear $\mathcal{PT}$-symmetric optical structures. *Phys. Rev. A*, 82:043803, Oct 2010.

[14] Carl M. Bender, Bjorn K. Berntson, David Parker, and E. Samuel. Observation of PT phase transition in a simple mechanical system. *American Journal of Physics*, 81(3):173–179, 03 2013.

[15] Julian Huber, Peter Kirton, and Peter Rabl. Nonequilibrium magnetic phases in spin lattices with gain and loss. *Phys. Rev. A*, 102:012219, Jul 2020.

[16] Federico Becca and Sandro Sorella. *Quantum Monte Carlo Approaches For Correlated Systems*. Cambridge University Press, 2017.

[17] Giuseppe Carleo and Matthias Troyer. Solving the quantum many-body problem with artificial neural networks. *Science*, 355(6325):602–606, 2017.

[18] Jing Chen, Song Cheng, Haidong Xie, Lei Wang, and Tao Xiang. Equivalence of restricted boltzmann machines and tensor network states. *Phys. Rev. B*, 97:085104, Feb 2018.

[19] Michael Zwolak and Guifré Vidal. Mixed-state dynamics in one-dimensional quantum lattice systems: A time-dependent superoperator renormalization algorithm. *Phys. Rev. Lett.*, 93:207205, Nov 2004.

[20] Michael Y. Pei and Stephen R. Clark. Neural-network quantum states for spin-1 systems: Spin-basis and parameterization effects on compactness of representations. *Entropy*, 23(7):879, 2021.

[21] Filippo Vicentini, Alberto Biella, Nicolas Regnault, and Cristiano Ciuti. Variational neural-network ansatz for steady states in open quantum systems. *Phys. Rev. Lett.*, 122:250503, Jun 2019.

[22] H.J. Lipkin, N. Meshkov, and A.J. Glick. Validity of many-body approximation methods for a solvable model: (i). exact solutions and perturbation theory. *Nuclear Physics*, 62(2):188–198, 1965.

[23] Heinz-Peter Breuer and Francesco Petruccione. *The Theory of open quantum systems*. Oxford, 2002.

[24] Daniel A. Lidar. Lecture notes on the theory of open quantum systems, 2020.

[25] D.F. Walls and Milburn Gerard J. *Quantum Optics 2nd Edition (2008)*. Springer, 2nd edition, 1994.

[26] Inés de Vega and Daniel Alonso. Dynamics of non-markovian open quantum systems. *Rev. Mod. Phys.*, 89:015001, Jan 2017.

[27] Andrew J. Daley. Quantum trajectories and open many-body quantum systems. *Advances in Physics*, 63(2):77–149, 2014.

[28] Ievgen I. Arkhipov, Adam Miranowicz, Fabrizio Minganti, and Franco Nori. Quantum and semiclassical exceptional points of a linear system of coupled cavities with losses and gain within the scully-lamb laser theory. *Phys. Rev. A*, 101:013812, Jan 2020.

[29] Zin Lin, Hamidreza Ramezani, Toni Eichelkraut, Tsampikos Kottos, Hui Cao, and Demetrios N. Christodoulides. Unidirectional invisibility induced by $\mathcal{PT}$-symmetric periodic structures. *Phys. Rev. Lett.*, 106:213901, May 2011.

[30] Xuefeng Zhu, Hamidreza Ramezani, Chengzhi Shi, Jie Zhu, and Xiang Zhang. $\mathcal{PT}$-symmetric acoustics. *Phys. Rev. X*, 4:031042, Sep 2014.

[31] Kun Ding, Guancong Ma, Meng Xiao, Z. Q. Zhang, and C. T. Chan. Emergence, coalescence, and topological properties of multiple exceptional points and their experimental realization. *Phys. Rev. X*, 6:021007, Apr 2016.

[32] Joseph Schindler, Ang Li, Mei C. Zheng, F. M. Ellis, and Tsampikos Kottos. Experimental study of active lrc circuits with $\mathcal{PT}$ symmetries. *Phys. Rev. A*, 84:040101, Oct 2011.

[33] N. Bender, S. Factor, J. D. Bodyfelt, H. Ramezani, D. N. Christodoulides, F. M. Ellis, and T. Kottos. Observation of asymmetric transport in structures with active nonlinearities. *Phys. Rev. Lett.*, 110:234101, Jun 2013.

[34] Yang Wu, Wenquan Liu, Jianpei Geng, Xingrui Song, Xiangyu Ye, Chang-Kui Duan, Xing Rong, and Jiangfeng Du. Observation of parity-time symmetry breaking in a single-spin system. *Science*, 364(6443):878–880, 2019.

[35] Anant V. Varma and Sourin Das. Simulating many-body non-hermitian $\mathcal{PT}$-symmetric spin dynamics. *Phys. Rev. B*, 104:035153, Jul 2021.

[36] L. Tetling, M. V. Fistul, and Ilya M. Eremin. Linear response for pseudo-hermitian hamiltonian systems: Application to pt-symmetric qubits. *Phys. Rev. B*, 106:134511, Oct 2022.

[37] Stavros Komineas. Non-hermitian dynamics for a two-spin system with $\mathcal{PT}$ symmetry. *Phys. Rev. B*, 107:094435, Mar 2023.

[38] Grigory A. Starkov, Mikhail V. Fistul, and Ilya M. Eremin. Quantum phase transitions in non-hermitian pt-symmetric transverse-field ising spin chains. *Annals of Physics*, 456:169268, 2023.

[39] Fabrizio Minganti, Adam Miranowicz, Ravindra W. Chhajlany, and Franco Nori. Quantum exceptional points of non-hermitian hamiltonians and liouvillians: The effects of quantum jumps. *Phys. Rev. A*, 100:062131, Dec 2019.

[40] Fabrizio Minganti, Alberto Biella, Nicola Bartolo, and Cristiano Ciuti. Spectral theory of liouvillians for dissipative phase transitions. *Phys. Rev. A*, 98:042118, Oct 2018.

[41] Fabrizio Minganti, Adam Miranowicz, Ravindra W. Chhajlany, Ievgen I. Arkhipov, and Franco Nori. Hybrid-liouvillian formalism connecting exceptional points of non-hermitian hamiltonians and liouvillians via postselection of quantum trajectories. *Phys. Rev. A*, 101:062112, Jun 2020.

[42] Andrew Pocklington and Aashish A. Clerk. Stability via symmetry breaking in interacting driven systems, 2023.

[43] Toma ž Prosen. $\mathbb{PT}$-symmetric quantum liouvillean dynamics. *Phys. Rev. Lett.*, 109:090404, Aug 2012.

[44] Toma ž Prosen. Generic examples of $\mathbb{PT}$-symmetric qubit (spin-1/2) liouvillian dynamics. *Phys. Rev. A*, 86:044103, Oct 2012.

[45] Yuma Nakanishi and Tomohiro Sasamoto. $\mathcal{PT}$ phase transition in open quantum systems with lindblad dynamics. *Phys. Rev. A*, 105:022219, Feb 2022.

[46] F. Iemini, A. Russomanno, J. Keeling, M. Schirò, M. Dalmonte, and R. Fazio. Boundary time crystals. *Phys. Rev. Lett.*, 121:035301, Jul 2018.

[47] Matteo Marcuzzi, Michael Buchhold, Sebastian Diehl, and Igor Lesanovsky. Absorbing state phase transition with competing quantum and classical fluctuations. *Phys. Rev. Lett.*, 116:245701, Jun 2016.

[48] Edward Gillman, Federico Carollo, and Igor Lesanovsky. Numerical simulation of critical dissipative non-equilibrium quantum systems with an absorbing state. *New Journal of Physics*, 21(9):093064, sep 2019.

[49] Federico Carollo, Edward Gillman, Hendrik Weimer, and Igor Lesanovsky. Critical behavior of the quantum contact process in one dimension. *Phys. Rev. Lett.*, 123:100604, Sep 2019.

[50] K Binder. Theory of first-order phase transitions. *Reports on Progress in Physics*, 50(7):783, jul 1987.

[51] Tony E. Lee, Sarang Gopalakrishnan, and Mikhail D. Lukin. Unconventional magnetism via optical pumping of interacting spin systems. *Phys. Rev. Lett.*, 110:257204, Jun 2013.

[52] Bernhard Baumgartner and Heide Narnhofer. Analysis of quantum semigroups with gks–lindblad generators: Ii. general. *Journal of Physics A: Mathematical and Theoretical*, 41(39):395303, sep 2008.

[53] Berislav Buča and Tomaž Prosen. A note on symmetry reductions of the lindblad equation: transport in constrained open spin chains. *New Journal of Physics*, 14(7):073007, jul 2012.

[54] Victor V. Albert and Liang Jiang. Symmetries and conserved quantities in lindblad master equations. *Phys. Rev. A*, 89:022118, Feb 2014.

[55] E. M. Kessler, G. Giedke, A. Imamoglu, S. F. Yelin, M. D. Lukin, and J. I. Cirac. Dissipative phase transition in a central spin system. *Phys. Rev. A*, 86:012116, Jul 2012.

[56] Katarzyna Macieszczak, Măd ălin Guţă, Igor Lesanovsky, and Juan P. Garrahan. Towards a theory of metastability in open quantum dynamics. *Phys. Rev. Lett.*, 116:240404, Jun 2016.

[57] Lucas Sá, Pedro Ribeiro, and Toma ž Prosen. Symmetry classification of many-body lindbladians: Tenfold way and beyond. *Phys. Rev. X*, 13:031019, Aug 2023.

[58] Igor Lesanovsky, Katarzyna Macieszczak, and Juan P Garrahan. Non-equilibrium absorbing state phase transitions in discrete-time quantum cellular automaton dynamics on spin lattices. *Quantum Science and Technology*, 4(2):02LT02, jan 2019.

[59] Katarzyna Macieszczak. Operational approach to metastability, 2021.

[60] Katarzyna Macieszczak, Dominic C. Rose, Igor Lesanovsky, and Juan P. Garrahan. Theory of classical metastability in open quantum systems. *Phys. Rev. Res.*, 3:033047, Jul 2021.

[61] Calum A. Brown, Katarzyna Macieszczak, and Robert L. Jack. Unravelling metastable markovian open quantum systems, 2023.

[62] Stephanie Matern, Katarzyna Macieszczak, Simon Wozny, and Martin Leijnse. Metastability and quantum coherence assisted sensing in interacting parallel quantum dots. *Phys. Rev. B*, 107:125424, Mar 2023.

[63] Guifré Vidal. Efficient classical simulation of slightly entangled quantum computations. *Phys. Rev. Lett.*, 91:147902, Oct 2003.

[64] Steven R. White. Density matrix formulation for quantum renormalization groups. *Phys. Rev. Lett.*, 69:2863–2866, Nov 1992.

[65] Steven R. White and Adrian E. Feiguin. Real-time evolution using the density matrix renormalization group. *Phys. Rev. Lett.*, 93:076401, Aug 2004.

[66] Ulrich Schollwöck. The density-matrix renormalization group in the age of matrix product states. *Ann. Phys.*, 326(1):96–192, 2011.

[67] Román Orús. A practical introduction to tensor networks: Matrix product states and projected entangled pair states. *Ann. Phys.*, 349:117–158, 2014.

[68] R. Dum, P. Zoller, and H. Ritsch. Monte carlo simulation of the atomic master equation for spontaneous emission. *Phys. Rev. A*, 45:4879–4887, Apr 1992.

[69] Klaus Mølmer, Yvan Castin, and Jean Dalibard. Monte carlo wave-function method in quantum optics. *J. Opt. Soc. Am. B*, 10(3):524–538, Mar 1993.

[70] S. Finazzi, A. Le Boité, F. Storme, A. Baksic, and C. Ciuti. Corner-space renormalization method for driven-dissipative two-dimensional correlated systems. *Phys. Rev. Lett.*, 115:080604, Aug 2015.

[71] R. Rota, F. Storme, N. Bartolo, R. Fazio, and C. Ciuti. Critical behavior of dissipative two-dimensional spin lattices. *Phys. Rev. B*, 95:134431, Apr 2017.

[72] Riccardo Rota, Fabrizio Minganti, Cristiano Ciuti, and Vincenzo Savona. Quantum critical regime in a quadratically driven nonlinear photonic lattice. *Phys. Rev. Lett.*, 122:110405, Mar 2019.

[73] Nicola Bartolo, Fabrizio Minganti, Wim Casteels, and Cristiano Ciuti. Exact steady state of a kerr resonator with one- and two-photon driving and dissipation: Controllable wigner-function multimodality and dissipative phase transitions. *Phys. Rev. A*, 94:033841, Sep 2016.

[74] Zhihai Wang, Tuomas Jaako, Peter Kirton, and Peter Rabl. Supercorrelated radiance in nonlinear photonic waveguides. *Phys. Rev. Lett.*, 124:213601, May 2020.

[75] Myung-Joong Hwang, Peter Rabl, and Martin B. Plenio. Dissipative phase transition in the open quantum rabi model. *Phys. Rev. A*, 97:013825, Jan 2018.

[76] Dainius Kilda and Jonathan Keeling. Fluorescence spectrum and thermalization in a driven coupled cavity array. *Phys. Rev. Lett.*, 122:043602, Feb 2019.

[77] Hendrik Weimer, Augustine Kshetrimayum, and Román Orús. Simulation methods for open quantum many-body systems. *Rev. Mod. Phys.*, 93:015008, Mar 2021.

[78] Pieter W. Claeys and Austen Lamacraft. Dissipative dynamics in open xxz richardson-gaudin models. *Phys. Rev. Res.*, 4:013033, Jan 2022.

[79] Linyu Song and Jiasen Jin. Crossover from discontinuous to continuous phase transition in a dissipative spin system with collective decay. *Phys. Rev. B*, 108:054302, Aug 2023.

[80] R. H. Dicke. Coherence in spontaneous radiation processes. *Phys. Rev.*, 93:99–110, Jan 1954.

[81] Peter Kirton and Jonathan Keeling. Superradiant and lasing states in driven-dissipative dicke models. *New Journal of Physics*, 20(1):015009, jan 2018.

[82] F. Dimer, B. Estienne, A. S. Parkins, and H. J. Carmichael. Proposed realization of the dicke-model quantum phase transition in an optical cavity qed system. *Phys. Rev. A*, 75:013804, Jan 2007.

[83] Kristian Baumann, Christine Guerlin, Ferdinand Brennecke, and Tilman Esslinger. Dicke quantum phase transition with a superfluid gas in an optical cavity. *Nature*, 464(7293):1301–1306, Apr 2010.

[84] K. Baumann, R. Mottl, F. Brennecke, and T. Esslinger. Exploring symmetry breaking at the dicke quantum phase transition. *Phys. Rev. Lett.*, 107:140402, Sep 2011.

[85] Peter Kirton, Mor M. Roses, Jonathan Keeling, and Emanuele G. Dalla Torre. Introduction to the dicke model: From equilibrium to nonequilibrium, and vice versa. *Advanced Quantum Technologies*, 2(1-2):1800043, 2019.

[86] B. Juliá-Díaz, E. Torrontegui, J. Martorell, J. G. Muga, and A. Polls. Fast generation of spin-squeezed states in bosonic josephson junctions. *Phys. Rev. A*, 86:063623, Dec 2012.

[87] P. Buonsante, R. Burioni, E. Vescovi, and A. Vezzani. Quantum criticality in a bosonic josephson junction. *Phys. Rev. A*, 85:043625, Apr 2012.

[88] Yue Ma, Thai M. Hoang, Ming Gong, Tongcang Li, and Zhang-qi Yin. Proposal for quantum many-body simulation and torsional matter-wave interferometry with a levitated nanodiamond. *Phys. Rev. A*, 96:023827, Aug 2017.

[89] Julian Huber, Peter Kirton, and Peter Rabl. Phase-space methods for simulating the dissipative many-body dynamics of collective spin systems. *SciPost Phys.*, 10:045, 2021.

[90] R. Botet, R. Jullien, and P. Pfeuty. Size scaling for infinitely coordinated systems. *Phys. Rev. Lett.*, 49:478–481, Aug 1982.

[91] Sébastien Dusuel and Julien Vidal. Finite-size scaling exponents of the lipkin-meshkov-glick model. *Phys. Rev. Lett.*, 93:237204, Dec 2004.

[92] Sébastien Dusuel and Julien Vidal. Continuous unitary transformations and finite-size scaling exponents in the lipkin-meshkov-glick model. *Phys. Rev. B*, 71:224420, Jun 2005.

[93] José I. Latorre, Román Orús, Enrique Rico, and Julien Vidal. Entanglement entropy in the lipkin-meshkov-glick model. *Phys. Rev. A*, 71:064101, Jun 2005.

[94] Julien Vidal, Sébastien Dusuel, and Thomas Barthel. Entanglement entropy in collective models. *Journal of Statistical Mechanics: Theory and Experiment*, 2007(01):P01015, jan 2007.

[95] Pedro Ribeiro, Julien Vidal, and Rémy Mosseri. Exact spectrum of the lipkin-meshkov-glick model in the thermodynamic limit and finite-size corrections. *Phys. Rev. E*, 78:021106, Aug 2008.

[96] Yi Huang, Tongcang Li, and Zhang-qi Yin. Symmetry-breaking dynamics of the finite-size lipkin-meshkov-glick model near ground state. *Phys. Rev. A*, 97:012115, Jan 2018.

[97] S. Morrison and A. S. Parkins. Dynamical quantum phase transitions in the dissipative lipkin-meshkov-glick model with proposed realization in optical cavity qed. *Phys. Rev. Lett.*, 100:040403, Jan 2008.

[98] S. Morrison and A. S. Parkins. Collective spin systems in dispersive optical cavity qed: Quantum phase transitions and entanglement. *Phys. Rev. A*, 77:043810, Apr 2008.

[99] João S. Ferreira and Pedro Ribeiro. Lipkin-meshkov-glick model with markovian dissipation: A description of a collective spin on a metallic surface. *Phys. Rev. B*, 100:184422, Nov 2019.

[100] Alessio Serafini, Fabrizio Illuminati, Matteo G. A. Paris, and Silvio De Siena. Entanglement and purity of two-mode gaussian states in noisy channels. *Phys. Rev. A*, 69:022318, Feb 2004.

[101] Leo P Kadanoff. More is the same; phase transitions and mean field theories. *Journal of Statistical Physics*, 137:777 – 797, Dec 2009.

[102] Taushif Ahmed. Spin coherent state through path integral and semi-classical physics, 2011.

[103] Hendrik Weimer. Variational principle for steady states of dissipative quantum many-body systems. *Phys. Rev. Lett.*, 114:040402, Jan 2015.

[104] Nicholas Metropolis. The beginning of the monte carlo method. *Los Alamos Science Special Issue*, 15:125–130, 1987.

[105] Sandro Sorella. Generalized lanczos algorithm for variational quantum monte carlo. *Phys. Rev. B*, 64:024512, Jun 2001.

[106] Eric Neuscamman, C. J. Umrigar, and Garnet Kin-Lic Chan. Optimizing large parameter sets in variational quantum monte carlo. *Phys. Rev. B*, 85:045103, Jan 2012.

[107] Stefan Weinzierl. Introduction to monte carlo methods, 2000.

[108] Nicholas Metropolis, Arianna W. Rosenbluth, Marshall N. Rosenbluth, Augusta H. Teller, and Edward Teller. Equation of state calculations by fast computing machines. *The Journal of Chemical Physics*, 21(6):1087–1092, 1953.

[109] W. K. Hastings. Monte carlo sampling methods using markov chains and their applications. *Biometrika*, 57(1):97–109, 1970.

[110] Helmut G. Katzgraber. Introduction to monte carlo methods, 2011.

[111] Robert H. Swendsen and Jian-Sheng Wang. Replica monte carlo simulation of spin-glasses. *Phys. Rev. Lett.*, 57:2607–2609, Nov 1986.

[112] Jian-Sheng Wang and Robert H. Swendsen. Replica Monte Carlo Simulation (Revisited). *Progress of Theoretical Physics Supplement*, 157:317–323, 01 2005.

[113] Helmut G Katzgraber, Simon Trebst, David A Huse, and Matthias Troyer. Feedback-optimized parallel tempering monte carlo. *J. Stat. Mech.: Theory and Experiment*, 2006(03):P03018, mar 2006.

[114] Yasuyuki Ishikawa, Yuji Sugita, Takeshi Nishikawa, and Yuko Okamoto. Ab initio replica-exchange monte carlo method for cluster studies. *Chemical Physics Letters*, 333(1):199–206, 2001.

[115] Pinaki Sengupta, Anders W. Sandvik, and David K. Campbell. Bond-order-wave phase and quantum phase transitions in the one-dimensional extended hubbard model. *Phys. Rev. B*, 65:155113, Apr 2002.

[116] David J. Earl and Michael W. Deem. Parallel tempering: Theory, applications, and new perspectives. *Phys. Chem. Chem. Phys.*, 7:3910–3916, 2005.

[117] F. Verstraete, D. Porras, and J. I. Cirac. Density matrix renormalization group and periodic boundary conditions: A quantum information perspective. *Phys. Rev. Lett.*, 93:227205, Nov 2004.

[118] Carl Eckart and Gale Young. The approximation of one matrix by another of lower rank. *Psychometrika*, 1(3):211–218, Sep 1936.

[119] Masuo Suzuki. Generalized trotter's formula and systematic approximants of exponential operators and inner derivations with applications to many-body problems. *Communications in Mathematical Physics*, 51(2):183–190, Jun 1976.

[120] I. P. McCulloch. Infinite size density matrix renormalization group, revisited, 2008.

[121] R. Orús and G. Vidal. Infinite time-evolving block decimation algorithm beyond unitary evolution. *Phys. Rev. B*, 78:155117, Oct 2008.

[122] G. Vidal, J. I. Latorre, E. Rico, and A. Kitaev. Entanglement in quantum critical phenomena. *Phys. Rev. Lett.*, 90:227902, Jun 2003.

[123] F. Verstraete and J. I. Cirac. Matrix product states represent ground states faithfully. *Phys. Rev. B*, 73:094423, Mar 2006.

[124] J. Eisert, M. Cramer, and M. B. Plenio. Colloquium: Area laws for the entanglement entropy. *Rev. Mod. Phys.*, 82:277–306, Feb 2010.

[125] F. Verstraete and J. I. Cirac. Renormalization algorithms for quantum-many body systems in two and higher dimensions, 2004.

[126] H. C. Jiang, Z. Y. Weng, and T. Xiang. Accurate determination of tensor network state of quantum lattice models in two dimensions. *Phys. Rev. Lett.*, 101:090603, Aug 2008.

[127] J. Jordan, R. Orús, G. Vidal, F. Verstraete, and J. I. Cirac. Classical simulation of infinite-size quantum lattice systems in two spatial dimensions. *Phys. Rev. Lett.*, 101:250602, Dec 2008.

[128] Jonas Haferkamp, Dominik Hangleiter, Jens Eisert, and Marek Gluza. Contracting projected entangled pair states is average-case hard. *Phys. Rev. Res.*, 2:013010, Jan 2020.

[129] F. Verstraete, J. J. García-Ripoll, and J. I. Cirac. Matrix product density operators: Simulation of finite-temperature and dissipative systems. *Phys. Rev. Lett.*, 93:207204, Nov 2004.

[130] Michael Nielsen and Isaac Chuang. *Quantum Computation and Quantum Information*. Cambridge University Press, 2000.

[131] Jian Cui, J. Ignacio Cirac, and Mari Carmen Bañuls. Variational matrix product operators for the steady state of dissipative quantum systems. *Phys. Rev. Lett.*, 114:220601, Jun 2015.

[132] Adil A. Gangat, Te I, and Ying-Jer Kao. Steady states of infinite-size dissipative quantum chains via imaginary time evolution. *Phys. Rev. Lett.*, 119:010501, Jul 2017.

[133] Dainius Kilda, Alberto Biella, Marco Schirò, Rosario Fazio, and Jonathan Keeling. On the stability of the infinite Projected Entangled Pair Operator ansatz for driven-dissipative 2D lattices. *SciPost Phys. Core*, 4:005, 2021.

[134] Augustine Kshetrimayum, Hendrik Weimer, and Román Orús. A simple tensor network algorithm for two-dimensional steady states. *Nature Communications*, 8(1):1291, Nov 2017.

[135] Román Orús. Exploring corner transfer matrices and corner tensors for the classical simulation of quantum lattice systems. *Phys. Rev. B*, 85:205117, May 2012.

[136] C. Mc Keever and M. H. Szymańska. Stable ipepo tensor-network algorithm for dynamics of two-dimensional open quantum lattice models. *Phys. Rev. X*, 11:021035, May 2021.

[137] Glen Evenbly. Gauge fixing, canonical forms, and optimal truncations in tensor networks with closed loops. *Phys. Rev. B*, 98:085155, Aug 2018.

[138] M. T. Fishman, L. Vanderstraeten, V. Zauner-Stauber, J. Haegeman, and F. Verstraete. Faster methods for contracting infinite two-dimensional tensor networks. *Phys. Rev. B*, 98:235148, Dec 2018.

[139] Roger G Melko, Giuseppe Carleo, Juan Carrasquilla, and J Ignacio Cirac. Restricted boltzmann machines in quantum physics. *Nat. Phys.*, 15(9):887, 2019.

[140] Giuseppe Carleo, Ignacio Cirac, Kyle Cranmer, Laurent Daudet, Maria Schuld, Naftali Tishby, Leslie Vogt-Maranto, and Lenka Zdeborová. Machine learning and the physical sciences. *Rev. Mod. Phys.*, 91:045002, Dec 2019.

[141] Dong-Ling Deng, Xiaopeng Li, and S. Das Sarma. Quantum entanglement in neural network states. *Phys. Rev. X*, 7:021021, May 2017.

[142] Yusuke Nomura. Helping restricted boltzmann machines with quantum-state representation by restoring symmetry. *Journal of Physics: Condensed Matter*, 33(17):174003, apr 2021.

[143] Moritz Reh, Markus Schmitt, and Martin Gärttner. Optimizing design choices for neural quantum states. *Phys. Rev. B*, 107:195115, May 2023.

[144] Or Sharir, Amnon Shashua, and Giuseppe Carleo. Neural tensor contractions and the expressive power of deep neural quantum states. *Phys. Rev. B*, 106:205136, Nov 2022.

[145] Giacomo Passetti, Damian Hofmann, Pit Neitemeier, Lukas Grunwald, Michael A. Sentef, and Dante M. Kennes. Can neural quantum states learn volume-law ground states?, 2022.

[146] Pankaj Mehta and David J. Schwab. An exact mapping between the variational renormalization group and deep learning, 2014.

[147] Mohamed Hibat-Allah, Roger G. Melko, and Juan Carrasquilla. Supplementing recurrent neural network wave functions with symmetry and annealing to improve accuracy, 2024.

[148] Stefanie Czischek, Martin Gärttner, and Thomas Gasenzer. Quenches near ising quantum criticality as a challenge for artificial neural networks. *Phys. Rev. B*, 98:024311, Jul 2018.

[149] Luciano Loris Viteritti, Francesco Ferrari, and Federico Becca. Accuracy of restricted Boltzmann machines for the one-dimensional $J_1 - J_2$ Heisenberg model. *SciPost Phys.*, 12:166, 2022.

[150] Kaelan Donatella, Zakari Denis, Alexandre Le Boité, and Cristiano Ciuti. Dynamics with autoregressive neural quantum states: Application to critical quench dynamics. *Phys. Rev. A*, 108:022210, Aug 2023.

[151] Or Sharir, Yoav Levine, Noam Wies, Giuseppe Carleo, and Amnon Shashua. Deep autoregressive models for the efficient variational simulation of many-body quantum systems. *Phys. Rev. Lett.*, 124:020503, Jan 2020.

[152] Mohamed Hibat-Allah, Martin Ganahl, Lauren E. Hayward, Roger G. Melko, and Juan Carrasquilla. Recurrent neural network wave functions. *Phys. Rev. Res.*, 2:023358, Jun 2020.

[153] Di Luo, Zhuo Chen, Juan Carrasquilla, and Bryan K. Clark. Autoregressive neural network for simulating open quantum systems via a probabilistic formulation. *Phys. Rev. Lett.*, 128:090501, Feb 2022.

[154] Dian Wu, Riccardo Rossi, Filippo Vicentini, and Giuseppe Carleo. From tensor network quantum states to tensorial recurrent neural networks, 2023.

[155] Markus Schmitt and Markus Heyl. Quantum many-body dynamics in two dimensions with artificial neural networks. *Phys. Rev. Lett.*, 125:100503, Sep 2020.

[156] Kenny Choo, Titus Neupert, and Giuseppe Carleo. Two-dimensional frustrated J_1-J_2 model studied with neural network quantum states. *Phys. Rev. B*, 100:125124, Sep 2019.

[157] Irene López Gutiérrez and Christian B. Mendl. Real time evolution with neural-network quantum states. *Quantum*, 6:627, January 2022.

[158] Christopher Roth, Attila Szabó, and Allan H. MacDonald. High-accuracy variational monte carlo for frustrated magnets with deep neural networks. *Physical Review B*, 108(5), August 2023.

[159] Yoav Levine, Or Sharir, Nadav Cohen, and Amnon Shashua. Quantum entanglement in deep learning architectures. *Phys. Rev. Lett.*, 122:065301, Feb 2019.

[160] Giacomo Torlai and Roger G. Melko. Latent space purification via neural density operators. *Phys. Rev. Lett.*, 120:240503, Jun 2018.

[161] Michael J. Hartmann and Giuseppe Carleo. Neural-network approach to dissipative quantum many-body dynamics. *Phys. Rev. Lett.*, 122:250502, Jun 2019.

[162] Alexandra Nagy and Vincenzo Savona. Variational quantum monte carlo method with a neural-network ansatz for open quantum systems. *Phys. Rev. Lett.*, 122:250501, Jun 2019.

[163] Johannes Mellak, Enrico Arrigoni, Thomas Pock, and Wolfgang von der Linden. Quantum transport in open spin chains using neural-network quantum states. *Phys. Rev. B*, 107:205102, May 2023.

[164] Giuseppe Carleo, Kenny Choo, Damian Hofmann, James E.T. Smith, Tom Westerhout, Fabien Alet, Emily J. Davis, Stavros Efthymiou, Ivan Glasser, Sheng-Hsuan Lin, Marta Mauri, Guglielmo Mazzola, Christian B. Mendl, Evert van Nieuwenburg, Ossian O'Reilly, Hugo Théveniaut, Giacomo Torlai, Filippo Vicentini, and Alexander Wietek. Netket: A machine learning toolkit for many-body quantum systems. *SoftwareX*, 10:100311, 2019.

[165] Filippo Vicentini, Riccardo Rossi, and Giuseppe Carleo. Positive-definite parametrization of mixed quantum states with deep neural networks, 2022.

[166] Johannes Mellak, Enrico Arrigoni, and Wolfgang von der Linden. Deep neural networks as variational solutions for correlated open quantum systems, 2024.

[167] Juan Carrasquilla, Giacomo Torlai, Roger G. Melko, and Leandro Aolita. Reconstructing quantum states with geenrative models. *Nature Machine Intelligence*, 1:155 – 161, Mar 2019.

[168] Moritz Reh, Markus Schmitt, and Martin Gärttner. Time-dependent variational principle for open quantum systems with artificial neural networks. *Phys. Rev. Lett.*, 127:230501, Dec 2021.

[169] Nobuyuki Yoshioka and Ryusuke Hamazaki. Constructing neural stationary states for open quantum many-body systems. *Phys. Rev. B*, 99:214306, Jun 2019.

[170] Faijul Amin. *Complex-Valued Neural Networks:Learning Algorithms and Applications.* PhD thesis, University of Fukui, 2012.

[171] Chae-Yeun Park and Michael J. Kastoryano. Geometry of learning neural quantum states. *Phys. Rev. Res.*, 2:023232, May 2020.

[172] Ivan Glasser, Nicola Pancotti, Moritz August, Ivan D. Rodriguez, and J. Ignacio Cirac. Neural-network quantum states, string-bond states, and chiral topological states. *Phys. Rev. X*, 8:011006, Jan 2018.

[173] C.-E. Bardyn and A. İmamoğlu. Majorana-like modes of light in a one-dimensional array of nonlinear cavities. *Phys. Rev. Lett.*, 109:253606, Dec 2012.

[174] J.R. Johansson, P.D. Nation, and Franco Nori. Qutip 2: A python framework for the dynamics of open quantum systems. *Comp. Phys. Commun.*, 184(4):1234–1240, 2013.

[175] Jiasen Jin, Alberto Biella, Oscar Viyuela, Leonardo Mazza, Jonathan Keeling, Rosario Fazio, and Davide Rossini. Cluster mean-field approach to the steady-state phase diagram of dissipative spin systems. *Phys. Rev. X*, 6:031011, Jul 2016.

[176] Eduardo Mascarenhas, Hugo Flayac, and Vincenzo Savona. Matrix-product-operator approach to the nonequilibrium steady state of driven-dissipative quantum arrays. *Phys. Rev. A*, 92:022116, Aug 2015.

[177] L Henderson and V Vedral. Classical, quantum and total correlations. *J. Phys. A: Mathematical and General*, 34(35):6899, aug 2001.

[178] G. Vidal and R. F. Werner. Computable measure of entanglement. *Phys. Rev. A*, 65:032314, Feb 2002.

[179] Kavan Modi, Aharon Brodutch, Hugo Cable, Tomasz Paterek, and Vlatko Vedral. The classical-quantum boundary for correlations: Discord and related measures. *Rev. Mod. Phys.*, 84:1655–1707, Nov 2012.

[180] Hengyuan Hu, Lisheng Gao, and Quanbin Ma. Deep restricted boltzmann networks, 2016.

[181] Alex Sherstinsky. Fundamentals of recurrent neural network (rnn) and long short-term memory (lstm) network. *Physica D: Nonlinear Phenomena*, 404:132306, 2020.

[182] Ashish Vaswani, Noam Shazeer, Niki Parmar, Jakob Uszkoreit, Llion Jones, Aidan N. Gomez, Lukasz Kaiser, and Illia Polosukhin. Attention is all you need, 2017.

Appendix A

Liouville Density Machine Code

The code we used for the Part II of the thesis has been developed by the author. Parts of the code were tested individually. For the sampler a fixed set of parameters was used, which heavily favours a single state. The LDM itself was similarly tested using fixed parameter sets and configurations with known results. The optimizer was first tested on a purely dissipative model, whose steady-state is the all-down state. Subsequently, more complex models where tested, whose steady states could be compared to exact results from QUTIP. Similarly, expectation values of local observables where calculated for edge cases first, where the results can be derived analytically. Afterwards, more complex expectation values were compared with results from QUTIP and MPS.

The code is fully annotated. It is currently stored both on the University internal GitLab as well as my own GitHub. The repositories are managed by me and Dr. Peter Kirton.

Appendix A. Liouville Density Machine Code